

Modelling and Simulation of Hypoxia Imaging with Positron Emission Tomography

Dissertation

der Mathematisch-Naturwissenschaftlichen Fakultät
der Eberhard Karls Universität Tübingen
zur Erlangung des Grades eines
Doktors der Naturwissenschaften
(Dr. rer. nat.)

vorgelegt von
David Mönnich
aus Rimbach (Oberpfalz)

Tübingen
2013

Tag der mündlichen Qualifikation:

28.06.2013

Dekan:

Prof. Dr. Wolfgang Rosenstiel

1. Berichterstatter:

Prof. Dr. Dr. Fritz Schick

2. Berichterstatter:

Prof. Dr. Heinz Clement

Contents

| | |
|---|-----------|
| 1. Introduction | 1 |
| 2. Background | 5 |
| 2.1. Tumour hypoxia and its relevance to radiotherapy | 5 |
| 2.1.1. Tumour microvessel networks | 5 |
| 2.1.2. Tumour hypoxia | 5 |
| 2.1.3. Hypoxia and radioresistance | 7 |
| 2.1.4. Specific treatments for hypoxic tumours | 7 |
| 2.2. Assessment of tumour hypoxia | 8 |
| 2.2.1. Overview of different methods | 8 |
| 2.2.2. Basics of positron emission tomography (PET) | 9 |
| 2.2.3. PET imaging with [¹⁸ F]Fluoromisonidazole | 11 |
| 3. Biophysical Models, Materials and Simulation Methods | 15 |
| 3.1. Diffusion-reaction models of O ₂ and FMISO in tumour tissue . . . | 15 |
| 3.1.1. Outline | 15 |
| 3.1.2. Oxygen transport and consumption | 16 |
| 3.1.3. FMISO transport and retention | 17 |
| 3.1.4. Parameter values | 20 |
| 3.2. Simulations of O ₂ and FMISO diffusion-reaction dynamics | 22 |
| 3.2.1. Outline | 22 |
| 3.2.2. Vessel maps from tumour histology | 23 |
| 3.2.3. Numerical methods | 25 |
| 3.2.4. Simulation procedure and data processing | 27 |
| 3.3. Validation of the simulation method | 28 |
| 4. Results and Discussion | 33 |
| 4.1. Fundamentals of FMISO PET signal formation | 33 |
| 4.1.1. Outline | 33 |
| 4.1.2. Results | 34 |
| 4.1.3. Discussion | 40 |
| 4.2. Acute hypoxia in FMISO PET imaging | 43 |

| | |
|---|------------|
| 4.2.1. Outline | 43 |
| 4.2.2. Methods and Materials | 44 |
| 4.2.3. Results | 46 |
| 4.2.4. Discussion | 49 |
| 4.3. Correlation between tumour oxygenation and FMISO PET data . | 53 |
| 4.3.1. Outline | 53 |
| 4.3.2. Methods and Materials | 54 |
| 4.3.3. Results | 56 |
| 4.3.4. Discussion | 62 |
| 5. Summary and Outlook | 65 |
| Bibliography | 69 |
| Appendix A. Modelling and simulation of [¹⁸F]fluoromisonidazole dynamics based on histology-derived microvessel maps | 83 |
| Appendix B. Modelling and simulation of the influence of acute and chronic hypoxia on [¹⁸F]fluoromisonidazole PET imaging | 97 |
| Appendix C. Correlation between tumor oxygenation and 18F-Fluoromisonidazole PET data simulated based on microvasculature images | 109 |
| Appendix D. Combined PET/CT for IMRT treatment planning of NSCLC: Contrast-enhanced CT images for Monte Carlo dose calculation | 121 |

Abbreviations

| | |
|-----------------|---------------------------------------|
| aHF | Acute Hypoxic Fraction |
| AUC | Area Under Curve |
| BOLD | Blood Oxygen Level Dependent |
| cHF | Chronic Hypoxic Fraction |
| CT | Computed Tomography |
| DP | Dose Painting |
| FDG | [¹⁸ F]Fluorodeoxyglucose |
| FEM | Finite Element Method |
| FMISO | [¹⁸ F]Fluoromisonidazole |
| FPR | False Positive Rate |
| FWHM | Full Width at Half Maximum |
| HF | Hypoxic Fraction |
| HNSCC | Head and Neck Squamous Cell Carcinoma |
| IHC | Immunohistochemistry |
| IMRT | Intensity Modulated Radiotherapy |
| LOR | Line of Response |
| MRI | Magnetic Resonance Imaging |
| MTC | Mass Transfer Coefficient |
| ODE | Ordinary Differential Equation |
| PO ₂ | Oxygen Partial Pressure |

Abbreviations

| | |
|-----|-----------------------------------|
| PDE | Partial Differential Equation |
| PET | Positron Emission Tomography |
| pi | Post Injection |
| PSF | Point Spread Function |
| PVE | Partial Volume Effect |
| RCF | Red Cell Flux |
| ROC | Receiver Operating Characteristic |
| ROI | Region of Interest |
| RT | Radiotherapy |
| SCC | Squamous Cell Carcinoma |
| T/B | Tumour to Blood Ratio |
| TAC | Time Activity Curve |
| TPR | True Positive Rate |
| vHF | Vital Hypoxic Fraction |
| YI | Youden Index |

1. Introduction

Radiotherapy (RT) is an established treatment for human cancers. It has been estimated that over 50% of all cancer patients would benefit from RT as isolated treatment or in combinations with surgery and chemotherapy [1]. The aim of RT is to apply a radiation dose focussed on the tumour that is high enough to kill all cancer cells, while keeping the dose to surrounding healthy tissue as low as possible to prevent adverse effects. The precision of RT has improved considerably by the introduction of advanced techniques, such as intensity modulated RT (IMRT) and irradiation with protons and heavier particles [2, 3]. With these techniques homogeneous doses can be delivered that are highly confined to the tumour.

Nevertheless, state of the art combinations of RT and chemotherapy accomplish local tumour control in only about 50% of patients with advanced head and neck cancer [4]. Other tumour entities show similarly low response rates. An explanation for this is the heterogeneous dose response of tumours that appear identical in many other aspects, such as histology, stage and localisation [5]. Several factors contribute to this effect. One of them is the varying density of cells that have the potential to repopulate the tumour and their various intrinsic radiosensitivities [6]. Another important factor is the availability of oxygen, which differs among tumours of the same type as well as within a particular tumour [7].

Regions that are hypoxic, i.e. deprived of oxygen, frequently exist in human tumours [8]. Under hypoxic conditions cells are less sensitive to radiation damage (radioresistant), compared to normal oxygen levels [9]. Correspondingly, several studies correlated tumour hypoxia with a poor prognosis for the success of treatments that involve RT [10, 11]. These studies, however, relied on oxygen measurements using needle probes, which are invasive and do not cover the entire tumour. Therefore, it is of great interest to develop noninvasive methods to assess hypoxia in clinical routine, ideally in three dimensions (3D) and with high spatial resolution. This would allow further classification of tumours into sub-types according to their hypoxic status and therefore adapted treatment strategies. Thus, for tumours of the same sub-type a more homogeneous and better treatment response can be achieved.

So far, no hypoxia imaging modality has been clinically established. A promising candidate is positron emission tomography imaging (PET) using the radiolabelled tracer [^{18}F]Fluoromisonidazole (FMISO). Its basic mechanism is the specific

accumulation of FMISO molecules in hypoxic cells. In a PET scanner, the decay products of the radioisotope ^{18}F labelling the tracer are detected outside of the patient. From this data, the tracer distribution inside of the patient can be mathematically reconstructed in 3D.

FMISO PET imaging and its applicability in RT are not yet fully understood. A number of studies concluded that the overall efficacy of RT can be predicted based on static FMISO PET imaging performed several hours after injection of the tracer [12, 13]. It is not clear whether this is the most reliable (i.e. sensitive, specific and reproducible) overall prediction that can be obtained with FMISO PET. Moreover, there is no evidence that static imaging can be used to assess the distribution of hypoxia-associated radioresistance within a particular tumour.

The latter aspect is particularly important with respect to dose painting (DP), a specific RT technique that has been suggested for the treatment of tumours containing hypoxic regions [14–16]. The concept of DP is to increase the RT dose locally, to compensate the radioresistance of hypoxic regions and kill cells with equal effectiveness in the entire tumour volume. In order to guide DP by FMISO PET, a comprehensive understanding of the image formation process is essential for a correct quantitative interpretation of FMISO PET data. It has been proposed that this requires dynamic PET imaging, which covers the distribution and accumulation of the tracer starting with its injection [17, 18].

It is the aim of this work to develop a fundamental understanding of the formation of FMISO PET signals in tumours. This is intricate, as the availability of oxygen, and consequently also the accumulation of FMISO [19], is very heterogeneous on the microscopic length scale. Therefore, FMISO distributions can not be adequately sampled by PET imaging, because its spatial resolution is limited to a few millimetres [20]. This is referred to as partial volume effect (PVE). From an improved understanding of FMISO PET, substantiated hypotheses about optimum imaging modes for the assessment of hypoxia-associated radioresistance can be developed. These hypotheses can then be used to effectively guide future clinical studies.

It would be extremely complex to pursue this aim by means of experiments under realistic conditions. Thus, in this work a theoretical method is developed to simulate microscopic oxygen distributions and the corresponding dynamics of FMISO molecules. FMISO PET signals are subsequently simulated. The simulation method is based on biophysical models of the diffusion-reaction dynamics of oxygen and FMISO molecules in tumour tissue.

While oxygen has been modelled and simulated in a number of studies [21–23], it is a novel concept to combine this with a model of the diffusion and oxygen-dependent accumulation of a PET tracer [24]. The uniqueness of this work is

that realistic models of tumour capillary networks are used as input data for the simulations. This is very important, in order to adequately model the flux of oxygen as well as FMISO into and out of tissue. The simulation method is validated using pre-clinical and clinical material.

Specific aspects of FMISO PET imaging investigated in this work are:

- In tissue, FMISO distributes slowly by passive diffusion. It takes considerable time for the molecules to reach hypoxic cells, which are typically located far from oxygen-supplying capillaries. The effect of the slow FMISO diffusion on its accumulation, as well as the combined influence on the resulting PET signal is analysed in **Section 4.1**. Moreover, with regard to dynamic PET imaging, it is investigated whether signals detected initially after tracer injection (wash-in phase) and signals detected by static imaging during the accumulation phase contain distinct information. The results are discussed in the context of optimum imaging timepoints of PET scans and their applicability for the individualisation of RT.
- The role of acute hypoxia, i.e. temporally varying hypoxia, and its potential influence on FMISO PET imaging as well as RT is an important issue with regard to clinical applications [25–29]. Therefore, a model of acute hypoxia is integrated into the oxygen diffusion-consumption model, as described in **Section 4.2**. As a consequence, the local oxygen-dependent FMISO accumulation rates become time-dependent as well. The results are discussed in the context of the reproducibility of FMISO PET imaging. Potential implications for its predictive power regarding hypoxia-associated radioresistance are also discussed.
- The quantitative interpretation of FMISO PET data is error-prone, foremost because signals are blurred by the PVE. Moreover, the dependence of the tracer accumulation rate on the oxygen concentration is ambiguous. In **Section 4.3**, the simulation tool developed in this work is used to evaluate different FMISO PET imaging modes with respect to their accuracy as surrogate measures of hypoxia. Specifically, the correlation between FMISO PET signals and the average oxygen concentrations underlying the according PET voxels is evaluated.

2. Background

2.1. Tumour hypoxia and its relevance to radiotherapy

2.1.1. Tumour microvessel networks

Blood vessels are an integral part of the circulatory system of the human body. They have several functions, for instance to supply tissue with nutrients, such as oxygen, and to remove waste products, such as carbon dioxide. Most of the substance exchange takes place between tissue and capillaries, which are the smallest constituents of the vascular system in terms of diameter.

Vascular networks in solid tumours differ from that in normal tissue in many aspects. They are often described as chaotic, because of their aberrant structural properties. These are e.g. enlarged intervessel distances, elongated vessels, irregularly arranged vessels with blind endings and shunts between arterioles and veins. The function of vessels is frequently impaired as well, for instance by an increased permeability of the endothelium and considerable variations in blood flow, including complete flow collapse [8].

2.1.2. Tumour hypoxia

An important effect of the abnormal tumour vessel networks is an insufficient supply of oxygen to tumour cells. This state is referred to as hypoxia. Normally oxygenated cells are called normoxic. Many studies have shown that hypoxia is a frequent trait of different malignancies in humans, especially squamous cell carcinomas of the head and neck (HNSCC) [30]. Hypoxia is a dynamic phenomenon, because oxygen supply by the tumour vasculature varies temporally. Thus, it is distinguished between acute and chronic hypoxia [27]. Acute hypoxia is characterised by tissue oxygen levels that fluctuate with a periodicity on the order of ten minutes [31], whereas chronic hypoxia remains stable for much longer periods.

Chronic hypoxia results from large intervessel distances. Cells far from vessel are undersupplied with oxygen, because it has already been metabolised by cells closer to the vessel. Typically, oxygen supply by a single vessel cord reaches as far as 100–200 μm into tissue [25]. Not only the intervessel distance is crucial, but also the oxygen content in blood, which decreases in flow direction. Thus,

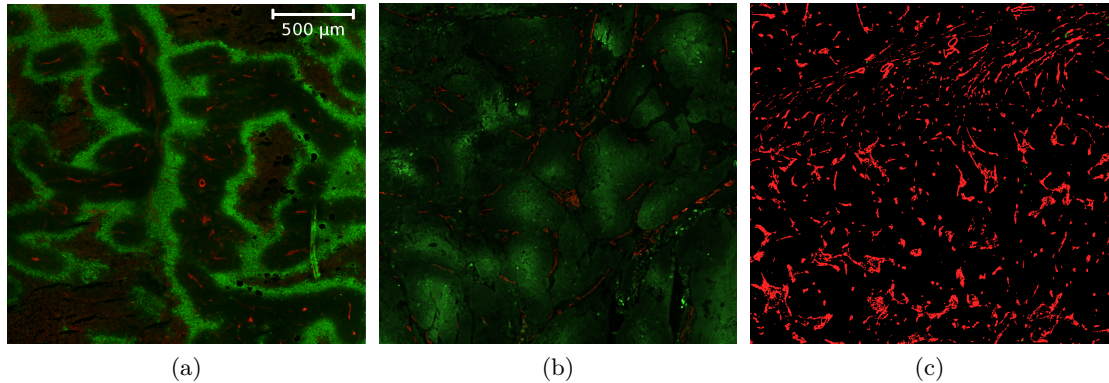


Figure 2.1.: IHC performed in tissue sections from HNSCC xenografts. These are overlays of fluorescence microscopy images of two different markers. Green indicates hypoxia (pimonidazole) and red indicates the endothelium of blood vessels (antibody to mouse endothelium). The scale applies to all images. Note, that hypoxia is distributed heterogeneously on the micrometre scale and that there are distinct hypoxia patterns in the same cell line: (a) ribbon-like hypoxia, (b) patchy hypoxia and (c) normoxia (classification according to [7]). Images provided by courtesy of E. Troost (Department of Radiation Oncology, Radboud University Nijmegen Medical Centre, Nijmegen, The Netherlands).

chronically hypoxic cells might be located closer to vessels at the venous ends of capillaries than close to arterioles. If cells experience extreme deprivation of oxygen and other nutrients, they eventually die in an uncontrolled way. This process is called necrosis and the resulting tissue regions are referred to as being necrotic.

Acute hypoxia results from temporal variations in blood flow and in blood oxygen content, i.e. from a varying perfusion [32,33]. The most extreme aberration in blood supply is total flow stasis. Flow stasis was observed in pre-clinical tumour models [34], though its incidence appears to be lower than that of continuous supply fluctuations [25]. Acutely hypoxic cells experience several cycles of becoming hypoxic followed by reoxygenation.

Chronic and acute hypoxia are closely linked, but they may have different biological consequences. Some studies associated acute hypoxia in tumours with a higher risk for the induction of metastases and an increased radioresistance, compared to chronically hypoxic tumours [26,35].

Immunohistochemical (IHC) methods can be used to image hypoxia in 2D tis-

sue sections. A commonly used biomarker is the 2-nitroimidazole compound pimonidazole, which binds in cells under hypoxic conditions. Pimonidazole can subsequently be visualised using a fluorescent antibody and fluorescence microscopy. IHC studies in tumour xenografts, i.e. human tumour material implanted in an animal, showed that hypoxia is distributed very heterogeneously on the microscopic length scale. This heterogeneity reflects, that oxygen concentrations around vessels vary on the micrometre scale, with chronically hypoxic regions being located 70–100 μm from vessels [36]. Distinctly different patterns of hypoxia were observed in the same cell lines, as illustrated in Figure 2.1a–c) [7]. These aspects are very important in the context of this work, as the spatial resolutions of most noninvasive methods to image hypoxia are much lower.

2.1.3. Hypoxia and radioresistance

Radiotherapy (RT) aims to kill cancer cells by exposing them to ionising radiation. The underlying radiobiological mechanism is the radiation damage to the DNA of cancer cells [37]. In order to fully eliminate a tumour, all cancer stem cells, i.e. cells that have the potential to repopulate the tumour, have to be damaged beyond their repair potential. Oxygen has an important role in this process, as it binds to radicals produced by the absorption of radiation in tissue. In this way it causes permanent changes in biological molecules, e.g. the DNA, which may eventually lead to cell death [13]. Consequently, under hypoxic conditions the probability that radiation damage is repaired is higher and therefore the effectiveness of radiotherapy is lower.

Already in 1953 it was reported, that low oxygen levels are associated with a decreased radiosensitivity [9]. In an extremely hypoxic cell population an up to three times higher radiation dose is needed to achieve the same cell kill as in normoxic cells. The radiosensitivity predominantly decreases for oxygen partial pressures (PO_2) below 10 mmHg [26]. Today, there is a large amount of evidence on the adverse influence of hypoxia on the efficacy of RT in human tumours. In most studies local PO_2 values were assessed with invasive oxygen sensing probes, for instance in SCC of the uterine cervix [10] and of the head and neck [11]. Moreover, many imaging studies with relatively small numbers of patients were performed, using different imaging modalities [13].

2.1.4. Specific treatments for hypoxic tumours

Different treatments to improve the efficacy of radiotherapy in hypoxic tumours are currently under clinical investigation. These studies include methods that are intended to increase the oxygen delivery to tissue or radiosensitise hypoxic cells,

which is referred to as hypoxic modification [38]. An example is the inhalation of carbogen, a mixture of 5% carbon dioxide and 95% oxygen, in combination with the administration of nicotinamide, a drug enhancing tumour blood flow [39]. Another method is targeted to radiosensitise hypoxic cells by hyperthermia and drugs such as nimorazole [40].

Other promising approaches involve the application of radiation doses that are tailored to the radiosensitivity of a tumour as a whole or even to varying sensitivities within a particular tumour. These methods can be summarised under the term biologically adapted dose prescription [41–43]. Information from various biomarkers and imaging modalities may be combined and translated into a dose prescription for the RT treatment planning process. A brief summary of methods to assess hypoxia is given in Section 2.2.

In the context of this work, the biological property of interest is the hypoxic status of tumour tissue. In case parts of a tumour have been identified as hypoxic, the simplest method in this category is to increase the radiation dose in the whole macroscopic tumour volume. This approach might be limited by adverse reactions in normal healthy tissue. Adverse reactions occur, because in external beam RT the X-rays are applied from the outside of the patient and thus some dose is inevitably deposited in organs at risk in proximity to the tumour.

Therefore, other concepts intend to escalate the dose by a constant amount in hypoxic areas of the tumour only. This is referred to as dose painting by contours. Maybe the most appealing method, though also the most complex, is the application of different doses to small tumour sub-volumes. These doses are tailored to match the respective local radiosensitivity. This method does not aim at a homogeneous radiation dose distribution in the whole tumour volume, but at a dose distribution with the same biological effect in every sub-volume. Because the degree of hypoxia may vary strongly within a tumour, a homogeneous biological effect can imply a highly heterogeneous dose distribution. This approach is called dose painting by numbers [14–16].

None of the described treatment options has yet been clinically established, as the assessment of hypoxia in human tumours is difficult.

2.2. Assessment of tumour hypoxia

2.2.1. Overview of different methods

In many studies relating hypoxia to RT response, the tissue oxygen levels were measured using invasive techniques. Frequently, oxygen sensing probes were used, which are attached to a needle and punctured into tissue [10, 11]. With the

Eppendorf probe, a polarographic needle electrode, a current is measured that is proportional to the local PO_2 . The current is generated by electrochemical reduction of oxygen at the gold cathode of the probe [44]. The probes were found to be unsuited for routine clinical use for several reasons [13]. For example, they are invasive and may cause false measurements by influencing the tissue integrity. Also, not all tumour sites are accessible and the PO_2 is measured at a few locations along the linear needle tracks only. Therefore, it is not possible to assess the full tumour oxygenation in a spatially resolved manner.

As a consequence, different noninvasive imaging methods have been proposed to assess hypoxia. Methods based on widely available hardware are obviously the most reasonable candidates for clinical application. These typically are computed tomography (CT), magnetic resonance imaging (MRI) and positron emission tomography (PET). Measurements of the blood flow in a tissue volume element (voxel), i.e. the perfusion, are possible with all three modalities. Perfusion measurements with MRI and CT appear to be prognostic for RT outcome in HNSCC and cervical cancer, but results on the correlation between the perfusion and oxygenation measurements with alternative methods were conflicting [13]. An MRI method referred to as blood oxygen level dependent (BOLD) imaging may be applicable to assess hypoxia, which has been demonstrated in prostate cancer [45]. It is problematic that BOLD signals must be interpreted in combination with the local tissue perfusion, in order to obtain reliable information on the local degree of hypoxia [36].

The work presented in this thesis was focussed on dedicated hypoxia tracers for PET imaging, i.e. radiolabelled biomarkers that specifically accumulate in hypoxic tissue. Especially the radiolabelled 2-nitroimidazole compound [^{18}F]Fluoromisonidazole (FMISO) was investigated, which is one of the first hypoxia PET tracers that have been developed [46–48]. To date, FMISO is the most extensively studied hypoxia tracer [13]. In the next section a short description of the basic principles of PET imaging is given, followed by a more detailed outline of PET imaging using FMISO.

2.2.2. Basics of positron emission tomography (PET)

PET is a medical imaging modality used to measure different functional tissue properties in patients, which are identified using dedicated tracers, i.e. molecules that are labelled with a positron emitting radioisotope (e.g. ^{18}F , ^{15}O , $^{60/64}\text{Cu}$). Examples of functional properties that can be imaged with PET are glucose metabolism and hypoxia, using the tracers [^{18}F]Fluorodeoxyglucose (FDG) and FMISO, respectively. Solutions of the tracer molecules are intravenously administered to the patient. Emission scanning is performed following an uptake period,

which depends on several factors, such as the half-life of the radioisotope, the imaged organ and the retention mechanism of the particular tracer.

As functional data complements anatomical information, PET is combined with CT in modern imaging equipment (PET/CT) [49]. For oncological applications, PET/CT is ideally suited to combine measurements of cancer biology and anatomy. PET/CT might help to define RT target volumes more accurately or even individualise treatments as discussed in Section 2.1.4 for hypoxia as an important functional property. As biological changes often precede anatomical changes, tumour recurrences or metastases may be detected earlier with PET imaging, compared to anatomical imaging modalities [50].

In PET, it is possible to image concentrations of the radiolabelled tracers with temporal and spatial resolution. The radioisotopes used to label the molecules are positron emitters, i.e. they undergo a β^+ decay. For the frequently used marker ^{18}F this process reads:



where e^+ and ν_e denote a positron and an electron neutrino, respectively. Following the decay, the positron annihilates with an electron and two 511 keV photons are emitted in opposite directions, at an angle of approximately 180° . This process is depicted in Figure 2.2a. The high energy photons leave the patient and are detected in the PET scanner by arrays of scintillation crystals and photomultiplier tubes, which are aligned in rings around the patient [51].

The acquisition of a 3D image of the tracer concentration is based on the coincidence detection of the two annihilation photons, which is illustrated in Figure 2.2b. If two detections occur within a few nanoseconds, it is assumed that a radioisotope has decayed on the line connecting the two responding detectors, i.e. the line of response (LOR). This is a valid assumption, because the photons travel in opposite directions at the speed of light. In case there are D possible LORs, the raw data acquired by PET imaging are the numbers of coincidences detected on these LORs $n(1), n(2), \dots, n(D)$. The density distribution of the emitting radioisotopes in tissue, which is proportional to the density of tracer molecules $C(x, y, z)$, can be recovered from these data. The recovery is done using dedicated image reconstruction algorithms, such as filtered back projection [52] and maximum likelihood expectation maximisation [53].

A spatial resolution of about 4 mm (FWHM) is achieved with modern whole-body PET equipment [54]. The resolution is limited by several factors. Fundamental physical limitations are that the emitted positrons, due to their kinetic energy, have a mean free path of a few millimetres before annihilation. Moreover, a remaining total momentum of the e^+e^- pair at the instant of annihilation results in an angle between the emitted photons that differs slightly from 180° .

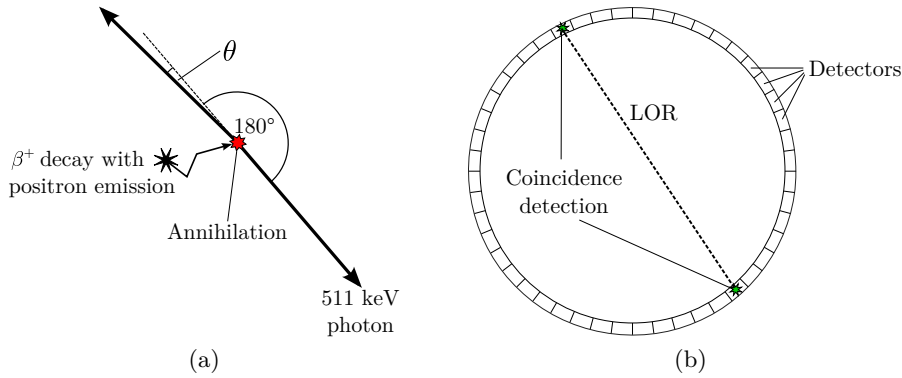


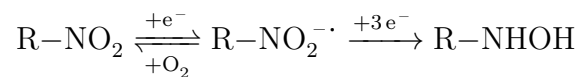
Figure 2.2.: (a) Diagram of the β^+ decay of radioisotopes used in PET and the subsequent e^+e^- annihilation generating two photons. The angle between the photon tracks differs by Θ from 180° . Typically $\Theta = 0.5^\circ$ (FWHM) [52]. (b) Coincidence detection of the annihilation photons in the PET scanner. Figures provided by courtesy of A. Horst (Section for Biomedical Physics, University Hospital Tübingen, Eberhard Karls University, Tübingen, Germany).

Other limitations are associated with the restricted count statistics, as only a small fraction of the emitted photons is detected as true coincidences and the total injected radioisotope dose is limited for medical reasons. Another important factor is the finite size of the discrete radiation detectors [51].

Emission scanning can be performed in dynamic mode, i.e. the acquisition of multiple image volumes at different timepoints post injection (pi) of the tracer.

2.2.3. PET imaging with [^{18}F]Fluoromisonidazole

FMISO is a PET tracer dedicated for the assessment of hypoxia in tumours. It can be denoted as $\text{R}-\text{NO}_2$, i.e. a nitro compound NO_2 attached to the rest R of the molecule. The bioreduction of $\text{R}-\text{NO}_2$ in cells involves multiple reduction steps. The first step is the conversion of NO_2 into a radical, which is reversed at a rate depending on the availability of molecular oxygen, i.e. a high reversal rate for high oxygen levels and *vice versa*. Due to this property, the subsequent accumulation of FMISO depends on the oxygen concentration and therefore is specific for hypoxia. In the following steps, further reactions occur and hydroxylamine (NHOH) is formed:



2. Background

Hydroxylamine binds to macromolecules in cells, such as nucleic acids and proteins, and remains confined for typical durations of a PET scan. As the reduction is mediated by enzymes, FMISO is retained in vital cells only [47]. The reduction process can be described by a first-order reaction rate constant that depends on the oxygen concentration [55]. This rate is fairly constant for PO_2 values above 20 mmHg and shows a steep increase below 10 mmHg [56].

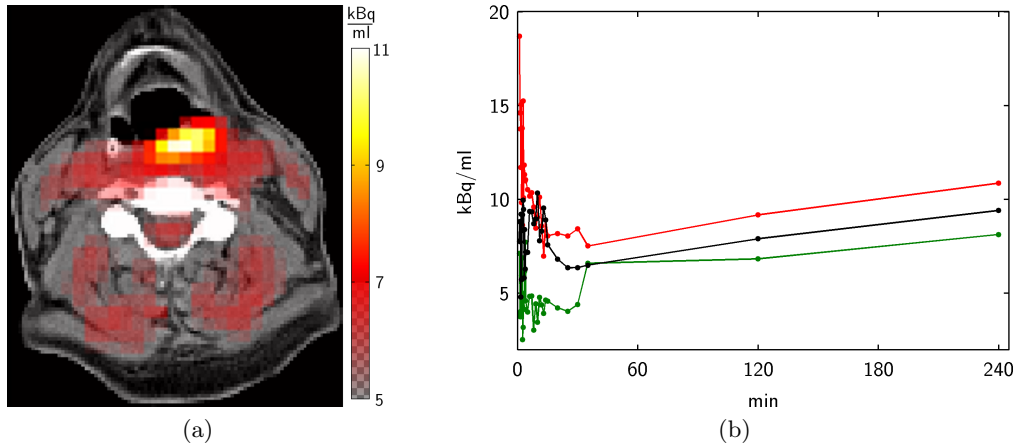


Figure 2.3.: (a) Transaxial slice of a clinical FMISO PET/CT image acquired 4 h pi in a patient with a tumour in the head and neck region. The FMISO concentration (red–white colour map) is overlaid on the CT (black–white). Parts of the tumour clearly exhibit a higher FMISO signal than the surrounding tissue, e.g. the neck muscles. (b) FMISO TACs for different voxels located in the tumour. In all voxels, tracer is accumulated at a similar rate (120–240 min). However, the signals differ strongly during the early phase (0–35 min). Imaging data provided by courtesy of D. Thorwarth (Section for Biomedical Physics, University Hospital Tübingen, Eberhard Karls University, Tübingen, Germany).

For application in PET imaging the positron emitter ^{18}F with a half-life of about 110 min is attached to the FMISO molecule [51]. After intravenous administration, FMISO distributes in the blood volume and enters soft tissue via blood vessel membranes. In tissue it is diffusively transported into hypoxic regions, which typically are located 70–100 μm from vessels [36]. Due to its balanced partition coefficient of 0.4 [57], FMISO readily crosses cell membranes and should be cleared from blood fairly quickly. The partition coefficient is a measure of lipophilicity. However, clearance observed by blood sampling in patients was quite slow, with a half-life of $T_{1/2} = 380$ min [48]. This is one explanation for the

relatively low contrast in FMISO PET images, compared to examinations using e.g. FDG. Maximum ratios between FMISO concentrations in tumour and blood (T/B) in general do not exceed 4.7 [12, 17, 29], but typically are considerably lower.

Typically, clinical FMISO PET images are reconstructed from signals that were collected during an acquisition period of about 15 min, following a uptake phase of more than two hours after tracer injection. Note that these are static images. A clinical example is shown in Figure 2.3a.

A major limitation of PET is its relatively low spatial resolution. Especially in hypoxia imaging this results in signals that are averaged over many differently oxygenated cells (cf. Figure 2.1a–b). This is referred to as partial volume effect (PVE). The PVE is another reason for the low contrast in FMISO PET images, because vital hypoxic cells, which exclusively retain the tracer, make up only a fraction of a voxel. Consequently, a voxel that has been classified as normoxic, based on the static FMISO PET signal, might still contain highly hypoxic islands embedded in normoxic or necrotic tissue regions [20]. This illustrates, how difficult it might be, to derive a reliable measure of hypoxia or of radiosensitivity from static signals on a voxel-by-voxel basis. For this reason, it has been proposed that dynamic PET scanning, commencing with the injection of the tracer, might give more conclusive information [17, 18, 58, 59]. As an example of dynamic acquisition, the FMISO density in three different tumour voxels is plotted over time in Figure 2.3b. These plots are referred to as time activity curves (TACs).

It is an open question whether FMISO PET strictly images chronic hypoxia, or is also influenced by acute hypoxia. This aspect is discussed especially regarding the reproducibility of FMISO PET scans, which is very important for its clinical implementation. In a clinical study, differences were found between two independent FMISO PET scans acquired within three days in untreated tumours [28]. It was hypothesised this might be the result of acute hypoxia. However, the findings could not be reproduced by a comparable study, in which much smaller differences were reported [29].

Alternative hypoxia PET tracers include other 2-nitroimidazole compounds, such as FAZA. FAZA has a lower partition coefficient than FMISO, i.e. it is more hydrophilic [60]. Therefore, its clearance from tissue might be faster and the PET image contrast higher. However, its distribution in tissue may be comparatively slow, as it does not cross cell membranes as easily as FMISO. A distinct hypoxia tracer is $^{60/64}\text{Cu}$ ATSM, labelled with different positron emitting copper isotopes. In contrast to 2-nitroimidazoles, it is based on a different and not yet completely understood oxygen-dependent retention mechanism [13]. It is very lipophilic and thus quickly distributes in tissue [61]. Accordingly, its tissue clearance is slow.

3. Biophysical Models, Materials and Simulation Methods

3.1. Diffusion-reaction models of O_2 and FMISO in tumour tissue

3.1.1. Outline

In this work, biophysical models of the behaviour of O_2 and FMISO in tumour tissue were used to simulate the dynamics of FMISO molecules in consecutive steps. This multistep approach, depicted in Figure 3.1, was proposed by Kelly *et al.* [24]. Here, their work was modified by using extended models, histology-based microvessel maps and a different numerical treatment of the model equations. Both models were intended to be representative for HNSCC. A model of oxygen transport and consumption was used to simulate static oxygen distributions. These served as input for a model of FMISO transport and retention with binding rates depending on the local PO_2 . For the oxygen model it was assumed that the underlying mechanisms and parameter values are known, so that predictive simulations of oxygenation maps for given vessel distributions are feasible. It can thus be classified as a predictive model, according to a classification scheme for theoretical models in biology [62]. In the FMISO model a comprehensive knowledge of the model equations was assumed as well, but not all parameters could be established from published data. Consequently, some parameters were optimised by comparing simulations with experimental data. This qualifies the model as being quantitative conceptual. Though, after establishing a set of parameters, the FMISO was also applied as a predictive model to the specific problems addressed in this work.

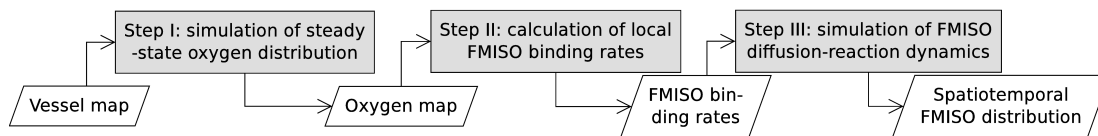


Figure 3.1.: Flowchart of the simulation process.

3.1.2. Oxygen transport and consumption

Oxygen is transported from the lungs to cells in tissue primarily in a haemoglobin bound state in red blood cells (RBCs) in the circulatory system. The release of O_2 from haemoglobin and subsequent diffusion through the RBC membrane, blood plasma, capillary wall, extracellular space and into the cells is a complex process, in which the molecules diffuse along concentration gradients. Because these processes are difficult to characterise experimentally, theoretical models have been developed that were reviewed in [63,64]. A method to reduce the complexity is to integrate the microscopical processes in mass transfer coefficients (MTCs) L_i . These coefficients link PO_2 gradients ΔP_i across each of the aforementioned tissue constituents i to the resulting O_2 fluxes $j_i = L_i \Delta P_i$. This is a formulation of Fick's law.

To make existing models applicable to the specific problem in this work, a single approximate MTC L_{O_2} was used. This lump coefficient comprises all transport steps between the RBC and the outside of the capillary wall driven by the corresponding PO_2 difference $P_{RBC} - P$. It was devised by fitting a quadratic function to modelled data and depends only on the RBC volume fraction in blood, i.e. the haematocrit H [65]:

$$L_{O_2} = 1.21 - 4.38H + 23.6H^2 \quad (3.1)$$

$$[L_{O_2}] = n l_{O_2} \text{ s}^{-1} \text{ mmHg}^{-1} \text{ cm}^{-2}. \quad (3.2)$$

The oxygen flux through the vessel wall into tissue was thus written as

$$\mathbf{j}_{O_2} = L_{O_2} (P - P_{RBC}) \mathbf{n}, \quad (3.3)$$

where \mathbf{n} denotes the normal unit vector pointing outward of each wall segment. Haematocrit H and intraerythrocytal P_{RBC} were set to values typical for tumour tissue. The perivascular P was variable, as it was part of the solution domain. The small O_2 molecules distribute diffusively in tissue and easily cross cell membranes. Therefore, a homogeneous diffusion coefficient D_{O_2} was assumed. Cells consume oxygen at a rate $M(P)$, which depends nonlinearly on the amount of proffered oxygen. This is typically modelled by a Michaelis-Menten relationship [64]:

$$M(P) = \frac{M_0 P}{P + P_0}. \quad (3.4)$$

For very high values of P cells consume oxygen at the maximum rate M_0 . With decreasing P the consumption decreases and reaches the half-maximum rate for $P = P_0$. The function is plotted in Figure 3.2. Cells exposed to very low oxygen pressures may become necrotic resulting in a decreased cell density. However, it

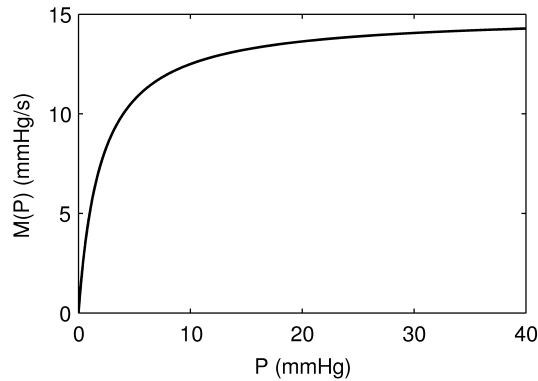


Figure 3.2.: Oxygen consumption as a function of PO_2 according to Equation (3.4). Parameter values from Table 3.1 were used.

was assumed that the oxygen demand of tissue is independent of the cell density. This is justified, because cells strongly decrease their oxygen consumption before critical partial pressures are reached, as modelled in Equation (3.4) describing the consumption rate. A small underestimation of the PO_2 far from supplying vessels might result from this assumption.

Finally, oxygen distribution and consumption were combined in a diffusion-reaction model [22, 23]:

$$\frac{\partial P}{\partial t} = D_{O_2} \nabla^2 P - M(P). \quad (3.5)$$

3.1.3. FMISO transport and retention

Another reaction-diffusion model was developed for the supply, distribution and retention of FMISO molecules. Basic model features presented in [24] were adapted and extended. Especially the relationship between PO_2 and tracer retention and the choice of parameters were revised. In contrast to O_2 , the transport of the larger FMISO molecules might be influenced by convection, due to their lower diffusion coefficient. However, transport of fluids across the capillary membrane results from hydrostatic and oncotic pressure differences. It is a frequent trait of tumours that both pressure differences are low due to the leaky nature of blood vessels in tumours [66, 67]. Consequently, convective transport of FMISO molecules across capillary membranes is negligible. As a result, the transmembrane FMISO flux \mathbf{j}_T only depends on the difference between the FMISO con-

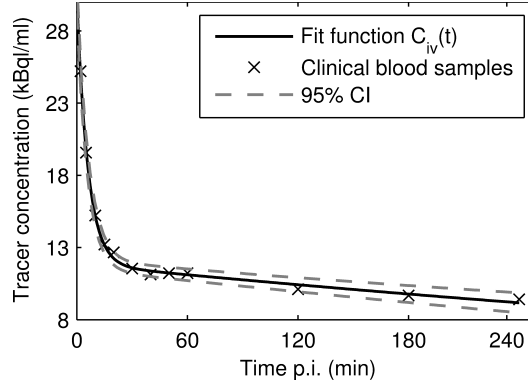


Figure 3.3.: Tracer blood input function $C_{iv}(t)$ according to Equation (3.7) used in this work. The parameter values specified in Table 3.1 were obtained by fitting it to clinical data.

centrations inside a blood vessel C_{iv} and in the adjoining tissue on the outside C :

$$\mathbf{j}_T = L_T (C - C_{iv}) \mathbf{n} \quad (3.6)$$

The tracer specific MTC and the normal unit vector are denoted by L_T and \mathbf{n} , respectively. As for O_2 , the tissue tracer concentration C is a variable in the simulation domain. The intravascular $C_{iv} = C_{iv}(t)$ is the time dependent blood tracer concentration in capillaries, which is defined by two major processes with distinct temporal characteristics. The rapid tracer distribution in the body after injection (time constant τ_1) is followed by a slow wash-out (τ_2). Experimental data were approximated by the model function

$$C_{iv}(t) = A_1 e^{-t/\tau_1} + A_2 e^{-t/\tau_2} \quad (3.7)$$

using the fit coefficients A_1 , A_2 , τ_1 and τ_2 . The input function used in this work is plotted in Figure 3.3. It is justified to neglect the initial increase of the blood tracer concentration after injection of the tracer bolus, because the distribution of the bolus in the blood volume is rapid (< 2 min). An overestimation by the model function for such short periods does not cause substantial errors in the simulations.

Tracer retention in cells is proportional to the available concentration of free tracer. The first order reaction rate of the binding process $K = K(P(x, y))$ is a nonlinear function of the local oxygen concentration, as depicted in Figure 3.4. Two multiplicative effects denoted by $F_1(P)$ and $F_2(P)$ were included:

$$K(P) = F_1(P) \cdot F_2(P) \quad (3.8)$$

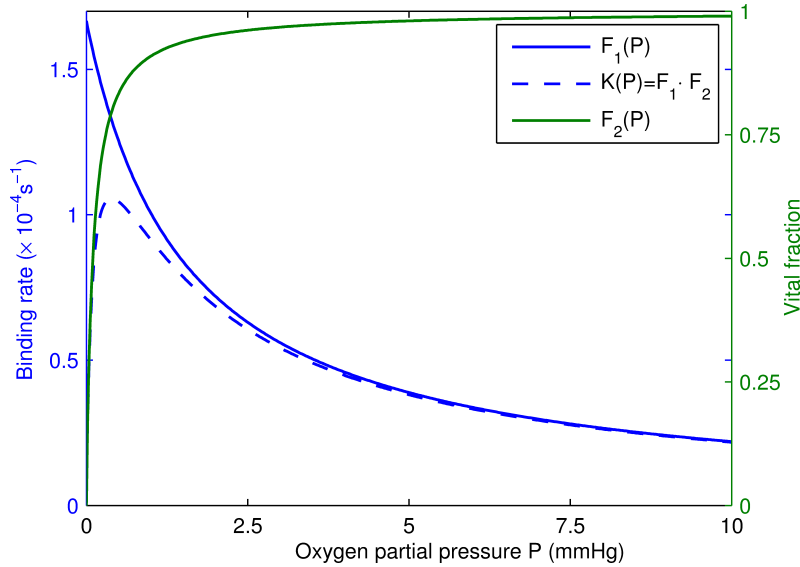


Figure 3.4.: First order reaction rate of FMISO as a function of the local oxygen concentration P .

The first effect is an increasing binding rate with decreasing PO_2 which reaches its half-maximum value $K_{\max}/2$ for $P = P_1$:

$$F_1(P) = \frac{K_{\max}P_1}{P + P_1}. \quad (3.9)$$

as derived by [55]. The second effect is that the reduction of FMISO in cells depends upon an active cellular metabolism [47]. Consequently, FMISO retention is diminished in regions with extremely low oxygen content, in which cells become necrotic. This was modelled by a function that is close to unity for large P , but drops to zero around $P = P_2$:

$$F_2(P) = \left(\frac{P}{P + P_2} \right)^k. \quad (3.10)$$

The steepness is controlled by the parameter k .

Transport of FMISO molecules in tumour tissue is dominated by diffusion, as human SCC have a very high content of glycosaminoglycans [68] and in this case convection is negligible for interstitial transport of compounds with low molecular weights [69]. A homogeneous diffusion coefficient D_T was assumed, as FMISO readily diffuses across cell membranes [36]. By separating the total tracer concentration C into a freely diffusing C_f and a bound C_b component ($C = C_f + C_b$),

the given assumptions were eventually expressed mathematically by two coupled partial differential equations (PDEs):

$$\begin{aligned}\frac{\partial C_f}{\partial t} &= D_T \nabla^2 C_f - K(P)C_f \\ \frac{\partial C_b}{\partial t} &= K(P)C_f.\end{aligned}\tag{3.11}$$

3.1.4. Parameter values

An overview of parameter values used in this work is given in Table 3.1. Ranges of realistic parameter values are naturally broad, because tumour physiology varies within a particular tumour and among tumours. Moreover, for some properties there are no accurate *in vivo* measurement methods, especially those that can be applied in humans. Most values were therefore taken from pre-clinical studies.

Table 3.1.: Parameter values for the diffusion-reaction models in Equations (3.5) and (3.11). Bold values were used where value ranges are specified.

| Symbol | Meaning | Value | Reference |
|------------------|---|---|--------------------------------|
| Oxygen | | | |
| P_{RBC} | Typical PO_2 in RBCs | 40 mmHg | [23] |
| H | Typical tumour haematocrit | 19 % | [70] |
| L_{O_2} | O_2 MTC | 4.1×10^{-4} m/s | [65] |
| D_{O_2} | O_2 diffusion coefficient | 2×10^{-9} m ² /s | [21] |
| M_0 | Max. O_2 consumption rate | 15 mmHg/s | [22] |
| P_0 | Michaelis-Menten coefficient | (2.0 – 2.5) mmHg | [22, 64] |
| Fmiso | | | |
| τ_1 | Time constant equilibration | 3.58×10^2 s | |
| τ_2 | Time constant washout | 5.63×10^4 s | Fit coefficients in |
| A_1 | Initial conc. equilibration | 18.5 kBq/ml | Equation (3.7) |
| A_2 | Initial conc. washout | 11.9 kBq/ml | |
| L_T | Transcapillary MTC | (2.4 – 9.4) $\times 10^{-5}$ m/s | [24] |
| D_T | MISO diffusion coefficient | 5.5×10^{-11} m ² /s | [71] |
| P_1 | PO_2 inhibiting binding by 50% | (0.8 – 1.5) mmHg | [46] |
| K_{max} | Max. binding rate (anoxia) | 1.7×10^{-4} s ⁻¹ | Optimised |
| P_2 | PO_2 inducing 50% necrosis | 0.1 mmHg | Simulated PO_2 |
| | | | 120 μm from vessels |
| k | Determines step width at P_2 | 0.3 | Optimised |

Oxygen

An intraerythrocyte PO_2 of $P_{RBC} = 40$ mmHg was assumed. This is the approximate value at arteriolar capillary ends. It decreases along the capillaries. The same value was used in previous studies [22,23]. A haematocrit value of $H = 19\%$, which was measured in mammary adenocarcinoma tumour models [70], was used to calculate the MTC of oxygen $L_{O_2} = 4.1 \times 10^{-4}$ m/s from Equation (3.1). This value lies slightly above the range given in [24]. The oxygen diffusion coefficient was set to $D_{O_2} = 2 \times 10^{-9}$ m²/s [21]. The maximum oxygen consumption rate M_0 is known only vaguely. A value of $M_0 = 15$ mmHg/s was used [22]. Generally, M_0 is proportional to the density of vital cells, which varies within a specific tumour as well as among different tumour entities. Published data for the Michaelis-Menten constant P_0 of the oxygen consumption model vary strongly. It was set to $P_0 = 2$ mmHg, in agreement with previous studies [22,64].

FMISO

The fit parameters defining the blood tracer concentration $C_{iv}(t)$ according to Equation (3.7) were derived from clinical data (cf. Figure 3.3). Decay-corrected measurements of the activity concentration in blood samples taken at different timepoints after tracer injection were used*.

The MTC of FMISO was set to $L_T = 2.4 \times 10^{-5}$ m/s, as given in [24]. This value may vary by two orders of magnitude for small molecules due to the increased vessel fenestration in tumours [72]. A diffusion coefficient of $D_T = 5.5 \times 10^{-11}$ m²/s measured for Misonidazole (MISO) in multicellular membranes of V79 hamster cells [71] is applicable for FMISO as well, because their molecular weights and partition coefficients are similar [57]. This is an effective value in tissue, consisting of cells enclosed by a membrane and extravascular space. MISO diffusion coefficients observed in multicellular membranes are significantly lower than in a medium without cells [71]. The tracer binding rate $K(P)$ is a function of the local PO_2 and is determined by the parameters P_1 , K_{max} , P_2 and k (cf. Equations (3.9) and (3.10)). It was found in different *in vitro* assays that 1000–2000 ppm O_2 inhibited binding by 50% compared to anoxia [46]. Hence, P_1 ranges from 0.8 mmHg to 1.5 mmHg. The parameter P_2 defines the PO_2 at which oxygen deprivation results in a 50% reduction of the cell density. Because oxygen distributions can be simulated without a model of the vital cell density, P_2 could be determined by the simulated PO_2 at a distance of about 120 μ m from vessels. This is a typical width of the vital cell layer around isolated vessels [21,73].

*Provided by courtesy of S.-M. Eschmann (Department of Nuclear Medicine, University Hospital Tübingen, Eberhard Karls University, Tübingen, Germany).

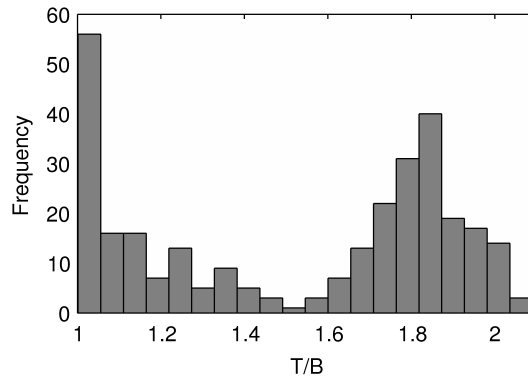


Figure 3.5.: Histogram of T/B ratios simulated in 2×2 mm regions.

The remaining parameters K_{\max} and k could not be established from published values and were determined heuristically. Values of $K_{\max} = 1.7 \times 10^{-4} \text{ s}^{-1}$ and $k = 0.3$ were chosen so that the simulated tracer concentrations 4 hpi result in voxel-based tumour T/B ratios that are comparable to clinical PET data. A histogram of simulated T/B ratios using these parameter values is shown in Figure 3.5. The simulated T/B ratios ranged from 1.00–2.09 with a mean value of 1.53. This is comparable to a clinical FMISO PET study in HNSCC, in which tumour to muscle ratios ranging from 1.10–3.44 with a mean of 1.72 were reported [17]. The maximum and mean simulated values were smaller than observed experimentally. This might for example represent variations in the dynamics of the blood tracer concentration. Specifically, a faster tracer wash-out can lead to higher T/B ratios.

3.2. Simulations of O_2 and FMISO diffusion-reaction dynamics

3.2.1. Outline

In the previous section, the diffusion-reaction models for oxygen and FMISO were established. In addition, the choice of model parameter values was discussed. In this section the methods used to simulate oxygen and FMISO distributions in microvessel networks are described. Specifically, it is detailed how vessel maps were created from tumour histology and how the model equations were solved numerically. In these aspects, the presented method is distinct from that presented by Kelly *et al.* [24]. They used distributions of identical vessels that were randomly placed in a tissue region according to single empirical parameters, e.g. typical

microvascular densities in tumours. Here, microvessel maps were used that were derived from real tissue samples to model the input and clearance of molecules. Due to the irregular vessel structures in these samples, it was necessary to use a finite element method (FEM) to solve the model equations numerically. Compared to the finite difference method employed by Kelly *et al.*, the FEM method is more flexible and efficient with respect to the discretisation of the solution domain.

3.2.2. Vessel maps from tumour histology

Material

Two-dimensional vessel maps were derived from fluorescence microscopy images of tumour tissue microsections[†]. Frozen tissue sections from human head and neck xenograft tumour lines were immunohistochemically stained for blood vessels using an antibody that marks endothelial cells in mice (9F1). The same sections were also stained for hypoxia using a marker that accumulates in hypoxic cells due to a binding mechanism similar to FMISO (pimonidazole hydrochloride). All tumour sections were scanned using a digital image analysis system resulting in grey-scale images for both fluorescent signals with a spatial resolution of $2.67 \mu\text{m}/\text{pixel}$. Details on this process were described previously [74, 75]. An example of the resulting images is given in Figure 3.6a.

Processing

Grey-scale images of vessel structures had to be converted to binary maps in order to model sources and sinks of oxygen and FMISO molecules in the simulations. In the first step, the image noise was reduced by bilateral filtering, which preserves edges. Therefore, the function *bfilter2* in MATLAB [76, 77] was used.

In the second step a threshold was applied to the filtered images in order to create binary data (Figure 3.6b). Threshold values were chosen according to the noise level in presumably avascular image regions. These values varied among images, which might result from varying conditions during image scanning or from variations in the application of the vessel marker. In some cases the value was adjusted manually according to a visual inspection.

In the last step the binary vessel maps were coarsened by combining 3×3 pixels (Figure 3.6c). The circumference of the resulting $8.00 \mu\text{m}$ pixels was similar to that of a vessel with a circular profile and a diameter of $10 \mu\text{m}$, which is roughly the smallest physiologically realistic value. The resulting pixel represents a vessel

[†]Provided by courtesy of E. Troost (Department of Radiation Oncology, Radboud University Nijmegen Medical Centre, Nijmegen, The Netherlands).

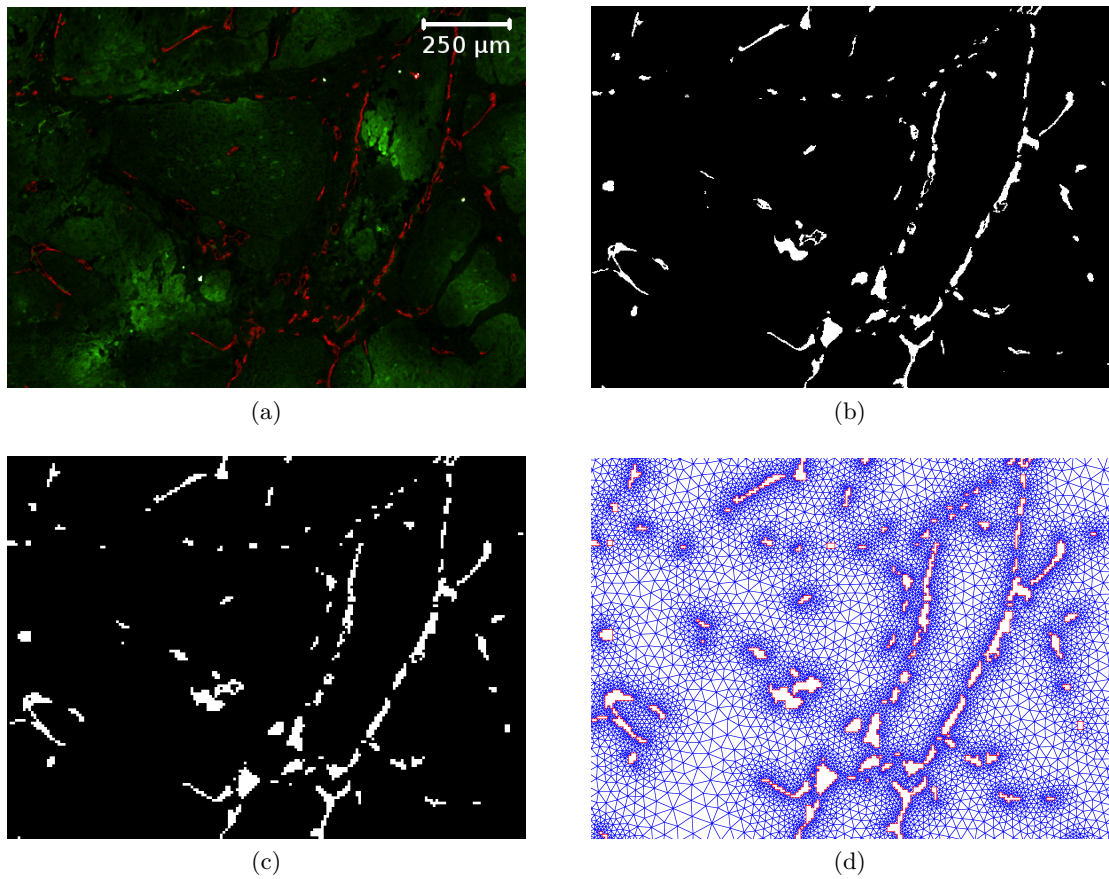


Figure 3.6.: (a) Combined false-colour images of the fluorescent signals from staining for vessel endothelium (red) and hypoxic cells (green). (b) Vessel structures from (a) after bilateral filtering and thresholding. (c) Vessel map after additional coarsening, which removed small staining artifacts. (d) Triangular FEM mesh derived from the coarsened map. Vessel boundaries are red.

(value 1) only if at least three of the contained pixels have value 1. This procedure removes staining artifacts from the map that are too small to represent the profile of a microvessel. Moreover, it has the advantage of restricting the computer memory demand of the employed numerical methods, because the size of the FEM mesh strongly depends on the minimum size of structures in the map.

3.2.3. Numerical methods

Creating triangular meshes from vessel maps

Solving the diffusion-reaction equations (3.5) and (3.11) numerically with the FEM requires a description of the 2D solution domain Ω . This description is created by discretising the given geometry into triangles of different shapes and sizes. The result is called a triangular mesh and the points in which triangle corners join are called nodes. In this work, the geometry was defined by the vessel maps that were created as described in the previous section. Based on the maps a mesh was generated using a routine in MATLAB which creates a Delaunay triangulation. The extravascular space was tessellated with triangles, sparing vessel interiors from Ω . Thus, vessel surfaces $\partial\Omega_v$ and the outer edges of the map $\partial\Omega_e$ form the 1D boundary $\partial\Omega = \partial\Omega_v \cup \partial\Omega_e$ of the domain Ω . An example of a mesh is shown in Figure 3.6d.

Differential equations and boundary conditions

The diffusion-reaction equations (3.5) and (3.11) are parabolic PDEs. A more general formulation of these PDE problems is: find a solution $u = u(x, y, t)$ that satisfies the equation

$$\frac{\partial u}{\partial t} = c\nabla^2 u - au \quad (3.12)$$

in the bounded 2D domain Ω . The problem-specific coefficients are denoted by c and a . The construction of Ω was described in the previous section. For a full description of the problem, initial values $u(x, y, 0) = u_0(x, y)$ for $x, y \in \Omega$ and boundary conditions on $\partial\Omega$ must be specified. Coefficients and initial values u_0 specific to the oxygen and FMISO diffusion-reaction problems are given in Table 3.2. For the two coupled PDEs of the FMISO model these coefficients are two-element vectors. Robin and Neumann type boundary conditions were used in this work. With Robin boundary conditions the flux $\mathbf{j} = -c\nabla u$ across a boundary segment can be specified by

$$\mathbf{j} = (qu - g) \mathbf{n} \quad (3.13)$$

with problem specific coefficients q and g . This is equivalent to setting the gradient ∇u to a fixed value on the segment. Robin conditions were applied to vessel boundary segments $\partial\Omega_v$ in order to define the transmembrane flux of molecules according to Equations (3.3) and (3.6). By applying Neumann boundary conditions the net flux across a boundary element is set to zero: $\mathbf{j} = 0$. In the context of this work, Neumann conditions were applied to the outer boundaries of vessel maps $\partial\Omega_e$, so that there is no net molecular transport across them. This assumption implies a certain symmetry in the virtual continuation of a given vessel map outside its outer edges. For example, a copy of the original map mirrored on the specific edge fulfils the no-flux condition.

Table 3.2.: Problem-specific PDE coefficients. These can be derived by comparing the general equations (3.12) and (3.13) with equations (3.5) and (3.3) for oxygen as well as with equations (3.11) and (3.6) for FMISO.

| | Oxygen | FMISO |
|-------|-------------------------|---|
| u | $P(x, y, t)$ | $(C_f(x, y, t) \quad C_b(x, y, t))$ |
| u_0 | 0 mmHg | $(0 \text{ kBq/ml} \quad 0 \text{ kBq/ml})$ |
| c | D_{O_2} | $(D_T \quad 0)$ |
| a | $M(P)/P$ | $(K(P) \quad -K(P))$ |
| q | L_{O_2} | $(L_T \quad 0)$ |
| g | $L_{O_2} \cdot P_{RBC}$ | $(L_T \cdot C_{iv} \quad 0)$ |

Problem-specific finite element method in 2D

A short problem-specific summary of the FEM is given here, which is based on an outline in [78]. To find an approximate solution $u_h(x, y, t)$ of the PDE problem, u_h is expanded in a set of basis functions ϕ_i , $i = 1, \dots, N_p$

$$u_h(x, y, t) = \sum_{i=1}^{N_p} U_i(t) \phi_i(x, y) \quad (3.14)$$

where N_p denotes the number of mesh nodes and $U_i(t)$ are time-dependent coefficients that have to be found. Typically, piecewise linear functions ϕ_i are chosen that take on the value 1 at node i and the value 0 at all other nodes. Then, the variational formulation of the PDE problem in Equation (3.12) is to find U_i , so that

$$\int_{\Omega} \left(\frac{\partial u_h}{\partial t} - c \nabla^2 u_h + a u_h \right) \phi_j dx dy = 0 \quad \forall j = 1, \dots, N_p. \quad (3.15)$$

The boundary and initial value conditions must also be fulfilled. Note that the test functions ϕ_j are from the same set of piecewise linear functions as in the expansion of u_h . Combining Equations (3.14) and (3.15) and using Green's identity together with the boundary conditions in Equation (3.13) results in a system of linear ordinary differential equations (ODEs):

$$M \frac{dU}{dt} + KU = F \quad (3.16)$$

with

$$\begin{aligned} M_{j,i} &= \int_{\Omega} \phi_i \phi_j \, dx \, dy \\ K_{j,i} &= \int_{\Omega} ((c \nabla \phi_i) \nabla \phi_j + a \phi_i \phi_j) \, dx \, dy + \int_{\partial\Omega} q \phi_i \phi_j \, ds \\ F_j &= \int_{\partial\Omega} g \phi_j \, ds. \end{aligned}$$

By solving this ODE the coefficients U_i and thus the approximate solution u_h can be obtained. For the problems in this work this system is very large, N_p typically is on the order of 10^5 . The product $\phi_i \phi_j$ is zero for most combinations of i and j , because the basis function ϕ_k is non-zero only on a few triangles adjoining node k of the FEM mesh. Thus, the matrices M and K are sparse, i.e. that most elements are zero. The function *parabolic* in MATLAB was used to assemble M , K and F and to solve Equation (3.16) numerically with an integrated ODE solver.

3.2.4. Simulation procedure and data processing

Spatio-temporal FMISO distributions were simulated in three-steps, which are outlined in Figure 3.1. In the first step, the steady-state oxygen distribution P_{eq} for a specific vessel map was calculated. For the oxygen case the diffusion-reaction PDE is nonlinear, because the coefficient $a = M(P)/P$ is a nonlinear function of P . As nonlinear PDEs can not be handled with the routine *parabolic*, the problem was linearised by calculating P_{eq} iteratively. Based on the result of each time step, the coefficient a was reevaluated and used as input for the following step. The iteration was interrupted when the maximum variation of P during one iteration step was below 0.1%.

In the second step the local FMISO binding rates were calculated from the steady-state oxygen distribution $K(P_{\text{eq}}(x, y))$ according to Equation (3.8). This was followed by the solution of the FMISO diffusion-reaction equation. Solution values were given at each node of the FEM mesh and for each predefined timepoint.

By averaging the tracer concentration in different regions of interest (ROIs) time activity curves (TACs) were calculated. In addition to the average concentration of free C_f and bound C_b tracer, the amount of tracer in blood vessels $C_{iv}(t)$ was included according to the vascular fraction in the specific region. In this way, features of simulated TACs could be compared with pre-clinical and clinical PET TACs. The advantages of the presented theoretical method are that the microscopical tracer distributions underlying a TAC are known and that the free, bound and intravascular tracer components can be evaluated separately. Simulated TACs must be interpreted as approximate PET TACs, because influences of PET image acquisition and reconstruction on the measured signal were not simulated. In other words, an idealised PET scanner was assumed that recovers signals from small cubic regions without noise or blurring.

3.3. Validation of the simulation method

Validating the simulation method is very difficult. For a rigorous microscopic validation, high resolution 2D or 3D measurements of the spatial distribution of oxygen and FMISO would be necessary. Temporally resolved data would be needed for FMISO to validate the dynamic component. Additionally, the corresponding vascular structures would have to be known. Because such detailed experimental data do not exist, it was confirmed that the simulated results are consistent with the available information.

The simulated PO_2 strongly decreases with increasing distance from vessels. Typically, the PO_2 is smaller than 0.1 mmHg at a distance of about 120 μm from vessels. Values of zero are reached only asymptotically, as the oxygen consumption $M(P)$ tends towards zero in line with decreasing PO_2 . Similar empirical data were reported for the distance at which PO_2 falls to zero [21]. The median simulated PO_2 for all vessel maps used in this work was 10.0 mmHg. It was calculated from oxygen maps with resolutions of 50 $\mu\text{m}/\text{pixel}$, which is comparable to the measurement volume of polarographic oxygen sensing electrodes [79]. The median PO_2 measured with such electrodes in clinical HNSCC by different institutions ranged from 5 mmHg to 18 mmHg [11]. This makes it plausible that the manifold oxygenations in human SCCHN were adequately represented by the simulations.

In order to evaluate the FMISO model the aspects of tracer retention and transport were investigated independently. FMISO retention patterns were qualitatively compared against the pimonidazole IHC staining for identical vessel maps. A high visual concordance between the patterns was found. For example in Figures 3.7a and c, the maximum uptake of FMISO and pimonidazole occurs at roughly the same distance from vessels. In Figures 3.7b and d, a good agreement

between areas of low simulated FMISO retention and low pimonidazole intensity associated with cell necrosis can be observed (white arrow). Despite apparent similarities between the retention patterns, quantitative correlations were very low. Possible reasons for this are that the pimonidazole stainings are cross-sections from three-dimensional material, while FMISO is simulated in a 2D plane. There might also be a disparity between the two markers regarding the PO_2 dependence of the binding rate. Another effect that might contribute to a low correlation can be identified in Figure 3.7a. In some regions high pimonidazole intensities overlap with a vessel (white arrow). This indicates that the vessel did not properly supply oxygen during uptake period of the marker, which may be explained by acute hypoxia. Nonetheless, in the FMISO simulations a normal oxygen supply by this particular vessel was assumed and there is no retention overlapping with the vessel, as can be seen in Figure 3.7c.

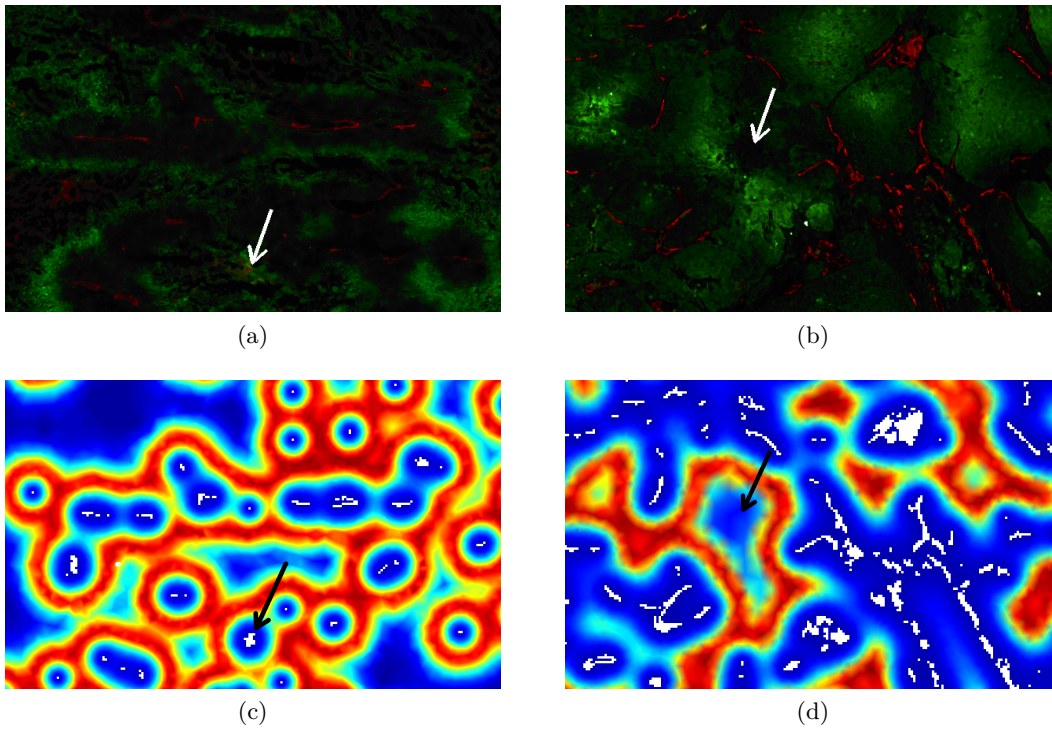


Figure 3.7.: (a), (b): Details of two different IHC stained tissue sections ($1.69 \text{ mm} \times 1.04 \text{ mm}$). Vessels are red and hypoxia is green. (c), (d): Concentrations of bound FMISO 4 h pi $C_b(t = 4 \text{ h})$ simulated based on vessel maps derived from (a) and (b), respectively.

Furthermore, the FMISO simulation model was validated by comparing clinical and simulated TACs, which is shown in Figure 3.8. Two characteristics can be distinguished in the curves, a highly variable component initially after tracer injection, which is followed by an almost linear progress. The early component represents the distribution of the tracer molecules, injected as a bolus into the blood volume, in the entire tissue volume. It is thus referred to as input peak. After a state has been reached that is closer to equilibrium, the curves are dominated by the superposition of tracer accumulation in hypoxic cells and clearance of free tracer. During this phase tracer molecules are cleared from tissue via vessels. This component is therefore called the uptake curve. The transition between the two phases is completed when the curves become linear. These timepoints strongly depend on the vessel density in the map as well as the mass transfer and diffusion coefficients of FMISO. Also, the binding rate properties of FMISO play a role. Thus, the timepoint of completed transition is an ideal parameter to check the overall plausibility of the FMISO simulations.

Three distinct clinical FMISO PET TACs[‡] were used as references (Figure 3.8d). Simulated TACs were evaluated in ROIs that were chosen so that the resulting overall curve shapes were comparable (Figure 3.8c). It could not be investigated if microvessel networks underlying real and simulated data were similar, because this information is unavailable for clinical PET voxels. Nonetheless, there is a very good agreement in terms of the transition timepoints. It appears that for a specific clinical TAC it is generally possible to find a similar simulated TAC in the available vessel maps. Thus, tracer input across capillary membranes and subsequent distribution in tissue seems to be adequately reproduced by the model and simulation method in combination with the chosen parameter values. It also appears that the properties of vessel maps, e.g. the heterogeneity of vessel distributions, cover a realistic range.

[‡]Provided by courtesy of D. Thorwarth (Section for Biomedical Physics, University Hospital Tübingen, Eberhard Karls University, Tübingen, Germany)

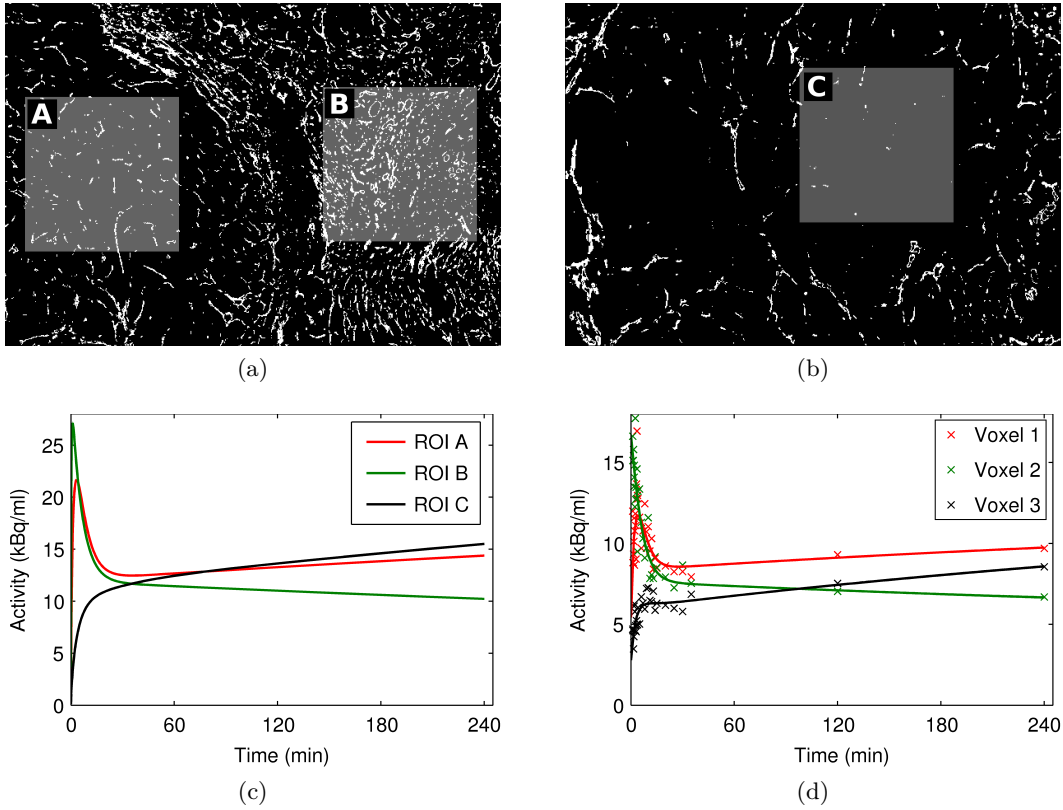


Figure 3.8.: (a) Vessel map highlighting $1.5 \times 1.5 \text{ mm}^2$ ROIs with intermediate (A) and high vessel density (B). (b) Low vessel density in a different map (C). (c) TACs were simulated by averaging the total tracer concentration in the respective ROI. Note the distinct curve shapes. Curves are almost linear after 40 min, 41 min and 109 min in ROI A, B and C, respectively. (d) Clinical voxel-based FMISO PET TACs in a HNSCC. Voxels 1 and 2 were located in the centre and at the edge of the tumour, respectively. Voxel 3 was located in a metastatic lymph node. Fits were plotted as solid lines. Curves are linear after 33 min, 38 min and 105 min in voxel 1, 2 and 3, respectively.

4. Results and Discussion

4.1. Fundamentals of FMISO PET signal formation

4.1.1. Outline

Intervessel distances in tumour tissue are typically large. This is generally accepted as the cause of chronic hypoxia, in combination with the chaotic arrangement of vessels, that is lacking a proper hierarchy and shows other aberrations, such as blind endings and plasma flow [8, 80]. The fact that hypoxic cells are located at relatively large distances from vessels might pose an obstacle for FMISO molecules to reach these cells and accumulate there, as it distributes passively by diffusion. Another effect of large intervessel distances might be a slow equilibration between the injected bolus of tracer molecules and remote tissue regions. This is comprehensible considering that the expected distance a particle diffusing in 2D has travelled from its starting point in a time interval Δt is given by the root-mean-squared distance $d_{\text{RMS}} = \sqrt{4D\Delta t}$ [81]. D denotes the diffusion coefficient of the particle in a given medium. As a consequence, small changes of intervessel distances have a large effect on the distribution of particles. It takes particles four times as long to travel twice as far. Interpreted in the context of this work, it takes about 46 s for an FMISO molecule ($D_T = 5.5 \times 10^{-11} \text{ m}^2/\text{s}$, cf. Table 3.1) to reach hypoxic cells, which are located about 100 μm from vessels. To reach necrotic tissue, located for example 300 μm from vessels, it takes 409 s.

Both effects allow to hypothesise that it might take a long time before FMISO signals effectively represent FMISO accumulation that is specific for tumour hypoxia. This is an important issue for the design of FMISO PET acquisition protocols. In the following, this aspect is studied based on the simulation method developed in this thesis, making use of its capability to simulate the distribution of FMISO in tissue with very high spatial and temporal resolution.

Another hypothesis is that the equilibration between blood and tissue is faster in regions with high vessel densities and regularly arranged vessels, leading to higher FMISO signals in the early wash-in phase. Therefore, early signals may be used as a measure of perfusion by the embedded vessel configuration. Evidence for this relationship has been found in clinical studies comparing FMISO or FAZA PET scans with scans using radiolabelled water, i.e. $^{15}\text{O}]\text{H}_2\text{O}$ [82, 83]. The latter

molecule is a PET tracer dedicated to perfusion imaging. It might be possible to gather a more reliable prediction of the latent RT response with an FMISO PET examination, if the perfusion is analysed in combination with the accumulation data [17, 18]. Therefore, the second aspect studied in the following is, whether early and late FMISO PET signals contain distinct information.

4.1.2. Results

In this study a single microscopic tissue section was converted into a square vessel map with an edge length of 3.94 mm, which is shown in Figure 4.1a. The overall vascular fraction was 3.0%. Within this map three square ROIs with edge lengths of 0.63 mm were manually selected. The ROIs comprise vessel distributions that are distinct with respect to their vessel densities. The vascular fraction was 7.9%, 2.9%, and 1.2% in ROI A, B, and C, respectively. Simulations of the corresponding static oxygen distribution and subsequently the FMISO dynamics were performed as described in Section 3.2.

The oxygen distribution used to calculate FMISO binding rates is shown in Figure 4.1b. Maximum PO_2 values in proximity to vessels are close to the modelled PO_2 in red blood cells of 40 mmHg. This value strongly decreases with increasing distance from vessels. At a distance of about 120 μm the PO_2 typically is below 0.1 mmHg. The mean simulated PO_2 for this specific map was 8.8 mmHg, irrespective of whether the oxygen maps were sampled at a resolution of 50 $\mu\text{m}/\text{pixel}$ or 5 $\mu\text{m}/\text{pixel}$. As the former is close to the spatial resolution of polarographic electrodes, this theoretical result corroborates that the resolution of the electrodes is sufficient to capture representative microscopic PO_2 values. The mean PO_2 in the ROIs was 18.1 mmHg, 14.0 mmHg and 2.4 mmHg, in ROI A, B and C, respectively.

Simulated FMISO distributions are displayed in Figures 4.1c–f for different timepoints after injection (pi). The early distribution 4 min pi is clearly dominated by freely diffusing tracer molecules entering the tissue via vessels (Figure 4.1c). Subsequently, the molecules gradually spread into regions further from vessels. However, 15 min pi there still are considerable heterogeneities, with lower tracer concentrations in regions distant from vessels (Figure 4.1d). Apparently, these regions are still not equilibrated with the supply of tracer from vessels. Moreover, at 15 min pi the first hint of a concentration contrast appears that can actually be attributed to FMISO retention. This contrast gradually increases with increasing uptake time (Figures 4.1e–f). The resulting FMISO patterns predominantly appear like ribbons around vessels. The concentration strongly increases with increasing distance from vessels, then reaches a maximum and declines again. This mirrors the PO_2 -dependence of the tracer binding rate modelled by Equation

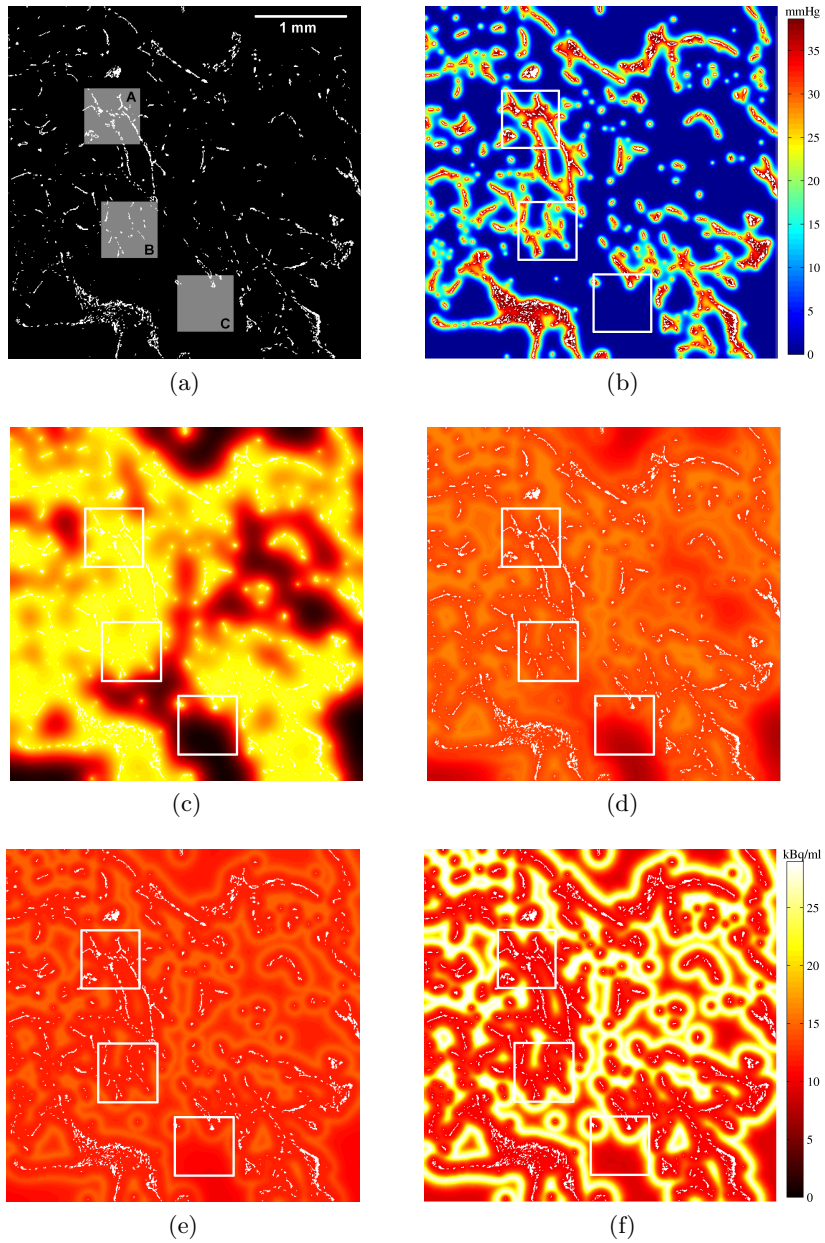


Figure 4.1.: (a) Vessel map and ROIs used in this study. (b) Corresponding simulated static O_2 distribution $P_{eq}(x, y)$. (c)–(f) Simulated total FMISO concentration $C(x, y, t)$ for $t = 4$ min (c), 15 min (d), 30 min (e) and 240 min (f) (colour bar applies to all).

(3.8). The increase is associated with an increasing retention of FMISO in hypoxic cells, while the following decline is caused by a reduced cell density due to necrosis. It is evident that low FMISO retention several hours pi may indicate normoxic (high PO_2) as well as predominantly necrotic (extremely low PO_2) tissue. Similar findings were reported for IHC experiments investigating the microscopic nature of hypoxia: ribbon-like patterns of pimonidazole binding were observed in tumour models [7].

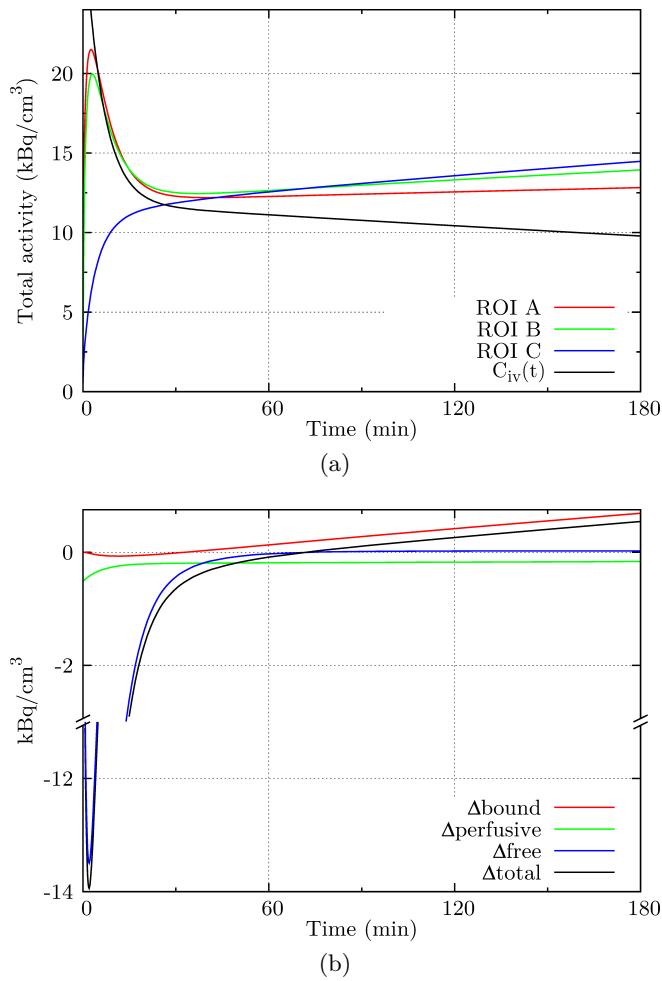


Figure 4.2.: (a) Simulated TACs for the ROIs outlined in Figure 4.1. The modelled tracer input function $C_{iv}(t)$ is shown in black. (b) Differences between the tracer signal components of ROIs B and C ($\Delta = C - B$).

Time activity curves (TACs) were derived from the simulated data by averaging the tracer concentrations in ROIs A, B and C for each timepoint. As shown in Figure 4.2a, curves with distinct shapes emanate from each region. There is a correspondence between the shape of the initial signals, i.e. the input peaks, and the underlying vessel distributions. Pronounced peaks belong to regions A and B, which exhibit high vascular densities and relatively homogeneous vessel distributions. Obviously, the tracer concentrations in these regions are strongly coupled to the intravascular component $C_{iv}(t)$. The maximum value of peak A is slightly larger than in peak B, which can be explained by the higher vessel density in A. On the other hand, the almost avascular region C is characterised by a very shallow initial curve without a peak value. Regarding the uptake curves 60–180 min pi, region A shows a slower FMISO retention than regions B and C. By comparing curve A with the plotted input function it can be seen that some tracer is accumulated in A as well. Therefore, it is not a pure wash-out type region. Most remarkably, the uptake curves of B and C are similar, even though the underlying microvessel networks differ strongly. The net tracer uptake rate is slightly higher in C than in B. In contrast, the total signal in C is lower up to about 70 min pi. This inconsistency between the total FMISO signal and the net uptake rate was further investigated by separately evaluating the components of the signal. These are (1) the perfusive component in vessels, (2) the free and (3) the bound tracer component in tissue. Differences between these components in regions B and C are plotted in Figure 4.2b. The observations for each component are:

- (1) Perfusion: The negative difference in the perfusive component shows that the signal originating from vessels is larger in region B than in C. Obviously, this is due to different vascular volumes in the regions.
- (2) Free tracer: There is a large initial difference between the average free tracer concentrations, because tracer molecules distribute much quicker in region B. Nevertheless, this difference vanishes almost completely for timepoints later than 60 min pi. This is contradictory, as the extravascular space, which the tracer distributes in, is larger in region C than in B. Thus, if both regions were equilibrated with the intravascular component, one would expect a higher contribution of free tracer to the total signal in region C. As this is not the case, free tracer levels must be lower in some areas of region C than in B. Such lower concentrations are vaguely discernible 4 h pi in the avascular bottom part of C in Figure 4.1f. It can be argued that the reason is the slow coupling between the tracer input and distant areas due to diffusion restrictions.

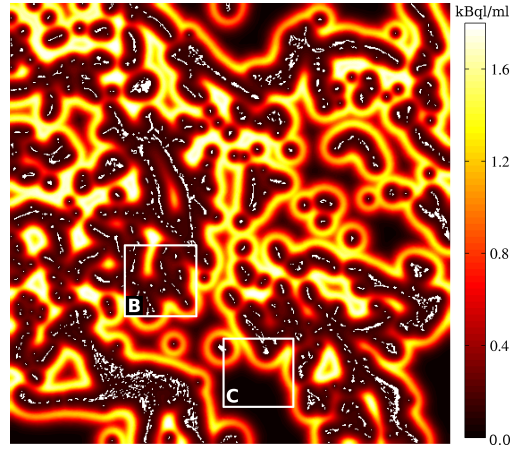


Figure 4.3.: Simulated bound FMISO concentration $C_b(x, y, t = 15 \text{ min})$. The tracer retention in ribbon-like patterns around vessels is anisotropic. It is lower in direction towards avascular regions than in direction towards regions with a high vessel density.

- (3) Bound tracer: Interestingly, the bound tracer concentration is higher in B up to about 30 min pi, even though this region displays a considerably higher vessel density and mean PO_2 . Later this is compensated by the higher net binding rate in region C. This initial anti-specific binding is a direct consequence of the slow distribution of tracer in tissue. More specifically, tracer binding is proportional to the amount of proffered tracer according to Equation (3.11). Initially, more tracer is bound in hypoxic areas of region B than in C, which can be seen in Figure 4.3 showing the bound tracer concentration 15 min pi. Clearly, less tracer was bound around vessels that supply tracer to large tissue areas. In the same figure, this effect can also be identified in vessels on the edges of highly vascularised regions. There, tracer accumulation is anisotropic, i.e. it is lower in direction towards avascular regions than in direction towards regions with a high vessel density.

Altogether, these effects explain why it takes more than one hour until the total FMISO signal in region C is higher than in B. It is corroborated that the diffusive transport, which is slow compared to typical intervessel distances, is an important factor determining signal formation. More generally, the results give evidence that a sufficiently long tracer uptake period is mandatory, in order to obtain a consistent FMISO image contrast in terms of a stable sign.

Furthermore, the results indicate that there is a correspondence between prop-

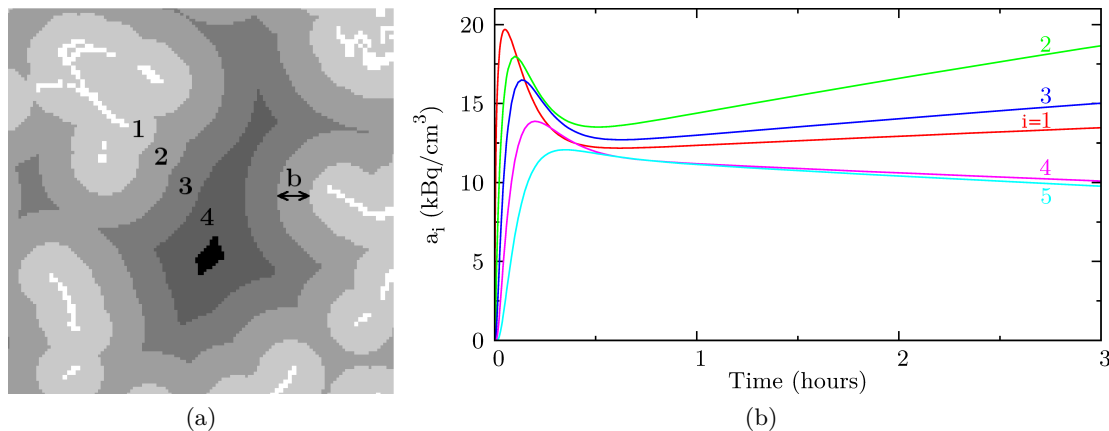


Figure 4.4.: (a) Concentric layers around vessels (width $b = 50 \mu\text{m}$). (b) TAC decomposed into sub-TACs $a_1(t), \dots, a_5(t)$ for each layer. The weights $w_1 = 0.38$, $w_2 = 0.36$, $w_3 = 0.16$, $w_4 = 0.04$, $w_5 = 0.02$ correspond to the respective areas occupied by the layers.

erties of the microvascular network and the input peak shape. It was analysed in detail whether this information is redundant with the information from tracer retention, i.e. whether the magnitude of the input peak is inversely related to the tracer uptake. Therefore, the simulated TAC $A(t)$ of the vessel map in Figure 4.4a was decomposed into a weighted superposition of sub-TACs $a_i(t)$, $i = 1, \dots, 5$ originating from concentric layers around vessels

$$A(t) = \sum_{i=1}^5 w_i a_i(t).$$

The weights are denoted by w_i . Each type of sub-TAC may be interpreted to represent a tissue volume, in which the typical distance between cells and vessels lies within the range of the layer that is covered by the specific sub-TAC.

The resulting sub-TACs are shown in Figure 4.4b. A gradual change of the input peak with increasing distance from the nearest vessel can be observed, i.e. the maximum value decreases and the peak becomes wider. Moreover, the position of the peak is shifted towards later timepoints. This monotonic behaviour is not found in the uptake curves, where an increase of the slope from layer 1 to layer 2 is followed by decreasing slopes for the more distant layers. Apparently, layer 2 comprises most of the ribbon-like uptake regions, as it covers distances from $50 \mu\text{m}$ to $100 \mu\text{m}$. Necrosis dominates layers at distances larger than $150 \mu\text{m}$, in particular

layers 4 and 5. In these layers the uptake rates are low, as FMISO is retained in vital cells only. This clearly demonstrates that the tracer input peak conveys independent information about the respective tissue region. For example, it might help to resolve problems that are associated with the intrinsically ambiguous FMISO binding, i.e. a low retention in normoxic as well as necrotic tissue.

4.1.3. Discussion

The aim of FMISO PET imaging is to measure hypoxia by means of the oxygen-dependent retention of the radiolabelled molecule. The results show that the supply of FMISO molecules to tissue regions located far from vessels is dilatory. This effect can mask hypoxia-specific tracer retention in the total FMISO signal for a considerable period following tracer injection. As large intervessel distances are common in hypoxic tumours, it is necessary to acquire static FMISO PET images after a sufficiently long uptake period. Not all recent clinical hypoxia PET studies have regarded this aspect, for example in [83] FAZA PET imaging has been performed up to 1 h pi only. Clearly, longer uptake periods compete with decreasing decay rates of the injected ^{18}F radioisotopes, which determine the count statistics of the PET acquisition.

The results of this study show that the quantification of FMISO uptake from static images is problematic, because the contrast between PET voxels is unstable. For example, the ratios between the signals from ROIs A, B and C in Figure 4.2a strongly depend on the imaging timepoint. A robust quantification of the net uptake rate in a voxel requires the acquisition of at least two image volumes at different timepoints pi during the uptake phase, for example 2 h and 4 h. Nevertheless, most clinical studies were so far limited to the analysis of single static scans [12, 84]. A consistent quantification is for instance necessary to segment hypoxic volumes in FMISO PET images in a reliable manner, regardless whether these volumes are defined manually or by automatic algorithms [85]. These volumes may be used in RT to perform a dose escalation by dose painting by contours [86]. The requirements for dose painting by numbers based on FMISO PET are even higher, because the dose is not escalated using a binary criterion, i.e. inside/outside the contour, but it is prescribed according to a voxel-based metric.

In order to obtain a stable measure of hypoxia, a method has been proposed to quantitatively analyse dynamic FMISO PET data that were acquired over several hours pi [87]. Dynamic imaging in patients is technically demanding and time consuming. For the analysis of dynamic data a suitable compartmental model of the tracer kinetics has to be established [55]. The free coefficients of this model can then be fitted to voxel-based FMISO PET TACs. Parametric

maps can subsequently be created by combining these coefficients in a single value. In this way a parameter that correlates with RT outcome was derived [18]. It combined two kinetic model coefficients characterising the hypoxia-associated retention (late signal) and the vessel architecture (early signal) in a PET voxel, respectively. The results presented here corroborate the interpretation that there is a connection between early FMISO PET signals and the underlying vessel architecture. As a consequence, it is proposed in Section 4.3 that the combination of a late and an early static FMISO PET scan is useful to identify hypoxia and the associated radioresistance. This may facilitate hypoxia PET imaging compared to the acquisition and analysis of fully dynamic data.

If it should prove unfeasible to obtain all information about the hypoxia status of a tumour that is necessary for an effective adaption of RT, a combination of different imaging modalities may be an alternative. This may for example be a combination of FMISO PET and functional MRI methods, such as dynamic contrast enhanced (DCE) [88] or blood oxygen level dependent (BOLD) measurements [36, 45]. This approach is facilitated by modern PET/MRI equipment, which combines these two modalities in a single device, enabling simultaneous whole-body image acquisition without moving the patient off the bed between scans.

4.2. Acute hypoxia in FMISO PET imaging

4.2.1. Outline

Hypoxia can be classified into chronic and acute hypoxia. While chronic hypoxia is a static phenomenon, which is primarily caused by a sparse and chaotic network of vessels [8,80], acute hypoxia is highly dynamic and is characterised by fluctuating tissue PO_2 [27,33,89].

Fluctuating tissue PO_2 was directly measured in pre-clinical tumour models with polarographic and optical oxygen sensing methods [33,90]. Indirect methods, evaluating a mismatch between sequentially administered markers, also yielded evidence for acute hypoxia [32,91].

Although a varying oxygen consumption by tumour cells may cause fluctuations in tissue oxygenation, previous research was focussed on the relationship between fluctuations and variations in the red blood cell flux (RCF). Early studies attributed acute hypoxia to a total stasis of blood flow in tumour vessels [34]. This perception shifted towards a more gradual understanding of acute hypoxia, as it was demonstrated that varying RCF predominates over flow stasis in pre-clinical tumour models [92,93]. Fluctuating RCF was found in different human tumours as well [94]. A few studies combined direct single-point measurements of tissue PO_2 timelines and RCF in tumour models [89,95]. These studies revealed that frequently there is a correlation between flux fluctuations and variations in tissue oxygenation. Consequently, it seems justified to assume that the supply of oxygen, rather than the demand for it, is driving fluctuations in tissue.

Previously, theoretical simulations of tissue oxygenations were used to link supply fluctuations and acute hypoxia [89]. In a similar way, a theoretical model of intravascular PO_2 fluctuations was used to simulate the efficacy of the hypoxic cytotoxin tirapazamine under acute hypoxia [31]. It is an important prerequisite for a clinical application that FMISO PET imaging is reproducible. This has been questioned by an FMISO PET imaging study, because variations in the spatial uptake was found between repeated scans in head and neck cancer patients [28]. In contrast, a comparable study concluded that FMISO PET scans are highly reproducible [29]. In this context a method was developed to separate acute from chronic hypoxia using multiple independent scans [96]. So far, this method could not be validated [97].

In this part of the work, a theoretical model of varying intravascular PO_2 has been developed and integrated in the simulation method. The model and its parameter values were deduced from published measurements in pre-clinical tumour models. As results, the simulated oxygenations in different phases of the fluctuating oxygen supply are discussed. Moreover, the magnitude of the influence

of supply fluctuation on FMISO PET imaging is estimated. The results are interpreted in the context of the reproducibility of FMISO PET imaging and the potential separate assessment of the degrees of chronic and acute hypoxia.

4.2.2. Methods and Materials

Model of supply fluctuations

So far, the PO_2 in red blood cells P_{RBC} was set to a constant value. To simulate the influence of acute hypoxia on FMISO retention, the calculation of static oxygen distributions was extended by an explicit time dependence $P_{\text{RBC}} = P_{\text{RBC}}(t)$. As a consequence, the simulated oxygen supply became time dependent as well. Sinusoidal fluctuations around a mean value \bar{P} , with an amplitude P_A , a period T and a phase ϕ were assumed

$$P_{\text{RBC}}(t) = \bar{P} + P_A \sin\left(\frac{2\pi}{T}t + \phi\right). \quad (4.1)$$

This is a simplification of a broad range of fluctuation patterns observed in pre-clinical tumour models. Nonetheless, a number of published timelines clearly exhibit an approximately harmonic behaviour [90, 93]. The continuous fluctuations in Equation (4.1) were discretised, in order to maintain the approach of simulating the oxygenation and FMISO dynamics in consecutive steps (cf. Figure 3.1). In each timestep i of length Δt a constant P_{RBC}^i , i.e. a constant supply, was simulated as calculated from

$$P_{\text{RBC}}^i = \frac{1}{\Delta t} \int_{(i-1)\Delta t}^{i\Delta t} P_{\text{RBC}}(t) dt \quad (4.2)$$

for $i = 1, 2, \dots, T/\Delta t$. Figure 4.5b illustrates that the discretised values adequately sample the continuous fluctuations for $\Delta t = 2.5$ min, $T = 40$ min and hence $i = 1, 2, \dots, 16$, as chosen in this study. The choice of parameter values is discussed in the following section. In a separate scenario, total supply collapse in a manually selected group of vessels was added to continuous fluctuations. It was further assumed that the vital status of cells is not influenced by acute hypoxia.

In tissue, the small O_2 molecules have a higher mobility than FMISO because of their diffusive properties. This situation is reversed for intravascular transport, where most oxygen is bound in RBCs, which are large compared to FMISO molecules. Thus, fluctuating vascular oxygen supply does not necessarily imply an unstable supply of FMISO. This also holds true for transient collapse of RCF in vessels, as FMISO may still be transported by plasma flow [25]. Consequently, a stable tracer supply was assumed in this study.

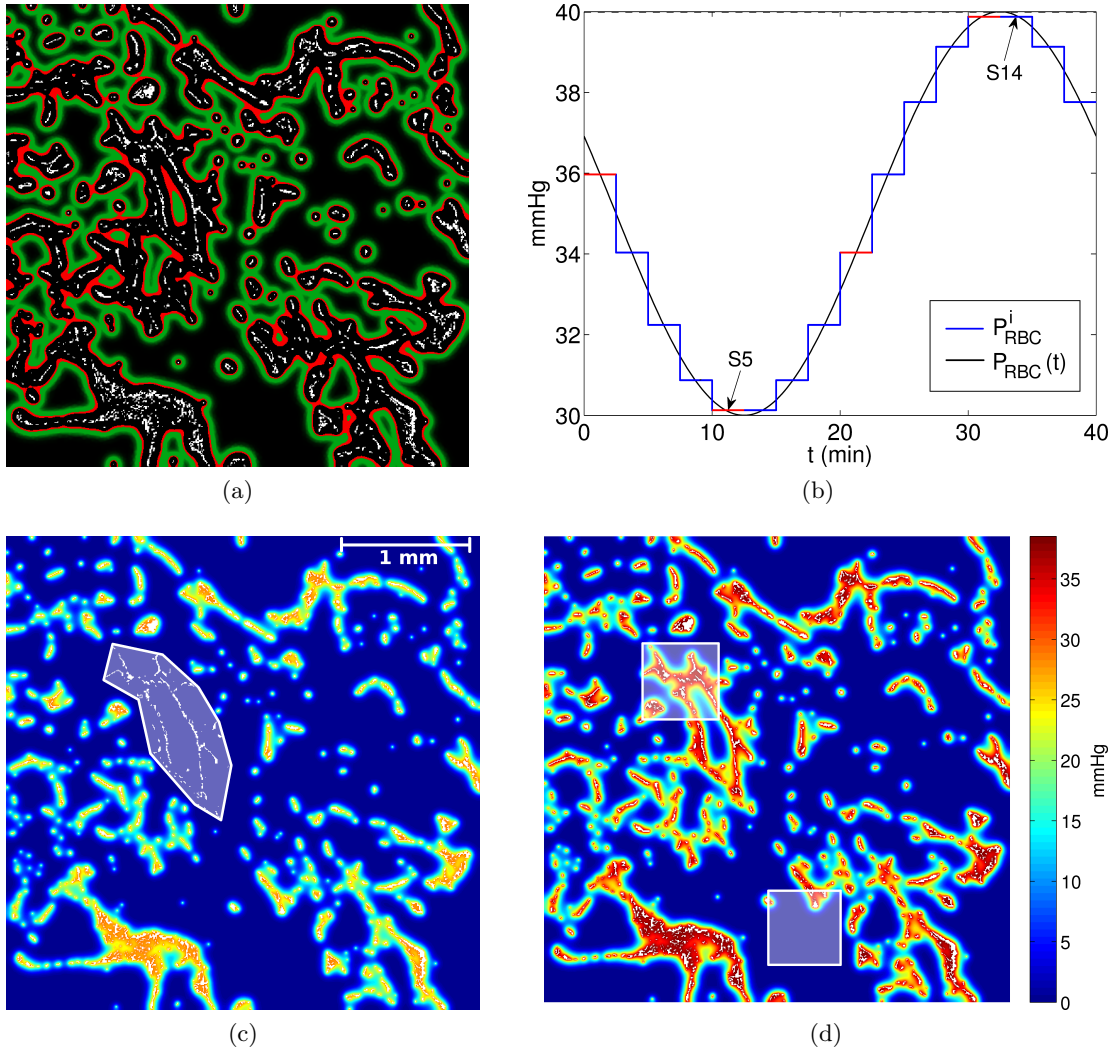


Figure 4.5.: (a) The simulated PO_2 fluctuates around 5 $mmHg$ in acutely hypoxic regions (red), which is a typical hypoxia threshold. It invariably remains below this threshold in chronically hypoxic regions (green). (b) Black curve: Modelled fluctuations of $P_{RBC}(t)$ for $T = 40$ min and $\bar{P} = 5$ $mmHg$, cf. Equation (4.1). Blue curve: Fluctuations discretised into steps of constant supply $P_{RBC}^i, i = 1, 2, \dots, 16$, cf. Equation (4.2). Red steps include total supply collapse. (c) Static oxygenation P_{eq} during step 5, i.e. low supply and supply collapse in outlined region. (d) Oxygenation during step 14, i.e. high supply and no supply collapse.

Parameter values

The choice of parameter values for the fluctuation model is based on pre-clinical timelines of intravascular PO_2 measured in rats [93]. Dominating fluctuation periods were on the order of tens of minutes. Total amplitudes as high as 10 mmHg were commonly observed, thus $P_A = 5$ mmHg was chosen for the simulations. These values may vary among different tumour entities, sites and volumes. Consequently, several fluctuation periods T were included in this study up to an empirically unvalidated value of $T = 4$ h, in order to assess the magnitude of the potential influence of acute hypoxia on hypoxia PET imaging. It appears likely that these effects crucially depend on the fluctuation period, because the accumulation of FMISO during the uptake period effectively integrates the concurrent fluctuations of the tracer binding rates. For P_{RBC} a mean value of $\bar{P} = 35$ mmHg was used, hence the maximum value of $P_A + \bar{P} = 40$ mmHg during cycling corresponds to the baseline chronic oxygenation. Experimentally observed fluctuations were not strictly synchronous among vessels in 6 mm^2 regions. Nonetheless, there is evidence for synchronous cycling in small groups of vessels as well [33]. Consequently, synchronous variations were modelled in the $4.2 \times 4.2 \text{ mm}^2$ vessel map that was used in this study. Again, this aimed to simulate the maximum effect. In some tumour models, a transient flow collapse or the absence of RCF was observed, affecting 5%–17% of repeatedly the same vessels for short periods [33, 98]. However, no data have yet been published on typical frequencies of this collapse. For simulation purposes a region comprising 13% of the total vessel volume in the vessel map was selected manually, which is depicted in Figure 4.5c. In the affected vessels, collapse was simulated with a duration of 2.5 min and a frequency of $f = 1/T = 6 \text{ h}^{-1}$.

4.2.3. Results

Influence on tissue oxygenation

Simulated static oxygen distributions in two fluctuation steps are shown in Figures 4.5c–d. In step 5 the oxygen supply is low ($P_{\text{RBC}}^5 = 30.1$ mmHg) and supply collapse is occurring in the selected group of vessels. On the other hand, step 14 is a high supply step ($P_{\text{RBC}}^{14} = 39.9$ mmHg) without collapse. The resulting PO_2 values averaged over the whole vessel map ($\bar{\text{PO}}_2$) for each fluctuation step are summarised in Figure 4.6a. In step 5 $\bar{\text{PO}}_2$ is 5.5 mmHg and 4.8 mmHg without and with supply collapse, respectively. In step 14 it is 8.2 mmHg, which is the approximate value for stable chronic hypoxia. Therefore, the maximum difference in $\bar{\text{PO}}_2$ is 3.4 mmHg or 41% relative to baseline conditions. Obviously, the tissue oxygenation is substantially influenced by the modelled supply fluctuations.

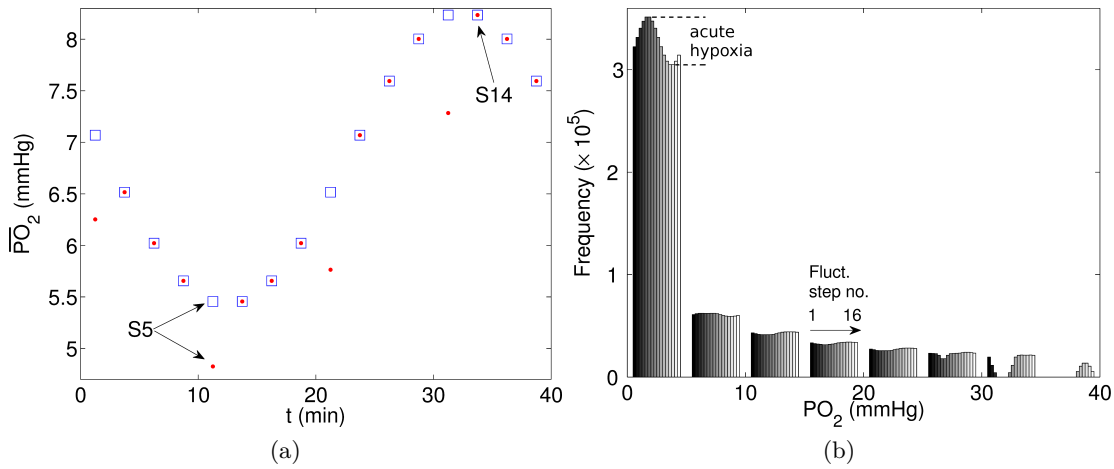


Figure 4.6.: (a) Mean PO_2 in the simulation map for each fluctuation step (cf. fig. 4.5c). Boxes: without supply collapse. Dots: with collapse occurring in every fourth step ($f = 6 \text{ h}^{-1}$). (b) PO_2 histogram for fluctuation steps 1 to 16 (black to white). The number of oxygen levels between 0 mmHg and 5 mmHg as well as between 30 mmHg and 40 mmHg are primarily affected by fluctuating supply. Supply collapse is not included in the histogram.

To analyse which oxygen levels are affected the most, PO_2 histograms for all fluctuation steps were plotted in Figure 4.6b. For a decreasing supply between steps 1 to 5, the number of high PO_2 values between 30 mmHg and 40 mmHg decreases, while the number of very low readings between 0 mmHg and 5 mmHg increases. This process is reversed when supply increases again during steps 6 to 13. In contrast, the number of intermediately oxygenated states between 5 mmHg and 30 mmHg is influenced much less.

Commonly, a hypoxic fraction (HF) is calculated by defining a threshold PO_2 value below which cells are considered hypoxic. Here, a value of 5 mmHg was chosen, which is a well established threshold. Though this binary picture of hypoxia is highly questionable, it offers a straightforward possibility to compare different oxygenations based on a single value. The acutely hypoxic fraction (aHF) can be defined as the proportion of tissue in which oxygen levels fluctuate across the threshold. The chronically hypoxic fraction (cHF) of tissue invariably remains below the threshold. For the presented example, this distinction is visualised in Figure 4.5a. The aHF is 8.6% and 12.2% for simulations without and with supply collapse, respectively. Chronic hypoxia prevails, with a cHF of 56.3%.

Influence on FMISO retention

In order to evaluate the influence of acute hypoxia on FMISO retention, TACs for the whole vessel map were simulated in four scenarios:

- (A) chronic hypoxia with a stable P_{RBC} of 40 mmHg,
- (B) fluctuating supply with $T = 40$ min, without supply collapse,
- (C) similar to B, but with supply collapse,
- (D) fluctuating supply with $T = 4$ h, without supply collapse.

Scenario D is exploratory, as there is no experimental evidence for such extremely slow cycling.

The amount of free tracer in tissue, which is available for binding, varies with time. Thus, the FMISO retention will depend on the phase of the fluctuating oxygen supply in which the tracer bolus is injected. More specifically, the shape of the simulated TAC for a particular scenario is different for different fluctuation phase parameters ϕ (cf. Equation (4.1)). If this effect is large enough to be detected in routine clinical PET acquisition, the reproducibility of FMISO PET imaging can be affected. To investigate whether this is realistic, simulations were performed with eight phases $\phi = 0, \pi/4, \dots, 7\pi/4$ covering a full fluctuation period in scenarios B and C as well as with $\phi = 0, \pi/2$ in scenario D. This aimed to simulate a test/retest experiment in a clinical setting.

The resulting TACs are shown in Figure 4.7a. Clearly, an unstable oxygen supply influences the total signal. Depending on the timepoint, 4.1% (2 h), 5.4% (3 h) and 6.2% (4 h) of the signal directly results from acute hypoxia in scenario C. The difference between scenarios B and C, i.e. the blue and the red curve, shows that, compared to baseline conditions, fluctuations without supply collapse cause more additional tracer retention than the additional phases of supply collapse. An isolated analysis of the bound FMISO component revealed that in scenario C a maximum of 13.0% of the retention is related to acute hypoxia (Figure 4.7b). This value includes 3.5% of the retention arising from supply collapse. These values are independent of the timepoint.

Regarding the reproducibility of the total signal, the maximum differences were evaluated within each set of curves in scenarios B, C and D. This yields an estimate for the test/retest variability that acute hypoxia might induce in a voxel-based FMISO PET signal. In scenarios B and C the variability between the curves was extremely small. For both cases the maximum difference was 0.7% at 140 min pi, while it was 0.3% at 4 h pi. In the exploratory scenario D, a variability of 3.8%

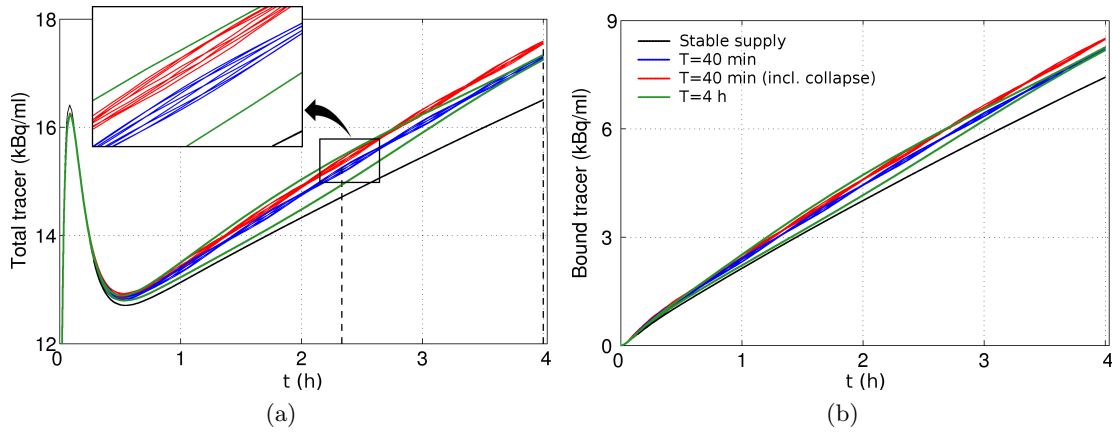


Figure 4.7.: (a) TACs for scenario A (black curve), B (blue), C (red) and D (green). For B and C, curves were simulated with fluctuation phases $\phi = 0, \pi/4, \dots, 7\pi/4$, for D with $\phi = 0, \pi/2$. (b) Isolated bound FMISO component.

(120 min pi) was found. These values are specified relative to the average of each set of curves at the respective timepoint.

So far, the analysis was performed for a single vessel map only. In order to further explore the potential magnitude of the effect, sub-regions with distinct vessel patterns were selected in the total map as depicted in Figure 4.5c. In the sub-region with an extremely low vessel density, the variability within the set of curves was 0.3% for scenario C, thus lower than in the total map. On the other hand, in a high vessel density sub-region the signal variability was 2.2%, which is an increase compared to the total map. Almost all vessels in the latter sub-region are affected by supply collapse, which explains the larger effect. Typically, tissue regions with an intermediate vessel density are affected most by fluctuating supply, because the net tracer accumulation is comparatively high. Consequently, the maximum expected signal variability is close to the 3.8% simulated for the total map in scenario D.

4.2.4. Discussion

In this study, periodical fluctuations in oxygen supply were modelled and integrated in the simulation method. The resulting variations in simulated tissue oxygenations showed that these fluctuations may induce acute hypoxia in substantial volumes of human tumours. Acutely hypoxic volumes are typically located

closer to vessels than the chronically hypoxic sub-population of cells. For the specific vessel map used in this study, chronic hypoxia prevails over acute hypoxia. This agrees with results from the evaluation of the frequency of acute and chronic hypoxia in immunohistochemically stained HNSCC xenograft sections [98].

However, regarding the influence of acute effects on FMISO PET imaging, the limited precision of PET measurements is important. Typically, in clinical PET imaging, acquisition times are adjusted to provide a voxel-based signal with a relative standard deviation of about 10%. A higher precision requires either the administration of a higher dose of radiolabelled tracer or a longer acquisition time, thus increasing the radiation exposure of the patient or the risk of image artifacts due to patient motion, respectively. With an accuracy of 10%, an increase of 6.2% in the total signal due to acute hypoxia is indistinguishable from the baseline signal without fluctuations. This is the maximum increase in uptake due to acute hypoxia simulated in this study. In other words, the results imply that two FMISO PET images acquired in the same subject, one in the presence of acute hypoxia and the other for stable supply, appear identical in a voxel-based analysis.

Regarding the issue of reproducibility the conclusion is similar. As the maximum simulated test/retest difference is 3.8% in scenario D, the consequence is that there is no detectable influence of acute hypoxia on FMISO PET imaging. This result appears reliable, because the fluctuation model was designed to evaluate the magnitude of the influence of acute hypoxia. Under most circumstances the influence of acute hypoxia on FMISO PET imaging presumably is even smaller, as fluctuation amplitudes and periods are smaller or fluctuations are less synchronised among vessels than assumed here.

Therefore, it seems unlikely that the differences between clinical repeat FMISO PET scans in HNSCC patients reported by Nehmeh *et al.* can be explained by acute hypoxia [28]. This is corroborated by a recent study performed under comparable conditions by Okamoto *et al.*, which lead to the conclusion that FMISO PET scans are highly reproducible [29]. Alternative explanations for the differences between repeated FMISO PET scans are an insufficient accuracy of the registration between the two PET/CT image volumes. It is also possible that irreversible, and therefore chronic, changes in the hypoxic status occurred between the scans. This is possible, as HNSCCs often progress rapidly [99]. However, this influence has not been observed by Okamoto *et al.*

The results have a number of implications for the integration of FMISO PET in RT treatment planning. Signals appear to be dominated by uptake from chronic hypoxia. The reproducibility of imaging an untreated tumour seems unaffected by acute hypoxia. These are ideal preconditions, if chronic hypoxia is the dominant form of hypoxia in terms of the negative impact on the efficacy of RT. FMISO

PET may then be used to predict treatment outcome and subsequently to locally adapt radiation doses according to the hypoxic status.

Though, it is also possible that the detrimental biological and clinical consequences of acute hypoxia dominate over those of chronic hypoxia. It has been suggested that acute hypoxia may induce increased radioresistance and stimulate transfer of cells to a more malignant phenotype, while chronically hypoxic cells are less harmful due to their limited survival time [26, 30]. In this situation the incapacity of FMISO PET imaging to detect acute hypoxia, which the presented results indicate, is problematic. Some capability to detect acute hypoxia might arise from an inherent correlation between chronic and acute hypoxia. Nevertheless, this correlation is speculative.

4.3. Correlation between tumour oxygenation and FMISO PET data

4.3.1. Outline

The tissue PO_2 in head and neck cancer patients measured with polarographic oxygen probes has been correlated with the overall survival after RT. Specifically, the fraction of measurements below 2.5 mmHg ($\text{HF}_{2.5}$) was the statistically most significant factor [11]. This study was based on data from 397 patients. There also is clinical evidence for the ability of FMISO PET imaging to predict RT outcome, though the studies performed until this point were based on much smaller numbers of patients [13].

So far, it is unclear which FMISO PET imaging protocol delivers the best surrogate for tissue PO_2 and therefore potentially has prognostic capabilities, comparable to those demonstrated for oxygen sensing probes. This issue has been addressed by a number of experimental studies investigating the relationship between PO_2 measurements with oxygen probes and hypoxia PET in clinical [100–102] as well as pre-clinical settings [103–105]. Generally, low or moderate correlations between hypoxia PET and direct probe measurements were observed. A good agreement was found in some tumours or tumour regions, while in others ambiguities remained.

A major drawback of the methods used in the aforementioned studies is the lack of a precise volumetric registration between PET and probe data, which is necessary for a voxel-based analysis. Recently, a voxel-based comparison was reported as well [106]. These problems in experimentally establishing links between tissue oxygenation and FMISO PET data make a simulation approach appealing. The method developed in this work overcomes many experimental limitations, because the simulated oxygenations and FMISO dynamics are based on the same microvessel maps and thus are perfectly aligned. It is furthermore possible to evaluate the full information from tracer dynamics, such as the wash-in and uptake phases, with very high spatial and temporal resolution.

The spatial distribution of hypoxia in tumour tissue is very heterogeneous on the microscopic length scale and often interspersed with necrotic regions. Necrosis frequently results from extremely low PO_2 levels. As FMISO is not retained in necrotic tissue, this may lead to low tracer retention in poorly oxygenated regions. This ambiguity, in combination with the PVE arising from the low spatial PET resolution, makes it virtually impossible to establish a bijective relationship between FMISO PET signals and properties of the underlying oxygenation. Nonetheless, it might be possible to derive a parameter from FMISO PET data that is sufficiently sensitive and specific for clinical purposes.

In this regard, two parameters were evaluated in this study, which can be readily acquired in a clinical setting: (a) The voxel values from a static FMISO PET scan 4 hpi (late scan). (b) The late scan signals were normalised with respect to a scan covering the first 15 min pi. The second parameter was chosen based on the result of Section 4.1 that the shape of the wash-in peak is characteristic for the density and arrangement of vessel in a voxel, i.e. its perfusion. In this way, predominantly necrotic voxels may be properly identified as high risk voxels, as they display a low perfusion in combination with a low tracer retention. Moreover, it has been suggested that a perfusion metric may contribute essential information about the potential of tissue to reoxygenate during RT [59]. In this case, it must be included in a metric predicting the radiosensitivity based on FMISO PET data. In this study, the correlations were analysed between the FMISO parameters specified above and characteristic properties of the underlying oxygenation, i.e. the mean PO_2 and the vital hypoxic fraction. The parameters are defined in detail in the following section.

4.3.2. Methods and Materials

Five tissue sections from different pre-clinical tumours with a combined area of 133 mm^2 were converted into binary vessel maps using the method described in Section 3.2.2. The sections covered a large range of distinct vessel distributions. Subsequently, a total number of 300 sub-regions with dimensions of $2 \times 2 \text{ mm}^2$ were placed in the vessel maps at random locations. In these sub-regions, O_2 and FMISO parameters were calculated from the simulated data as specified in the following section.

Oxygenation and FMISO parameter sets

Two parameters were evaluated from the simulated FMISO distributions. First, a measure of tracer retention F_H was derived from averaging the concentration $C(x, y, t)$ for $t = 4 \text{ hpi}$ over each sub-region:

$$F_H = \frac{1}{A_\Omega} \int_{\Omega} C(x, y, t = 4 \text{ h}) dx dy + C_{iv}(t = 4 \text{ h}) VF \quad (4.3)$$

where Ω denotes the extravascular space, A_Ω the area of Ω and VF the respective vascular fraction. To obtain a measure of perfusion, the simulated early timeframes between 0 and τ were averaged:

$$F_P = \frac{1}{\tau} \int_0^\tau \left(\frac{1}{A_\Omega} \int_{\Omega} C(x, y, t) dx dy + C_{iv}(t) VF \right) dt. \quad (4.4)$$

Based on this, the second investigated FMISO-derived parameter was evaluated from

$$F_{H/P} = \frac{F_H}{F_P}. \quad (4.5)$$

Here, $\tau = 15$ min was chosen, as this covers substantial parts of the wash-in phase and could be clinically implemented. The simulated steady-state oxygenations were characterised by two parameters. The mean of the equilibrium oxygen distribution $P_{eq}(x, y)$ in the respective sub-region was calculated from

$$\overline{PO_2} = \frac{1}{A_\Omega} \int_\Omega P_{eq}(x, y) dx dy.$$

In experimental studies, the hypoxic fraction (HF) is frequently evaluated as the ratio between the number of PO_2 measurements below and above a threshold value P_{crit} . Typical threshold values are 2.5 mmHg and 5 mmHg. Vital and necrotic tissue regions are likewise included in HF and in $\overline{PO_2}$ and both parameters are highly correlated, especially for hypoxic sub-regions, as can be seen in Figure 4.9b. For this reason a vital hypoxic fraction (vHF) was introduced in this study, instead of evaluating the HF. It regards the vital fraction F_2 at a particular location according to Equation (3.10) and therefore includes vital regions only. It was calculated from

$$vHF = \frac{1}{A_\Omega} \int_\Omega V(P_{eq}(x, y)) dx dy$$

$$V(P) = \begin{cases} F_2(P) & \text{if } P < P_{crit} \\ 0 & \text{else.} \end{cases}$$

In this study, $P_{crit} = 2.5$ mmHg was chosen.

Receiver operating characteristic

A straightforward approach to analyse FMISO PET signals is to choose a cut off value above which the respective parameter presumably indicates hypoxia. A too small cut off value leads to a low specificity, i.e. a high rate of false-positive results (FPR). A too large value leads to a low sensitivity, i.e. a low rate of true-positive results (TPR). The optimum value is located somewhere in between. The diagnostic accuracy for a given threshold value can be quantified by the Youden Index (YI) defined as

$$YI = TPR - FPR$$

$$= \text{Sensitivity} + \text{Specificity} - 1.$$

A receiver operating characteristic (ROC) analysis can be performed by plotting the TPR against the FPR for various cut off values. The area under the ROC curve (AUC) is an alternative accuracy measure. In contrast to the YI, the AUC regards the whole ROC curve and therefore also includes information about the stability of the method. The AUC and YI values may range from 0.5 to 1 and 0 to 1 (futile to ideal), respectively.

In this study a ROC analysis was performed, to investigate how accurately the two FMISO-derived parameters identify voxels with $\overline{PO}_2 < P_{\text{crit}}$. In a further step, the ROC analysis was also used to evaluate how well the parameters characterise the PO_2 on the microscopic length scale (micro PO_2). In this case, a single FMISO parameter does not represent a single \overline{PO}_2 value, but a matrix of 60×60 underlying microscopic oxygen partial pressures.

4.3.3. Results

Simulated oxygenations

Full simulations were performed on all vessel maps. An example of a simulated equilibrium PO_2 distribution is given in Figure 4.8a. Moreover, Figures 4.8b–c show the corresponding FMISO pattern 4 h pi as well as the pattern averaged over the first 15 min pi, respectively.

The median PO_2 over all maps was 10.0 mmHg (0.0 mmHg–40.0 mmHg), calculated with a resolution of 50 $\mu\text{m}/\text{pixel}$, i.e. a resolution comparable to that of polarographic probes. This agrees with observations in clinical HNSCC, where the median PO_2 assessed by different institutions ranged from 5 mmHg to 18 mmHg with an overall median of 9 mmHg [11]. This does not prove that the simulations adequately reproduce the manifold oxygenations in HNSCC. For example, there appears to be a disagreement with regard to the HF. The median simulated HF of 37% is considerably higher than the experimental value of 19%. This might partly be explained by the low accuracy of polarographic oxygen probes, which is about 1 mmHg irrespective of the absolute value [79]. Nonetheless, histograms of the microscopic PO_2 within four selected sub-regions exhibit distinct oxygenation patterns, as shown in Figure 4.9a. This indicates that the irregularities in tumour oxygenations are, to some degree, reproduced by the simulations.

The simulated sub-regional \overline{PO}_2 ranged from 1.3 mmHg to 32.5 mmHg with a median of 11.0 mmHg. The median vHF was 26% (0%–48%), while the median HF was 34% (0%–87%). In Figure 4.9b the simulated vHF and HF are plotted against \overline{PO}_2 . For mean PO_2 values above 17 mmHg vHF and HF overlap, which indicates that cell necrosis plays a minor role in this PO_2 range. However, for lower values vHF and HF differ greatly. In hypoxic regions with $\overline{PO}_2 < 10$ mmHg the

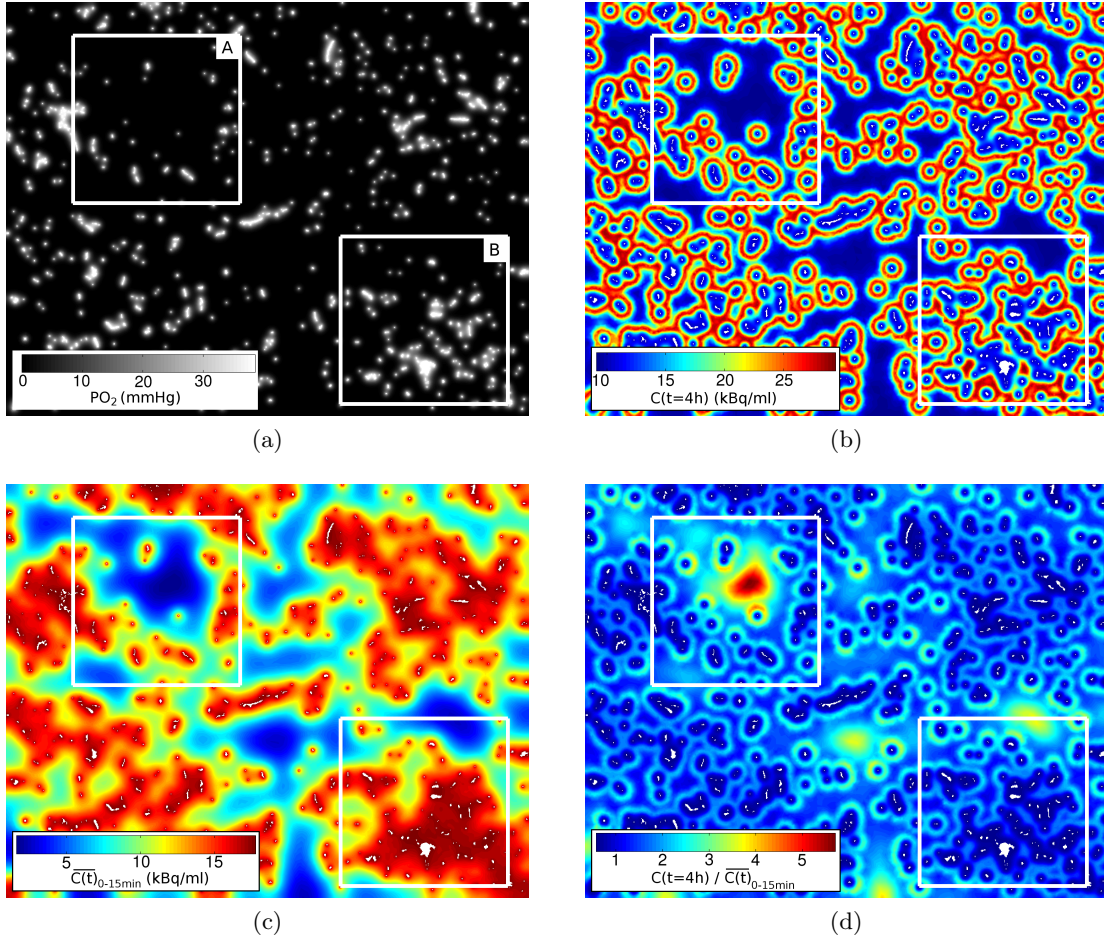


Figure 4.8.: (a) Equilibrium PO_2 distribution for a $6.3 \times 4.9 \text{ mm}^2$ vessel map, including two randomly placed $2 \times 2 \text{ mm}^2$ sub-regions (A and B). (b) Corresponding FMISO distribution 4 h pi, from which F_H is calculated according to Equation (4.3). (c) FMISO distribution averaged over timeframes between 0 min and 15 min, from which F_P is calculated according to Equation (4.4). (d) Ratio between the distributions in (b) and (c). Averaging over sub-regions yields $F_{H/P}$, as defined in Equation (4.5).

relationship between vHF and mean $\overline{PO_2}$ appears ambiguous, while apparently the HF is linearly related to $\overline{PO_2}$. This was the reason for abandoning the HF in favour of the mean $\overline{PO_2}$ in the further analysis, as the latter does not include an arbitrary threshold value. Certainly, the biological basis for a fixed hypoxia threshold is questionable.

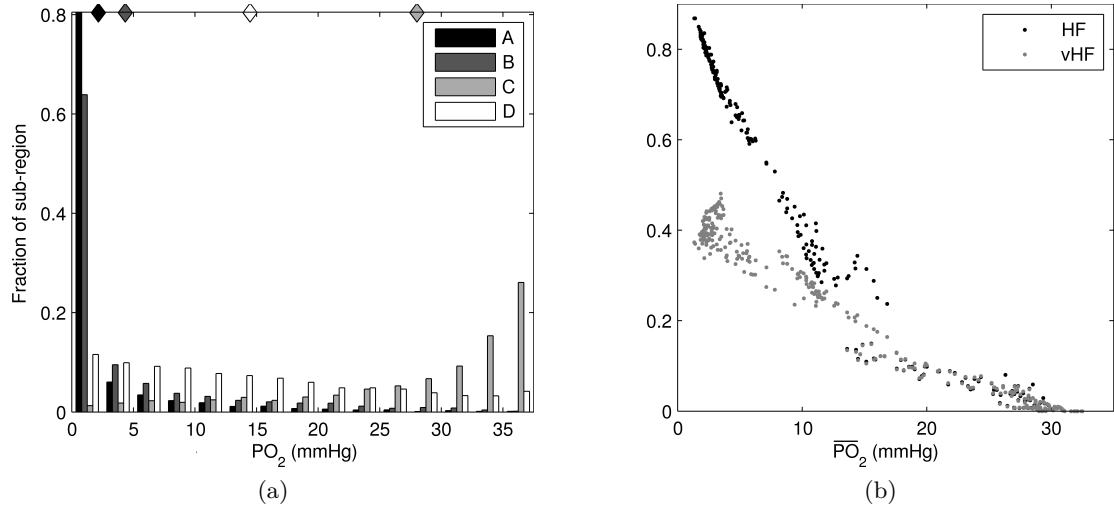


Figure 4.9.: (a) Histograms of the simulated micro PO_2 values in four different sub-regions display distinct distributions. Sub-regions A and B are depicted in Figure 4.8a, C and D are not shown. The mean of each histogram is indicated on the top axis. (b) Scatter plots of vHF and HF against $\overline{PO_2}$. Necrosis does not induce a difference between vHF and HF for $\overline{PO_2} > 17$ mmHg. For lower values, the exclusion of necrotic areas in the vHF causes large differences. In hypoxic areas ($\overline{PO_2} < 10$ mmHg) HF appears to be linearly correlated with $\overline{PO_2}$, while there are large discrepancies between $\overline{PO_2}$ and vHF.

Correlations between oxygenation and FMISO PET

Sub-regions A and B in Figure 4.8a are good examples of the ambiguous relationship between FMISO retention and mean PO_2 . The mean PO_2 in A and B is 1.7 mmHg and 4.3 mmHg, respectively. This is inconsistent with the late FMISO signal F_H , which is lower in A (16.2 kBq/ml) than in B (17.7 kBq/ml). In contrast, the combined parameter $F_{H/P}$ is consistent with the mean PO_2 , because it is higher in A (1.82) than in B (1.35).

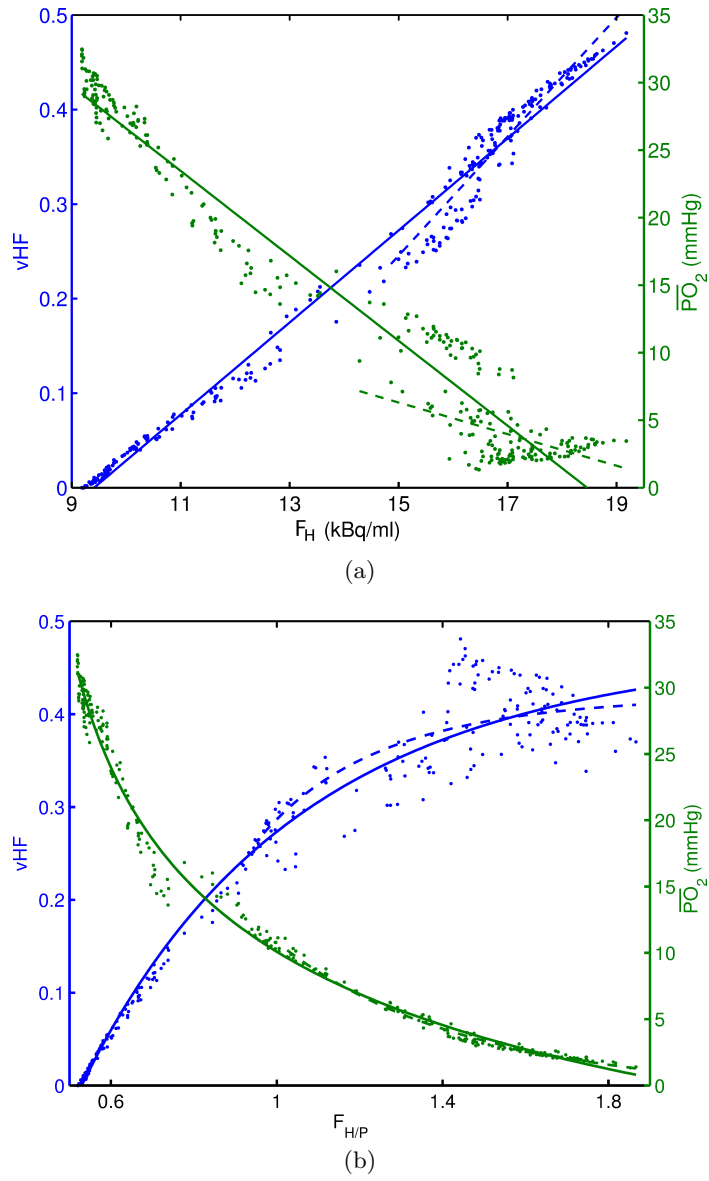


Figure 4.10.: Scatter plots of vHF and $\overline{PO_2}$ against the FMISO parameters (a) F_H and (b) $F_{H/P}$. Continuous lines are fits to the overall data, while dashed lines are fits restricted to hypoxic regions. The respective coefficients of determination R^2 for the restricted fits show that vHF correlates with F_H . In contrast, $\overline{PO_2}$ correlates with $F_{H/P}$ only (cf. Table 4.1).

In Figure 4.10a scatter plots of vHF and $\overline{\text{PO}}_2$ against F_{H} are shown. Each point represents a data pair from a specific sub-region. A high overall linear correlation coefficient R^2 of 0.99 and 0.95 for vHF and $\overline{\text{PO}}_2$ was observed, respectively. These values reduced to 0.90 and 0.22, respectively, when the analysis was restricted to data pairs in the hypoxic range, where $\overline{\text{PO}}_2 < 10$ mmHg and vHF > 0.24 . A high diagnostic accuracy is especially important in this range. Consequently, F_{H} is a reliable surrogate measure of the vHF, but it does not enable an accurate prediction of the $\overline{\text{PO}}_2$.

Figure 4.10b shows plots of vHF and $\overline{\text{PO}}_2$ against the second FMISO parameter $F_{\text{H/P}}$. Both scatter plots display a nonlinear relationship. Based on a visual inspection $\overline{\text{PO}}_2$ appears better defined than the vHF, especially in the hypoxic range. This was corroborated by fitting a function of the form

$$f(F_{\text{H/P}}) = \frac{p_1}{(p_2 + F_{\text{H/P}})^{p_3}} + p_4 \quad (4.6)$$

to both data sets in a least-squares sense. The respective fit coefficients $p_i, i = 1, 2, \dots, 4$ and determination coefficients R^2 are summarised in Table 4.1. For fits to the overall data, vHF as well as $\overline{\text{PO}}_2$ appear highly correlated with $F_{\text{H/P}}$, with R^2 values of 0.97 and 0.99, respectively. When the fit is restricted to data in the hypoxic range, values of R^2 were 0.54 and 0.99, respectively. This suggests that in this range $F_{\text{H/P}}$ is a more accurate surrogate measure of the mean PO_2 than F_{H} .

Table 4.1.: Coefficients obtained by fitting Equation (4.6) to the vHF- $F_{\text{H/P}}$ and $\overline{\text{PO}}_2$ - $F_{\text{H/P}}$ data shown in Figure 4.10b. The respective coefficient of determination R^2 is specified as well. For $\overline{\text{PO}}_2$: $[p_1] = [p_4] = \text{mmHg}$.

| | p_1 | p_2 | p_3 | p_4 | R^2 |
|--|---------------------|------------------------|-----------------------|------------------------|-------|
| vHF (overall) | -9.61×10^4 | 3.85 | 8.27 | 4.79×10^{-1} | 0.97 |
| vHF (> 0.24) | -4.90×10^1 | 1.22 | 7.37 | 4.22×10^{-1} | 0.54 |
| $\overline{\text{PO}}_2$ (overall) | 3.99×10^1 | -3.71×10^{-1} | 2.66×10^{-1} | -3.51×10^1 | 0.99 |
| $\overline{\text{PO}}_2$ (< 2.5 mmHg) | 4.39×10^4 | 2.25 | 6.97 | -9.93×10^{-1} | 0.99 |

The ROC analysis of the diagnostic accuracy of the two FMISO parameters to identify hypoxia is visualised in Figure 4.11. Clearly, regions with a critical mean PO_2 can be discriminated extremely well using $F_{\text{H/P}}$ (AUC = 0.95, optimal YI = 0.94), while F_{H} alone is much less reliable (AUC = 0.88, YI = 0.68). Note that for very high thresholds applied to F_{H} the false positive rate is higher than

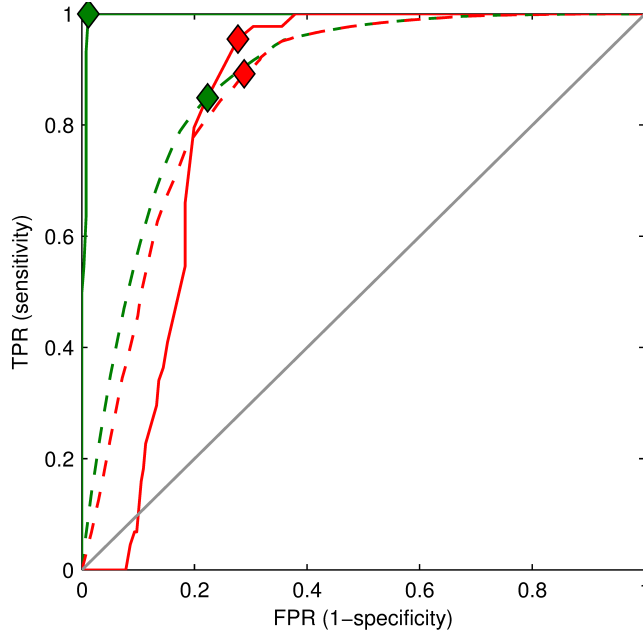


Figure 4.11.: Receiver operating characteristic of $F_{H/P}$ (green curves) and F_H (red curves) for the identification of hypoxia ($P_{\text{crit}} = 2.5$ mmHg) using different cut off values. Solid and dashed lines refer to the identification of \overline{PO}_2 and microPO_2 , respectively. Cut off values applied to the FMISO parameters decrease along the curves from left to right. Optimum points in terms of maximum YI are marked. The identification of critical \overline{PO}_2 is very sensitive and specific using $F_{H/P}$ (YI = 0.94). Using F_H is less effective (YI = 0.68). Both parameters are moderately accurate in identifying critical microPO_2 values (YI = 0.63 and 0.60).

the true positive rate. This means that the sub-regions with the highest tracer retention are identified as hypoxic, though the mean PO_2 lies above the critical value. The optimum threshold values, in terms of maximum YI, were $F_{H/P} = 1.61$ and $F_H = 16.3$ kBq/ml. The latter threshold value is equivalent to a T/B ratio of 1.8. The ROC analysis of the accuracy of identifying hypoxia that was defined based on microPO_2 with the FMISO parameters resulted in AUC values (optimum YI) of 0.88 (0.63) and 0.86 (0.60) for $F_{H/P}$ and F_H , respectively. These values are almost identical to those for identifying macroscopic hypoxia (according to \overline{PO}_2) using F_H , though much lower compared to $F_{H/P}$. Here, the optimum thresholds were $F_{H/P} = 1.0$ and $F_H = 15.5$ kBq/ml. The latter is equivalent to a T/B ratio of 1.7. Note the considerable decrease in the optimum $F_{H/P}$ threshold compared

to the identification of $\overline{PO_2}$. A decreasing threshold implies an increased fraction of sub-regions that are identified as hypoxic. In this case it increased from 15.7% to 46.6%. This can be interpreted in the context of RT dose painting: if the tumour sub-volume that receives an escalated radiation dose increases three-fold, this might strongly affect normal tissue complication probabilities.

4.3.4. Discussion

The results of this study outline the fundamental problems associated with imaging microscopic tumour hypoxia using PET, which is a macroscopic imaging modality. In addition to the PVE, the ambiguous binding behaviour of FMISO is problematic, i.e. it is not accumulated in well oxygenated as well as predominantly necrotic tissue. Necrosis is closely related to the progress of hypoxia [107].

The finding that late FMISO PET signals (F_H) are poor surrogate measures for the mean PO_2 in a voxel is a direct consequence of these limitations. On the other hand, it appears that the vHF, a parameter already corrected for necrosis by its definition, can be identified based on late signals with high accuracy. As our results show a high accuracy of assessing the mean PO_2 by means of $F_{H/P}$, supplementing the late FMISO information with information from the wash-in phase obviously compensates the loss of retention due to necrosis and also the excessive binding in voxels dominated by intermediate hypoxia.

This work can not answer the question whether vHF or $\overline{PO_2}$ offers a better prediction of the response to RT. However, all previous reports of a correlation between direct measurements of tumour oxygenation and RT efficacy were uncorrected for necrosis, i.e. it was not distinguished between necrotic and vital tissue. Therefore, there is only evidence for the predictive value of $\overline{PO_2}$, which was the reason for limiting the ROC analysis to this parameter.

The acquisition of both evaluated FMISO parameters requires relatively simple clinical PET imaging protocols. F_H is comparable to the voxel values in a static scan several hours pi, as it typically has been acquired in previous studies. For the evaluation of $F_{H/P}$ a second scan covering the wash-in phase would be necessary, followed by a registration of the PET/CT image volumes as well as a simple division between late and early voxel values.

There are some limitations regarding the transfer of the theoretical results of this study to clinical data and the underlying biological systems. Generally, the mathematical model is an idealisation of real tissue and the behaviour of O_2 and FMISO molecules therein. Adding further biological aspects to the model, e.g. a heterogeneous vascular permeability (MTC) for tracer molecules, would weaken the evaluated correlations. It probably has the same effect, if a larger base of histological material would be included that covers a broader range of vessel con-

figurations. Two other limitations specific to this study also lead to an overestimation of the diagnostic accuracy. First, the chosen size of sub-regions was smaller than a clinical PET voxel, because the size and number of available histological tissue sections was limited. Second, stable oxygenation properties (vHF , $\overline{PO_2}$) were assumed, though it was shown in Section 4.2 that the oxygenation is not static and that FMISO PET signals predominantly depict chronic hypoxia. The listed limitations likewise affect the correlations between $\overline{PO_2}$ and F_H as well as $F_{H/P}$. Therefore the conclusion that $F_{H/P}$ has a higher diagnostic accuracy than F_H remains unchanged.

In conclusion, this study offers an explanation for the low correlations that were reported between PO_2 and late FMISO PET measurements in clinical and pre-clinical tumours. Furthermore, the results indicate a potential advantage of using the independent information of two FMISO PET scans to accurately assess the mean PO_2 in a voxel-based manner in head and neck tumours, compared to a single scan. The first scan covers the tracer wash-in phase, while the second scan is acquired following a tracer uptake phase of several hours.

5. Summary and Outlook

Summary

This work investigates the assessment of hypoxia in human tumours with FMISO PET imaging. A special focus lies on its potential use in RT, as hypoxia is especially relevant regarding the prediction of the efficacy of RT [10, 11]. There is a number of open questions in FMISO PET imaging, particularly regarding the optimum acquisition modes. Scans can be performed in static or dynamic mode and at different timepoints post injection (pi). Most clinical FMISO PET imaging studies were based on small numbers of patients and imaging was rarely performed in dynamic mode [13]. Moreover, it has been suggested that scans must be acquired after the initiation of RT, in contrast to pre-treatment scans, to allow a prediction of treatment outcome [84].

As hypoxia is a microscopic phenomenon [7, 19], a fundamental understanding of FMISO PET requires an understanding of the processes on this length scale. In this work, a method is developed to simulate these processes. For this purpose, biophysical models of the diffusion and consumption of oxygen as well as the diffusion and retention of FMISO are combined. In contrast to an earlier model outlined in [24], it is considered that FMISO is retained in vital hypoxic cells only. Moreover, it is very important to include an accurate model of the supply of oxygen and the flux of FMISO into and out of tissue via capillary networks [108]. For this reason, 2D vessel maps are created based on tumour histology, which is a uniqueness of this work. Simulations are performed by solving the model-specific system of PDEs using the FEM in 2D. The method is validated by comparing the simulated results with IHC material and clinical FMISO PET data acquired in dynamic mode.

This work consists of three different studies that are performed using the described simulation method [109, 110]. See also Appendices A–C. In the following the results are briefly summarised. The first study shows that the diffusion of FMISO molecules to hypoxic regions is rather dilatory. As a result, the accumulation of FMISO may not be interpreted as hypoxia-specific for the first 30 min pi. It takes additional time, until a specific contrast develops. Therefore, it is obligatory to perform static FMISO PET imaging at timepoints later than 1 h pi. Possibly, even longer uptake times are necessary to achieve detectable and consis-

tent intratumour contrasts. A high image contrast is important for example for the automatic segmentation of hypoxic volumes using different algorithms [85]. In this study, it is as well demonstrated that the information content of a PET scan covering the wash-in of tracer is distinct from that of a scan during the accumulation phase a few hours pi. While tracer accumulation is related to hypoxia, the early signals appear to contain information about the density and regularity of the vessel network in a voxel. The denser and more regular the vessel network, the higher may be the probability that reoxygenation occurs during fractionated RT [58, 59, 111]. Therefore, the magnitude of early signals may be correlated with radiosensitivity.

In the second study, the role of acute, i.e. temporally varying, hypoxia in FMISO PET imaging is addressed. It is a frequently discussed issue whether the reproducibility of this imaging modality is impaired by acute hypoxia [28, 29] and whether it is possible to separately assess the degree of acute and chronic hypoxia based on two independent scans [96]. This is of interest, as acutely hypoxic cells may be less radiosensitive and less susceptible to radiosensitising drugs, compared to cells under chronic hypoxia [26, 93]. Therefore, a model of fluctuating oxygen levels in blood is integrated in the simulation model. These fluctuations result in temporal variations of the FMISO retention rates. The results of this study suggest that the influence of acute hypoxia on FMISO imaging is negligible, even though the fluctuation model is designed to explore the magnitude of the effect. FMISO PET thus predominantly images chronic hypoxia and the associated effects on RT. Consequently, the reported poor match between two independent image volumes that were acquired within three days in the same patients [28], most likely can not be explained by acute hypoxia. Possible explanations are an inconsistent patient preparation and positioning as well as an inaccurate post-scan registration of the two image volumes. Accordingly, a recent study performed under comparable conditions concluded that FMISO PET scans are highly reproducible [29].

In FMISO PET imaging, the microscopic oxygenation of tissue is assessed with a macroscopic imaging modality. The resulting spatial undersampling leads to errors in the assessment of different properties of the oxygen distribution in a PET voxel and consequently of hypoxia [20]. In the third study, this aspect is investigated in particular regard to the assessment of the mean PO_2 and the fraction of vital hypoxic cells (vHF) with FMISO PET. The accuracies of different surrogate measures of these parameters that can be derived from clinical FMISO PET imaging is studied with the simulation tool. A major result is that the mean PO_2 in a PET voxel may be assessed based on two static FMISO PET scans covering the wash-in and the accumulation phase, respectively. Compared

to a single scan, the accuracy of this method is much higher. The vHF may be effectively assessed by a single scan. However, it is reasonable to assume that the mean PO_2 is a better predictor of the radiation response than the vHF, as the oxygen enhancement of radiation damage shows a strong nonlinear dependence on the PO_2 [73]. Clinical data have to be analysed to investigate the feasibility of the proposed method. An advantage of the proposed method is that two static FMISO PET scans are easy to implement in clinical routine, in contrast to dynamic imaging, which is technically demanding and associated with a complex data analysis [55, 87].

Outlook

Some aspects of the simulation model have to be validated more comprehensively in the future. This can be achieved based on pre-clinical tissue sections, for which FMISO autoradiographs as well as images of the corresponding vessel structures are available. For these data sets, simulated FMISO distributions can be compared with experimental data. However, the analysis is restricted to a single timepoint, as autoradiographs display the tracer distribution at the moment when the laboratory animal has been sacrificed. In this way, for instance a better estimate may be found of the typical distance from vessels at which the maximum FMISO retention occurs. It critically depends on the PO_2 at which cell necrosis becomes important (cf. Equation (3.10)).

A further step will be to extend the method from 2D to 3D. It is possible to reconstruct 3D models of vessel networks from consecutive tissue sections, which were IHC stained for vessel structures [112]. With a fully 3D method, gradients in the intravascular oxygen content along elongated capillaries can be simulated. In case FMISO PET data has been obtained *in vivo* for the respective sections, it is as well possible to compare experimental and simulated PET data. Though, this requires an accurate spatial registration between IHC and the PET image, which can be realised in pre-clinical experiments [113]. For a quantitative comparison, it may also be necessary to consider blurring of FMISO signals by the point spread function (PSF) in the simulated data. The PSF is an intrinsic property of the PET scanner and the tracer radioisotope. Comparable PET data may also be obtained from simulated FMISO emission densities by Monte Carlo simulations of the detection process in the PET scanner [114]. This must be followed by image reconstruction with the same algorithm as the experimental data that is used for comparison.

Other hypoxia PET tracers have been developed, in addition to the first generation tracer FMISO, e.g. $[^{18}F]FAZA$ and $[^{60/64}Cu]ATSM$. These molecules differ

from FMISO in some aspects, such as the lipophilicity, the tissue clearance rate and the binding rate- PO_2 relationship. By adapting the simulation model to different tracers, their behaviour can be compared. For each tracer substantiated hypotheses regarding their respective general performance and optimum imaging protocols can be generated, instead of simply extrapolating experiences from FMISO PET imaging.

Another future line of research lies beyond the scope of the presented simulation model. It is the validation of a hypothesis, which is formulated in Section 4.3 based on results of this work. The hypothesis is that a parameter $F_{\text{H/P}}$, which combines early and late FMISO PET data, is a reliable predictor of the overall RT efficacy and moreover of the local hypoxia-associated radiosensitivity. The former aspect can be studied using existing clinical data sets of dynamic FMISO PET data and RT follow-up information. It is much more complex to investigate the second aspect, as detailed information about the localisation of potential tumour recurrences following RT are required. High recurrence rates are expected in regions with a high pre-treatment $F_{\text{H/P}}$ value.

Bibliography

- [1] Delaney G, Jacob S, Featherstone C, Barton M: **The role of radiotherapy in cancer treatment.** *Cancer* 2005, **104**(6):1129–1137.
- [2] Alber M, Thorwarth D, Ganswindt U, Belka C: **Fluenzmodulierte Strahlentherapie (IMRT).** In *Radioonkologie: Grundlagen, Volume 1*, 2nd edition, München: Zuckschwerdt 2009:189–201.
- [3] Debus J, Kraft G, Hug G: **Hadronentherapie.** In *Radioonkologie: Grundlagen, Volume 1*, 2nd edition, München: Zuckschwerdt 2009:95–108.
- [4] Budach V, Stuschke M, Budach W, Baumann M, Geismar D, Grabenbauer G, Lammert I, Jahnke K, Stueben G, Herrmann T, Bamberg M, Wust P, et al.: **Hyperfractionated Accelerated Chemoradiation With Concurrent Fluorouracil-Mitomycin Is More Effective Than Dose-Escalated Hyperfractionated Accelerated Radiation Therapy Alone in Locally Advanced Head and Neck Cancer: Final Results of the Radiotherapy Cooperative Clinical Trials Group of the German Cancer Society 95-06 Prospective Randomized Trial.** *J Clin Oncol* 2005, **23**(6):1125–1135.
- [5] Yaromina A, Thames H, Zhou X, Hering S, Eicheler W, Dörfler A, Leichtner T, Zips D, Baumann M: **Radiobiological hypoxia, histological parameters of tumour microenvironment and local tumour control after fractionated irradiation.** *Radiother Oncol* 2010, **96**:116–122.
- [6] Baumann M, Zips D, Molls M: **Die "4 Rs" der Strahlentherapie und Prädiktion der Strahlenreaktion von Tumoren.** In *Radioonkologie: Grundlagen, Volume 1*, 2nd edition, München: Zuckschwerdt 2009:268–279.
- [7] Ljungkvist AS, Bussink J, Rijken PF, Kaanders JH, van der Kogel AJ, Denekamp J: **Vascular architecture, hypoxia, and proliferation in first-generation xenografts of human head-and-neck squamous cell carcinomas.** *Int J Radiat Oncol Biol Phys* 2002, **54**:215–228.
- [8] Vaupel P: **Tumor microenvironmental physiology and its implication for radiation oncology.** *Semin Radiat Oncol* 2004, **14**(3):198–206.

- [9] Gray LH, Conger AD, Ebert M, Hornsey S, Scott OCA: **The Concentration of Oxygen Dissolved in Tissues at the Time of Irradiation as a Factor in Radiotherapy.** *Br J Radiol* 1953, **26**(312):638–648.
- [10] Höckel M, Schienger K, Aral B, Milze M, Schäffer U, Vaupel P: **Association between Tumor Hypoxia and Malignant Progression in Advanced Cancer of the Uterine Cervix.** *Cancer Res* 1996, **56**:4509–4515.
- [11] Nordsmark M, et al.: **Prognostic value of tumor oxygenation in 397 head and neck tumors after primary radiation therapy. An international multi-center study.** *Radiother Oncol* 2005, **77**:18–24.
- [12] Rajendran JG, Schwartz DL, O’Sullivan J, Peterson LM, Ng P, Scharnhorst J, Grierson JR, Krohn KA: **Tumor Hypoxia Imaging with [F-18] Fluoromisonidazole Positron Emission Tomography in Head and Neck Cancer.** *Clin Cancer Res* 2006, **12**(18):5435–5441.
- [13] Horsman MR, Mortensen LS, Petersen JB, Busk M, Overgaard J: **Imaging hypoxia to improve radiotherapy outcome.** *Nat Rev Clin Oncol* 2012, **9**:674–687.
- [14] Ling CC, Humm J, Larson S, Amols H, Fuks Z, Leibel S, Koutcher JA: **Towards multidimensional radiotherapy (MD-CRT): biological imaging and biological conformality.** *Int J Radiat Oncol Biol Phys* 2000, **47**(3):551–560.
- [15] Alber M, Paulsen F, Eschmann SM, Machulla HJ: **On biologically conformal boost dose optimization.** *Phys Med Biol* 2003, **48**(2):N31–N35.
- [16] Thorwarth D, Eschmann SM, Paulsen F, Alber M: **Hypoxia dose painting by numbers: A planning study.** *Int J Radiat Oncol Biol Phys* 2007, **68**:291–300.
- [17] Eschmann SM, Paulsen F, Reimold M, Dittmann H, Welz S, Reischl G, Machulla HJ, Bares R: **Prognostic Impact of Hypoxia Imaging with 18F-Misonidazole PET in Non-Small Cell Lung Cancer and Head and Neck Cancer Before Radiotherapy.** *J Nucl Med* 2005, **46**(2):253–260.
- [18] Thorwarth D, Eschmann SM, Scheiderbauer J, Paulsen F, Alber M: **Kinetic analysis of dynamic 18F-fluoromisonidazole PET correlates with radiation treatment outcome in head-and-neck cancer.** *BMC Cancer* 2005, **5**:152.

-
- [19] Troost EG, Laverman P, Kaanders JH, Philippens M, Lok J, Oyen WJ, van der Kogel AJ, Boerman OC, Bussink J: **Imaging hypoxia after oxygenation-modification: Comparing [18F]FMISO autoradiography with pimonidazole immunohistochemistry in human xenograft tumors.** *Radiother Oncol* 2006, **80**(2):157–164.
- [20] Busk M, Horsman MR, Overgaard J: **Resolution in PET hypoxia imaging: Voxel size matters.** *Acta Oncol* 2008, **47**(7):1201–1210.
- [21] Tannock IF: **Oxygen diffusion and the distribution of cellular radiosensitivity in tumours.** *Br J Radiol* 1972, **45**(535):515–524.
- [22] Daşu A, Toma-Daşu I, Karlsson M: **Theoretical simulation of tumour oxygenation and results from acute and chronic hypoxia.** *Phys Med Biol* 2003, **48**(17):2829–2842.
- [23] Secomb TW, Hsu R, Park EYH, Dewhirst MW: **Green’s function methods for analysis of oxygen delivery to tissues by microvascular networks.** *Ann Biomed Eng* 2004, **32**(11):1519–1529.
- [24] Kelly CJ, Brady M: **A model to simulate tumour oxygenation and dynamic [18F]-Fmiso PET data.** *Phys Med Biol* 2006, **51**(22):5859–5873.
- [25] Dewhirst MW: **Concepts of oxygen transport at the microcirculatory level.** *Semin Radiat Oncol* 1998, **8**(3):143–150.
- [26] Bristow RG, Hill RP: **Hypoxia and metabolism: Hypoxia, DNA repair and genetic instability.** *Nat Rev Cancer* 2008, **8**(3):180–192.
- [27] Bayer C, Shi K, Astner S, Maftai CA, Vaupel P: **Acute versus chronic hypoxia: why a simplified classification is simply not enough.** *Int J Radiat Oncol Biol Phys* 2011, **80**(4):965–968.
- [28] Nehmeh SA, Lee NY, Schröder H, Squire O, Zanzonico PB, Erdi YE, Greco C, Mageras G, Pham HS, Larson SM, Ling CC, Humm JL: **Reproducibility of Intratumor Distribution of 18F-Fluoromisonidazole in Head and Neck Cancer.** *Int J Radiat Oncol Biol Phys* 2008, **70**:235–242.
- [29] Okamoto S, Shiga T, Yasuda K, Ito YM, Magota K, Kasai K, Kuge Y, Shirato H, Tamaki N: **High Reproducibility of Tumor Hypoxia Evaluated by 18F-Fluoromisonidazole PET for Head and Neck Cancer.** *J Nucl Med* 2013.

- [30] Janssen HL, Haustermans KM, Balm AJ, Begg AC: **Hypoxia in head and neck cancer: How much, how important?** *Head and Neck* 2005, **27**(7):622–638.
- [31] Cárdenas-Navia LI, Secomb TW, Dewhirst MW: **Effects of fluctuating oxygenation on tirapazamine efficacy: Theoretical predictions.** *Int J Radiat Oncol Biol Phys* 2007, **67**(2):581–586.
- [32] Chaplin DJ, Olive PL, Durand RE: **Intermittent Blood Flow in a Murine Tumor: Radiobiological Effects.** *Cancer Res* 1987, **47**(2):597–601.
- [33] Dewhirst MW, Braun RD, Lanzen JL: **Temporal changes in pO₂ of R3230Ac tumors in fischer-344 rats.** *Int J Radiat Oncol Biol Phys* 1998, **42**(4):723–726.
- [34] Brown JM: **Evidence for acutely hypoxic cells in mouse tumours, and a possible mechanism of reoxygenation.** *Br J Radiol* 1979, **52**(620):650–656.
- [35] Rofstad EK, Gaustad JV, Egeland TA, Mathiesen B, Galappathi K: **Tumors exposed to acute cyclic hypoxic stress show enhanced angiogenesis, perfusion and metastatic dissemination.** *Int J Cancer* 2010, **127**(7):1535–1546.
- [36] Padhani AR, Krohn KA, Lewis JS, Alber M: **Imaging oxygenation of human tumours.** *Eur Radiol* 2007, **17**(4):861–872.
- [37] Hall EJ, Giaccia AJ: *Radiobiology for the Radiologist*. Philadelphia: Lippincott Williams and Wilkins, 6th edition 2006.
- [38] Overgaard J: **Hypoxic modification of radiotherapy in squamous cell carcinoma of the head and neck – A systematic review and meta-analysis.** *Radiother Oncol* 2011, **100**:22–32.
- [39] Janssens GO, Rademakers SE, Terhaard CH, Doornaert PA, Bijl HP, van den Ende P, Chin A, Marres HA, de Bree R, van der Kogel AJ, Hoogsteen IJ, Bussink J, Span PN, Kaanders JH: **Accelerated radiotherapy with carbogen and nicotinamide for laryngeal cancer: results of a phase III randomized trial.** *J Clin Oncol* 2012, **30**(15):1777–1783.
- [40] Overgaard J, Sand Hansen H, Overgaard M, Bastholt L, Berthelsen A, Specht L, Lindeløv B, Jørgensen K: **A randomized double-blind phase**

- III study of nimorazole as a hypoxic radiosensitizer of primary radiotherapy in supraglottic larynx and pharynx carcinoma. Results of the Danish Head and Neck Cancer Study (DAHANCA) Protocol 5-85.** *Radiother Oncol* 1998, **46**(2):135–146.
- [41] Yaromina A, Krause M, Baumann M: **Individualization of cancer treatment from radiotherapy perspective.** *Mol Oncol* 2012, **6**(2):211–221.
- [42] Bentzen SM: **Theragnostic imaging for radiation oncology: dose-painting by numbers.** *Lancet Oncol* 2005, **6**(2):112–117.
- [43] Søvik Å, Malinen E, Olsen DR: **Strategies for biologic image-guided dose escalation: A review.** *Int J Radiat Oncol Biol Phys* 2009, **73**(3):650–658.
- [44] Collingridge DR, Young WK, Vojnovic B, Wardman P, Lynch EM, Hill SA, Chaplin DJ: **Measurement of Tumor Oxygenation: A Comparison between Polarographic Needle Electrodes and a Time-Resolved Luminescence-Based Optical Sensor.** *Radiat Res* 1997, **147**(3):329–334.
- [45] Hoskin PJ, Carnell DM, Taylor NJ, Smith RE, Stirling JJ, Daley FM, Saunders MI, Bentzen SM, Collins DJ, d’Arcy JA, Padhani AP: **Hypoxia in Prostate Cancer: Correlation of BOLD-MRI With Pimonidazole Immunohistochemistry—Initial Observations.** *Int J Radiat Oncol Biol Phys* 2007, **68**(4):1065–1071.
- [46] Rasey JS, Koh WJ, Grierson JR, Grunbaum Z, Krohn KA: **Radiolabeled fluoromisonidazole as an imaging agent for tumor hypoxia.** *Int J Radiat Oncol Biol Phys* 1989, **17**(5):985–991.
- [47] Machulla HJ (Ed): *Imaging of Hypoxia: Tracer Developments.* Dordrecht: Kluwer Academic Publishers 1999.
- [48] Koh WJ, Rasey JS, Evans ML, Grierson JR, Lewellen TK, Graham MM, Krohn KA, Griffin TW: **Imaging of hypoxia in human tumors with [F-18]fluoromisonidazole.** *Int J Radiat Oncol Biol Phys* 1992, **22**:199–212.
- [49] Beyer T, Townsend DW, Brun T, Kinahan PE, Charron M, Roddy R, Jerin J, Young J, Byars L, Nutt R: **A Combined PET/CT Scanner for Clinical Oncology.** *J Nucl Med* 2000, **41**(8):1369–1379.

- [50] Elmpt Wv, Öllers M, Dingemans AMC, Lambin P, Ruyscher DD: **Response Assessment Using 18F-FDG PET Early in the Course of Radiotherapy Correlates with Survival in Advanced-Stage Non-Small Cell Lung Cancer.** *J Nucl Med* 2012, **53**(10):1514–1520.
- [51] Bushberg JT, Seibert JA, Leidholdt EM Jr, Boone JM: *The essential physics of medical imaging.* Philadelphia: Lippincott Williams and Wilkins, second edition 2002.
- [52] Townsend DW, Defrise M: **Image-reconstruction methods in positron tomography.** *CERN Academic Training Lecture* 1993, **CERN 93-02**, [[<http://cds.cern.ch/record/250967>]].
- [53] Shepp LA, Vardi Y: **Maximum Likelihood Reconstruction for Emission Tomography.** *IEEE Trans Med Imaging* 1982, **1**(2):113–122.
- [54] Jakoby BW, Bercier Y, Conti M, Casey ME, Bendriem B, Townsend DW: **Physical and clinical performance of the mCT time-of-flight PET/CT scanner.** *Phys Med Biol* 2011, **56**(8):2375–2389.
- [55] Casciari JJ, Graham MM, Rasey JS: **A modeling approach for quantifying tumor hypoxia with [F-18]fluoromisonidazole PET time-activity data.** *Med Phys* 1995, **22**(7):1127–1139.
- [56] Gross MW, Karbach U, Groebe K, Franko AJ, Mueller-Klieser W: **Calibration of misonidazole labeling by simultaneous measurement of oxygen tension and labeling density in multicellular spheroids.** *Int J Cancer* 1995, **61**:567–573.
- [57] Grunbaum Z, Freauff SJ, Krohn KA, Wilbur DS, Magee S, Rasey JS: **Synthesis and characterization of congeners of misonidazole for imaging hypoxia.** *J Nucl Med* 1987, **28**:68–75.
- [58] Eschmann SM, Paulsen F, Bedeshem C, Machulla HJ, Hehr T, Bamberg M, Bares R: **Hypoxia-imaging with 18F-Misonidazole and PET: Changes of kinetics during radiotherapy of head-and-neck cancer.** *Radiother Oncol* 2007, **83**(3):406–410.
- [59] Thorwarth D, Eschmann SM, Paulsen F, Alber M: **A Model of Reoxygenation Dynamics of Head-And-Neck Tumors Based on Serial 18F-Fluoromisonidazole Positron Emission Tomography Investigations.** *Int J Radiat Oncol Biol Phys* 2007, **68**(2):515–521.

-
- [60] Kumar P, Stypinski D, Xia H, McEwan AJB, Machulla HJ, Wiebe LI: **Fluoroazomycin arabinoside (FAZA): synthesis, 2H and 3H-labelling and preliminary biological evaluation of a novel 2-nitroimidazole marker of tissue hypoxia.** *J Labelled Cpd Radiopharm* 1999, **42**:3–16.
- [61] Basken NE, Green MA: **Cu(II) bis(thiosemicarbazone) radiopharmaceutical binding to serum albumin: further definition of species dependence and associated substituent effects.** *Nucl Med Biol* 2009, **36**(5):495–504.
- [62] Secomb TW, Beard DA, Frisbee JC, Smith NP, Pries AR: **The Role of Theoretical Modeling in Microcirculation Research.** *Microcirc* 2008, **15**(8):693–698.
- [63] Popel AS: **Theory of oxygen transport to tissue.** *Crit Rev Biomed Eng* 1989, **17**(3):257–321.
- [64] Goldman D: **Theoretical models of microvascular oxygen transport to tissue.** *Microcirc* 2008, **15**(8):795–811.
- [65] Eggleton CD, Vadapalli A, Roy TK, Popel AS: **Calculations of intracapillary oxygen tension distributions in muscle.** *Math Biosci* 2000, **167**(2):123–143.
- [66] Boucher Y, Leunig M, Jain RK: **Tumor Angiogenesis and Interstitial Hypertension.** *Cancer Res* 1996, **56**(18):4264–4266.
- [67] Stohrer M, Boucher Y, Stangassinger M, Jain RK: **Oncotic pressure in solid tumors is elevated.** *Cancer Res* 2000, **60**(15):4251–4255.
- [68] Takeuchi J, Sobue M, Yoshida M, Uchibori N, Sato E, Miura K: **A high level of glycosaminoglycan-synthesis of squamous cell carcinoma of the parotid gland.** *Cancer* 1981, **47**(8):2030–2035.
- [69] Jain RK: **Transport of molecules in the tumor interstitium: A review.** *Cancer Res* 1987, **47**(12):3039–3051.
- [70] Brizel DM, Klitzman B, Cook JM, Edwards J, Rosner G, Dewhirst MW: **A comparison of tumor and normal tissue microvascular hematocrits and red cell fluxes in a rat window chamber model.** *Int J Radiat Oncol Biol Phys* 1993, **25**(2):269–276.
- [71] Cowan DSM, Hicks KO, Wilson WR: **Multicellular membranes as an in vitro model for extravascular diffusion in tumours.** *Br J Cancer* 1996, **74**:S28–31.

- [72] Jain RK: **Transport of molecules across tumour vasculature.** *Cancer Metast Rev* 1987, **6**(4):559–593.
- [73] Thomlinson RH, Gray LH: **The histological structure of some human lung cancers and the possible implications for radiotherapy.** *Br J Cancer* 1955, **9**(4):539–549.
- [74] Bussink J, Kaanders JHAM, Rijken PFJW, Raleigh JA, Van der Kogel AJ: **Changes in Blood Perfusion and Hypoxia after Irradiation of a Human Squamous Cell Carcinoma Xenograft Tumor Line.** *Radiat Res* 2000, **153**(4):398–404.
- [75] Rijken PF, Bernsen HJ, Peters JP, Hodgkiss RJ, Raleigh JA, van der Kogel AJ: **Spatial relationship between hypoxia and the (perfused) vascular network in a human glioma xenograft: a quantitative multi-parameter analysis.** *Int J Radiat Oncol Biol Phys* 2000, **48**(2):571–582.
- [76] Lanman D: **bfilter2.** MATLAB Central 2006. [Retrieved June 15 2009 from <http://www.mathworks.de/matlabcentral/fileexchange/12191>].
- [77] *MATLAB version 7.6 (R2008a).* Natick, Massachusetts: The MathWorks Inc. 2008.
- [78] *MATLAB online help: The Parabolic Equation.* Natick, Massachusetts: The MathWorks Inc. 2008.
- [79] Griffiths JR, Robinson SP: **The OxyLite: a fibre-optic oxygen sensor.** *Br J Radiol* 1999, **72**:627–630.
- [80] Konerding MA, Fait E, Gaumann A: **3D microvascular architecture of pre-cancerous lesions and invasive carcinomas of the colon.** *Br J Cancer* 2001, **84**(10):1354–1362.
- [81] Berg HC: *Random Walks in Biology.* Princeton University Press 1983.
- [82] Bruehlmeier M, Roelcke U, Schubiger PA, Ametamey SM: **Assessment of Hypoxia and Perfusion in Human Brain Tumors Using PET with 18F-Fluoromisonidazole and 15O-H₂O.** *J Nucl Med* 2004, **45**(11):1851–1859.
- [83] Shi K, Souvatzoglou M, Astner ST, Vaupel P, Nüsslin F, Wilkens JJ, Ziegler SI: **Quantitative Assessment of Hypoxia Kinetic Models by a Cross-Study of Dynamic 18F-FAZA and 15O-H₂O in Patients with Head and Neck Tumors.** *J Nucl Med* 2010, **51**(9):1386–1394.

-
- [84] Zips D, Zöphel K, Abolmaali N, Perrin R, Abramyuk A, Haase R, Appold S, Steinbach J, Kotzerke J, Baumann M: **Exploratory prospective trial of hypoxia-specific PET imaging during radiochemotherapy in patients with locally advanced head-and-neck cancer.** *Radiother Oncol* 2012, in press.
- [85] Lee JA: **Segmentation of positron emission tomography images: Some recommendations for target delineation in radiation oncology.** *Radiother Oncol* 2010, **96**(3):302–307.
- [86] Thorwarth D, Geets X, Paiusco M: **Physical radiotherapy treatment planning based on functional PET/CT data.** *Radiother Oncol* 2010, **96**(3):317–24.
- [87] Thorwarth D, Eschmann SM, Paulsen F, Alber M: **A kinetic model for dynamic 18F-Fmiso PET data to analyse tumour hypoxia.** *Phys Med Biol* 2005, **50**(10):2209–2224.
- [88] Shukla-Dave A, Lee NY, Jansen JFA, Thaler HT, Stambuk HE, Fury MG, Patel SG, Moreira AL, Sherman E, Karimi S, Wang Y, Kraus D, et al.: **Dynamic contrast-enhanced magnetic resonance imaging as a predictor of outcome in head-and-neck squamous cell carcinoma patients with nodal metastases.** *Int J Radiat Oncol Biol Phys* 2012, **82**(5):1837–1844.
- [89] Kimura H, Braun RD, Ong ET, Hsu R, Secomb TW, Papahadjopoulos D, Hong K, Dewhirst MW: **Fluctuations in Red Cell Flux in Tumor Microvessels Can Lead to Transient Hypoxia and Reoxygenation in Tumor Parenchyma.** *Cancer Res* 1996, **56**(23):5522–5528.
- [90] Brurberg KG, Graff BA, Olsen DR, Rofstad EK: **Tumor-line specific pO₂ fluctuations in human melanoma xenografts.** *Int J Radiat Oncol Biol Phys* 2004, **58**(2):403 – 409.
- [91] Bennewith KL, Durand RE: **Quantifying transient hypoxia in human tumor xenografts by flow cytometry.** *Cancer Res* 2004, **64**(17):6183–6189.
- [92] Durand RE, Aquino-Parsons C: **Clinical Relevance of Intermittent Tumour Blood Flow.** *Acta Oncol* 2001, **40**(8):929–936.
- [93] Cárdenas-Navia LI, Mace D, Richardson RA, Wilson DF, Shan S, Dewhirst MW: **The pervasive presence of fluctuating oxygenation in tumors.** *Cancer Res* 2008, **68**(14):5812–5819.

- [94] Pigott K, Hill S, Chaplin D, Saunders M: **Microregional fluctuations in perfusion within human tumours detected using laser Doppler flowmetry.** *Radiother Oncol* 1996, **40**:45–50.
- [95] Lanzen J, Braun RD, Klitzman B, Brizel D, Secomb TW, Dewhirst MW: **Direct Demonstration of Instabilities in Oxygen Concentrations within the Extravascular Compartment of an Experimental Tumor.** *Cancer Res* 2006, **66**(4):2219–2223.
- [96] Wang K, Yorke E, Nehmeh SA, Humm JL, Ling CC: **Modeling acute and chronic hypoxia using serial images of [18F]-FMISO PET.** *Med Phys* 2009, **36**(10):4400–4408.
- [97] Maftai CA, Shi K, Bayer C, Astner S, Vaupel P: **Comparison of (immuno-)fluorescence data with serial [18F]Fmiso PET/CT imaging for assessment of chronic and acute hypoxia in head and neck cancers.** *Radiother Oncol* 2011, **99**:412–417.
- [98] Maftai CA, Bayer C, Shi K, Astner S, Vaupel P: **Quantitative assessment of hypoxia subtypes in microcirculatory supply units of malignant tumors Using (immuno-)fluorescence techniques.** *Strahlenther Onkol* 2011, **187**(4):260–266.
- [99] Jensen AR, Nellesmann HM, Overgaard J: **Tumor progression in waiting time for radiotherapy in head and neck cancer.** *Radiother Oncol* 2007, **84**:5–10.
- [100] Bentzen L, Keiding S, Nordmark M, Falborg L, Hansen SB, Keller J, Nielsen OS, Overgaard J: **Tumour oxygenation assessed by 18F-fluoromisonidazole PET and polarographic needle electrodes in human soft tissue tumours.** *Radiother Oncol* 2003, **67**(3):339–344.
- [101] Gagel B, Piroth M, Pinkawa M, Reinartz P, Zimny M, Kaiser H, Stanzel S, Asadpour B, Demirel C, Hamacher K, Coenen H, Scholbach T, et al.: **pO polarography, contrast enhanced color duplex sonography (CDS), [18F] fluoromisonidazole and [18F] fluorodeoxyglucose positron emission tomography: validated methods for the evaluation of therapy-relevant tumor oxygenation or only bricks in the puzzle of tumor hypoxia?** *BMC Cancer* 2007, **7**:113.
- [102] Mortensen LS, Buus S, Nordmark M, Bentzen L, Munk OL, Keiding S, Overgaard J: **Identifying hypoxia in human tumors: A correla-**

- tion study between **18F-FMISO PET** and the Eppendorf oxygen-sensitive electrode. *Acta Oncol* 2010, **49**(7):934–940.
- [103] Bentzen L, Keiding S, Horsman MR, Grönroos T, Hansen SB, Overgaard J: **Assessment of Hypoxia in Experimental Mice Tumours by [18F] Fluoromisonidazole PET and pO₂ Electrode Measurements.** *Acta Oncol* 2002, **41**(3):304–312.
- [104] O'Donoghue JA, Zanzonico P, Pugachev A, Wen B, Smith-Jones P, Cai S, Burnazi E, Finn RD, Burgman P, Ruan S, Lewis JS, Welch MJ, et al.: **Assessment of regional tumor hypoxia using 18F-fluoromisonidazole and 64Cu(II)-diacetyl-bis(N4-methylthiosemicarbazone) positron emission tomography: Comparative study featuring microPET imaging, Po₂ probe measurement, autoradiography, and fluorescent microscopy in the R3327-AT and FaDu rat tumor models.** *Int J Radiat Oncol Biol Phys* 2005, **61**(5):1493–1502.
- [105] Sørensen M, Horsman MR, Cumming P, Munk OL, Keiding S: **Effect of intratumoral heterogeneity in oxygenation status on FMISO PET, autoradiography, and electrode Po₂ measurements in murine tumors.** *Int J Radiat Oncol Biol Phys* 2005, **62**(3):854–861.
- [106] Bartlett RM, Beattie BJ, Naryanan M, Georgi JC, Chen Q, Carlin SD, Roble G, Zanzonico PB, Gonen M, O'Donoghue J, Fischer A, Humm JL: **Image-Guided Po₂ Probe Measurements Correlated with Parametric Images Derived from 18F-Fluoromisonidazole Small-Animal PET Data in Rats.** *J Nucl Med* 2012, **53**(10):1608–1615.
- [107] Ljungkvist AS, Bussink J, Kaanders JH, Rijken PF, Begg AC, Raleigh JA, van der Kogel AJ: **Hypoxic cell turnover in different solid tumor lines.** *Int J Radiat Oncol Biol Phys* 2005, **62**(4):1157–1168.
- [108] Jain RK: **Delivery of molecular and cellular medicine to solid tumors.** *Adv Drug Deliver Rev* 2001, **46**(1–3):149–168.
- [109] Mönnich D, Troost EGC, Kaanders JHAM, Oyen WJG, Alber M, Thorwarth D: **Modelling and simulation of [18F]fluoromisonidazole dynamics based on histology-derived microvessel maps.** *Phys Med Biol* 2011, **56**(7):2045–2057.
- [110] Mönnich D, Troost EGC, Kaanders JHAM, Oyen WJG, Alber M, Thorwarth D: **Modelling and simulation of the influence of acute and**

- chronic hypoxia on [18F]fluoromisonidazole PET imaging.** *Phys Med Biol* 2012, **57**(6):1675–1684.
- [111] Ljungkvist ASE, Bussink J, Kaanders JHAM, Wiedenmann NE, Vlasman R, van der Kogel AJ: **Dynamics of Hypoxia, Proliferation and Apoptosis after Irradiation in a Murine Tumor Model.** *Radiat Res* 2006, **165**(3):326–336.
- [112] Lagerlöf JH, Kindblom J, Cortez E, Pietras K, Bernhardt P: **Image-based 3D modeling study of the influence of vessel density and blood hemoglobin concentration on tumor oxygenation and response to irradiation.** *Med Phys* 2013, **40**(2):024101.
- [113] Cho H, Ackerstaff E, Carlin S, Lupu ME, Wang Y, Rizwan A, O'Donoghue J, Ling CC, Humm JL, Zanzonico PB, Koutcher JA: **Noninvasive multimodality imaging of the tumor microenvironment: Registered dynamic magnetic resonance imaging and positron emission tomography studies of a preclinical tumor model of tumor hypoxia.** *Neoplasia* 2009, **11**(3):247–259.
- [114] Jan S, Santin G, Strul D, Staelens S, et al.: **GATE: a simulation toolkit for PET and SPECT.** *Phys Med Biol* 2004, **49**(19):4543–4561.

Acknowledgements

First and foremost, I would like to express my gratitude to Daniela Thorwarth for guiding and encouraging me along the way. Without her insight, pragmatism and kindness this work would not have been possible.

I also owe thanks to Markus Alber, whose bright ideas shaped this work in many ways. His straightforward style never failed to impress me.

Furthermore, I thank Esther Troost, Hans Kaanders and Wim Oyen for contributing important insights into tumour biology as well as for patient proofreading of various manuscripts.

I wish to thank all members of the Biomedical Physics group for creating a warm atmosphere and for making me quickly feel at home in Tübingen: Benjamin, Sara, Martin, Oliver, Matthias, Bettina, Birgit, Linda, Jens, Liv, Marcin, Philip, Josip, Boris and Katharina. Special thanks go to my former office mate Alexander Horst for sharing countless jokes and lessons improvising experiments.

Thanks to my family for keeping wondering what exactly I am working on. Last but not least, I thank Manu for giving me the strength to pursue this work.

A. Modelling and simulation of [¹⁸F]fluoromisonidazole dynamics based on histology-derived microvessel maps

published in

Physics in Medicine and Biology 2011, **56**: 2045–2057.

Modelling and simulation of [^{18}F]fluoromisonidazole dynamics based on histology-derived microvessel maps

David Mönnich¹, Esther G C Troost², Johannes H A M Kaanders²,
Wim J G Oyen³, Markus Alber⁴ and Daniela Thorwarth¹

¹ Section for Biomedical Physics, University Hospital for Radiation Oncology,
Hoppe-Seyler-Straße 3, 72076 Tübingen, Germany

² Institute of Oncology, Radiation Oncology, Radboud University Nijmegen Medical Centre,
PO Box 9101, 6500 HB Nijmegen, The Netherlands

³ Institute of Oncology, Nuclear Medicine, Radboud University Nijmegen Medical Centre,
PO Box 9101, 6500 HB Nijmegen, The Netherlands

⁴ University Hospital for Radiation Oncology, Hoppe-Seyler-Straße 3, 72076 Tübingen, Germany

E-mail: david.moennich@med.uni-tuebingen.de

Received 3 January 2011, in final form 7 February 2011

Published 8 March 2011

Online at stacks.iop.org/PMB/56/2045

Abstract

Hypoxia can be assessed non-invasively by positron emission tomography (PET) using radiotracers such as [^{18}F]fluoromisonidazole (Fmiso) accumulating in poorly oxygenated cells. Typical features of dynamic Fmiso PET data are high signal variability in the first hour after tracer administration and slow formation of a consistent contrast. The purpose of this study is to investigate whether these characteristics can be explained by the current conception of the underlying microscopic processes and to identify fundamental effects. This is achieved by modelling and simulating tissue oxygenation and tracer dynamics on the microscopic scale. In simulations, vessel structures on histology-derived maps act as sources and sinks for oxygen as well as tracer molecules. Molecular distributions in the extravascular space are determined by reaction–diffusion equations, which are solved numerically using a two-dimensional finite element method. Simulated Fmiso time activity curves (TACs), though not directly comparable to PET TACs, reproduce major characteristics of clinical curves, indicating that the microscopic model and the parameter values are adequate. Evidence for dependence of the early PET signal on the vascular fraction is found. Further, possible effects leading to late contrast formation and potential implications on the quantification of Fmiso PET data are discussed.

(Some figures in this article are in colour only in the electronic version)

1. Introduction

Tumour hypoxia strongly affects radiotherapy (RT) outcome (Höckel *et al* 1993, Nordmark *et al* 2005). It is caused by the structurally and functionally abnormal microvessel networks in tumours (Vaupel 2004). Hypoxia may be chronic or acute. Chronic hypoxia is constantly present and is caused by a mismatch between oxygen supply and demand resulting from increased distances between vessels and tumour cells or the presence of underperfused vessels. Fluctuating perfusion can cause acute hypoxia in addition to chronic baseline conditions (Dewhirst 1998). In this paper we focus on the former effect.

One reason for RT failure is the lower radiosensitivity of hypoxic cancer cells compared to normoxic ones (Thomlinson and Gray 1955). Hypoxia can lead to a non-uniform radiation response within treatment volumes, while it is still clinical practice to provide uniform dose distributions. To compensate for hypoxia-induced treatment resistance, dose painting (DP) of RT target volumes has been proposed (Ling *et al* 2000, Bentzen 2005). Applying an increased dose to small sub-volumes is technically feasible by means of intensity modulated RT (Chao *et al* 2001, Alber *et al* 2003, Thorwarth *et al* 2007). The local oxygenation of tumours can be non-invasively assessed by positron emission tomography (PET) imaging using radiolabelled tracers accumulating in hypoxic cells, such as Fmiso⁵ (Rasey *et al* 1996), Faza⁶ (Piert *et al* 2005), Cu-ATSM⁷ (Dehdashti *et al* 2003), EF5⁸ (Komar *et al* 2008), EF3⁹ (Mahy *et al* 2008) and HX4¹⁰ (van Loon *et al* 2010). Kinetic analysis has been proposed as a method to quantify dynamic Fmiso PET data (Thorwarth *et al* 2005a). Still, no consensus has yet been found on how to correctly interpret hypoxia PET data and how to effectively use them in clinical practice (Søvik *et al* 2009).

Voxel-based dynamic PET data show two major characteristics: a highly variable nonlinear curve during the first hour after tracer administration, in some cases a pronounced peak, is followed by an approximately linearly sloped signal. This was observed e.g. for Faza (Souvatzoglou *et al* 2007), Fmiso (Koh *et al* 1992, Eschmann *et al* 2005, Wang *et al* 2010) and EF5 (Komar *et al* 2008). The late slope depends on the local cell density, cellular oxygenation, vascular fraction and tracer plasma clearance rate. It can take hours until a consistent contrast is observed in clinical hypoxia PET images, i.e. until the sign of the difference between any two voxel intensities is stable. The purpose of this study was to investigate whether these clinical observations can be explained by the current conception of the microscopic processes determining Fmiso distribution and retention. Specifically, that Fmiso is transported by passive diffusion, and that the pO₂ dependent binding is irreversible and can be described as a first-order reaction (Thorwarth *et al* 2005b). To answer these questions, Fmiso microdynamics were modelled and simulated in a two-step process starting with the simulation of static tissue oxygenation. Existing methods were adapted and extended, resulting in a quantitative conceptual model characterized by assumed mechanisms and the use of optimized parameter values in the lack of published values.

⁵ [18F]fluoromisonidazole.

⁶ 1-(5-[18F]Fluoro-5-deoxy- α -D-arabinofuranosyl)-2-nitroimidazole.

⁷ [61Cu]Copper(II)diacetyl-di(N4-methylthiosemicarbazone).

⁸ 2-(2-nitro-1H-imidazol-1-yl)-N-(2,2,3,3,3-[18F]pentafluoropropyl)-acetamide.

⁹ 2-(2-nitro-1H-imidazol-1-yl)-N-(3,3,3-[18F]trifluoropropyl)-acetamide.

¹⁰ 3-[18F]fluoro-2-(4-((2-nitro-1H-imidazol-1-yl)methyl)-1H-1,2,3-triazol-1-yl)propan-1-ol.

2. Model

2.1. Tissue oxygenation

Previous research focusing on the path of O_2 molecules from their haemoglobin bound state to extravasation was reviewed by Popel (1989) and Goldman (2008). A model taking into account relevant effects was fitted to experimental data to derive a lump permeability coefficient L_{O_2} depending on blood haematocrit only (Eggleton *et al* 2000). This coefficient links the oxygen flux through vessel walls J_{O_2} to the oxygen tension in erythrocytes P_{ie} and on the extravascular side of the wall P :

$$J_{O_2} = L_{O_2} (P_{ie} - P). \quad (1)$$

Previously, oxygen distributions in tumour tissues were simulated based on three-dimensional vessel maps derived from confocal microscopy (Secomb *et al* 2004), two-dimensional maps manually delineated on H&E-stained tissue sections (Pogue *et al* 2001) and two- and three-dimensional maps artificially generated from empirical parameters (Daşu *et al* 2003, Toma-Daşu *et al* 2009). All authors modelled oxygen transport as a diffusive process (diffusion coefficient D_{O_2}) that is in equilibrium with cellular oxygen consumption. While Pogue *et al* assumed a constant consumption rate, in this paper we adopt the approach of Secomb *et al* and Daşu *et al* using a Michaelis–Menten relationship between oxygen tension P and consumption rate $M(P)$. Specifically, the consumption rate is almost constant at high oxygen levels (rate M_0) and drops sharply at low levels, when cells adapt to limited supply. The half-maximal rate is reached for $P = P_0$. This aggregates in the reaction–diffusion equation for tissue oxygenation:

$$\frac{\partial P}{\partial t} = D_{O_2} \nabla^2 P - M(P) = D_{O_2} \nabla^2 P - \frac{M_0 P}{P + P_0}. \quad (2)$$

Diffusion along concentration gradients is introduced by the Laplacian operator ∇^2 , which is the sum of second-order spatial partial derivatives. Quasistatic distributions can be calculated by numerically solving equation (2) until temporal variations are below a specified threshold.

2.2. Fmiso dynamics

Previously, diffusion and binding of Fmiso and Cu-ATSM in tumours were simulated, employing vessel maps statistically generated from empirical microvessel distribution parameters (Kelly and Brady 2006, Dalah *et al* 2010). The method presented in this paper extends towards the use of more straightforward histology-derived vessel maps and an explicitly oxygen-dependent binding rate $K(P)$. As for oxygen, tracer flux across vessel walls J_T is assumed to be proportional to the difference between concentration on the intravascular C_{iv} and extravascular C side:

$$J_T = L_T (C_{iv} - C). \quad (3)$$

The tracer permeability coefficient is denoted by L_T . To model Fmiso dynamics, we follow the approach of Kelly *et al* by assuming that diffusion is the dominant transport mechanism (diffusion coefficient D_T), that tracer binding in cells can be described as a first-order reaction (rate constant K), and that binding is irreversible on timescales relevant for hypoxia PET imaging. This agrees with kinetic models used to analyse dynamic hypoxia PET data (Wang *et al* 2009, Thorwarth *et al* 2005b). To summarize the stated assumptions in a mathematical expression, the tracer concentration C is separated into a free C_f and a bound C_b component:

$$\frac{\partial C_f}{\partial t} = D_T \nabla^2 C_f - K(P) C_f \quad (4)$$

$$\frac{\partial C_b}{\partial t} = K(P)C_f. \quad (5)$$

A hyperbolic relationship $F_1(P)$ between the cellular Fmiso binding rate and oxygen tension was derived by Casciari *et al* (1995). It is parameterized by the maximal binding rate under anoxic conditions K_{\max} and the oxygen tension P_1 at which binding is inhibited by 50%:

$$F_1 = \frac{K_{\max} P_1}{P + P_1}. \quad (6)$$

Calculations of tissue oxygenation showed that some cells are exposed to extremely low oxygen levels. It appears realistic to assume cell death as the consequence, as necrosis is also present in H&E-stained tissue sections. It is modelled by a function $F_2(P)$ exhibiting a sharp drop from value 1 (all cells vital) to 0 (all cells dead) at a critical oxygen tension P_2 :

$$F_2 = \left(\frac{P}{P + P_2} \right)^k. \quad (7)$$

The dimensionless parameter k controls the width of the transition layer between vital and necrotic regions. Considering that Fmiso only accumulates in vivid cells the effective binding rate constant is $K(P) = F_1(P) \cdot F_2(P)$. Similar binding characteristics were reported as ribbon-like hypoxic structures in tissue sections dual-stained for vessels and hypoxia (Ljungkvist *et al* 2002). By defining the binding rate solely on the basis of local pO_2 the total cell density in the extravascular space is inherently considered homogeneous. It is further assumed that convective transport is negligible compared to diffusive transport in the extravascular space and across vessel membranes. In the extravascular space, this is justified for the rapidly diffusing O_2 molecule, but not necessarily for larger tracer molecules, where the dominant transport mechanism depends on different tissue properties (Jain 1987b). Transmembrane transport is diffusion dominated in tumours since hydrostatic and oncotic pressure differences across vessel walls are small due to the leaky nature of vessels (Boucher and Jain 1992, Stohrer *et al* 2000).

3. Methods and materials

In this section the practical aspects of simulating spatiotemporal Fmiso distributions based on the mathematical model presented in the preceding section are described and the employed materials are specified.

3.1. Stained microsections

Frozen tissue sections from human head-and-neck xenograft tumour lines were immunohistochemically stained for endothelial structures (9F1, rat monoclonal to mouse endothelium (Department of Pathology, Radboud University Nijmegen Medical Centre, Nijmegen, The Netherlands)) and hypoxia (Pimonidazole, (Natural Pharmacia International, Research Triangle Park, NC, USA)); anti-pimonidazole, (gift from J A Raleigh, Department of Radiation Oncology, University of North Carolina, School of Medicine, Chapel Hill, NC, USA) as described previously (Bussink *et al* 2000). All tumour sections were scanned using a digital image analysis system as described previously resulting in grey-scale images for both fluorescent signals (Rijken *et al* 2000). Consecutive tissue sections were stained with hematoxylin and eosin (H&E) to distinguish vital from necrotic tissue.

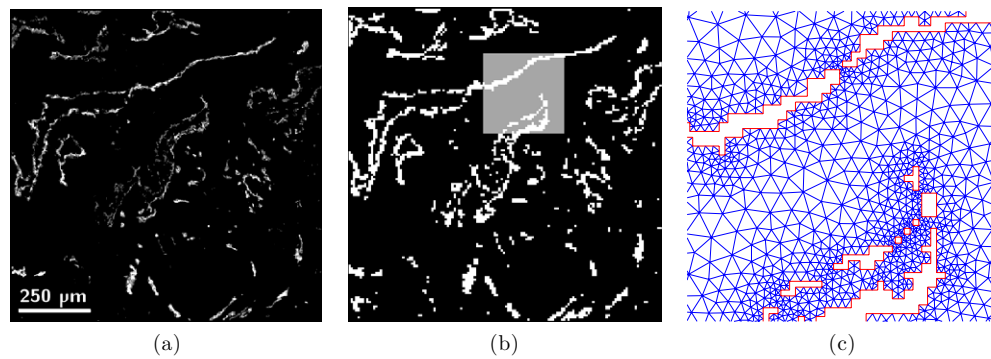


Figure 1. (a) Tissue microsection immunohistochemically stained for endothelium (9F1). (b) Image after binarization and resolution reduction. (c) FEM mesh in the region highlighted in (b).

3.2. Generation of vessel maps

The finite element method (FEM) applied to solve the reaction–diffusion equations given in section 2 is based on a triangular tessellation (mesh) of the integration domain. In the present case, this domain consists of extravascular space interspersed by vessels, which constitute holes in the mesh (figure 1(c)). Transport across vessel walls is reproduced by appropriate boundary conditions specified later. A set of vertices describing the vessel distribution is extracted from tissue microsections stained for vascular structures (figure 1(a)) by the following steps. First, the image is binarized using a threshold determined by the mean background intensity. In the next step the resolution of the binarized image is reduced. This restrains computer memory usage, because the mesh size strongly depends on the minimum structure size in the map. The output is a 2D binary vessel map with a pixel size of $8\mu\text{m}$ (figure 1(b)). Thus, a single pixel has approximately the same circumference as a circular vessel with a diameter of $10\mu\text{m}$, which is roughly the smallest physiologically realistic value. Due to the fact that the vessel surface area (length in 2D) is the most important factor for transport between blood and tissue, it is confirmed that it is not changed by the resolution reduction. The vascular fraction of 3% in the simulation map used in this work is comparable to other published values (Jain 1988).

3.3. Simulation of spatiotemporal Fmiso distributions

The simulation of spatiotemporal Fmiso distributions was implemented in a two-step process in Matlab R2008a.

Oxygen. In the first step the quasistatic oxygen distribution $P_s(x, y)$ in a vessel map was calculated by numerically solving equation (2) until relative temporal variations were below $0.2\% s^{-1}$. A solver for linear partial differential equations was extended to iteratively adapt the nonlinear consumption rate $M(P)$. The intraerythrocytic oxygen tension was assumed to be uniform, neglecting axial gradients or differences between vessels in pO_2 . Transmembrane fluxes J as defined in the modelling section were realized via Robin boundary conditions imposed on the vessel boundaries. For oxygen they read $\mathbf{n} \cdot (D_{O_2} \nabla P) = J_{O_2}$, where \mathbf{n} is the normal unit vector to the respective boundary segment. No-flux boundary conditions were applied to the edges of the vessel map for oxygen as well as tracer molecules.

Table 1. Parameter values used in simulations. The bold value was used where ranges are given.

| Symbol | Meaning | Value | Reference |
|------------|--|---|---|
| Oxygen | | | |
| P_{ie} | Intraerythrocyte pO ₂ in tumours | 40 mmHg | Secomb <i>et al</i> (2004) |
| L_{O_2} | Capillary permeability to O ₂ for tumour haematocrit of 19% | $4.1 \times 10^{-4} \text{ m s}^{-1}$ | Eggleton <i>et al</i> (2000)/ Brizel <i>et al</i> (1993) |
| D_{O_2} | O ₂ diffusion coefficient | $2 \times 10^{-9} \text{ m}^2 \text{ s}^{-1}$ | Tannock (1972) |
| M_0 | Maximum O ₂ consumption rate | 15 mmHg s^{-1} | Daşu <i>et al</i> (2003) |
| P_0 | Michaelis–Menten coefficient of oxygen consumption | (2.0–2.5) mmHg | Goldman (2008) and Daşu <i>et al</i> (2003) |
| Fmiso | | | |
| L_T | Capillary permeability to Fmiso | (2.4–9.4) $\times 10^{-5} \text{ m s}^{-1}$ | Kelly and Brady (2006) |
| D_T | Miso diffusion coefficient | $5.5 \times 10^{-11} \text{ m}^2 \text{ s}^{-1}$ | Cowan <i>et al</i> (1996) |
| P_1 | pO ₂ inhibiting binding by 50% | (0.8–1.5) mmHg | Rasey <i>et al</i> (1989) |
| K_{\max} | Maximum binding rate (anoxia) | $1.7 \times 10^{-4} \text{ s}^{-1}$ | Optimized |
| P_2 | pO ₂ inducing 50% necrosis | 0.1 mmHg | Simulated pO ₂ approximately 120 μm from vessels |
| k | Determines step width at P_2 | 0.3 | Optimized |

Fmiso. In the second step local tracer binding rates $K(P_s(x, y))$ were calculated from the simulated oxygenation. Eventually, diffusion and binding of tracer were simulated by solving the coupled linear equations (4) and (5). The plasma tracer concentration was specified as a function of time that was fitted to clinical decay-corrected data measured from multiple blood samples. The output was a set of spatial tracer distributions at predefined time points. By averaging tracer concentrations in designated regions it is possible to obtain time activity curves (TACs).

3.4. Parameter values

An overview of parameter values used in this work is given in table 1. Ranges of realistic parameter values are naturally broad because of large inter- and intra-tumoural variations in physiology.

Oxygen. An intraerythrocyte pO₂ of $P_{ie} = 40 \text{ mmHg}$ was assumed. This is the approximate value at arteriolar capillary ends. The same value was used for the intravascular pO₂ in previous approaches (Secomb *et al* 2004, Daşu *et al* 2003). Oxygen transport across the vessel wall is characterized by the permeability $L_{O_2} = 4.1 \times 10^{-4} \text{ m s}^{-1}$ calculated from a function of blood haematocrit fitted to simulated transport (Eggleton *et al* 2000). A median haematocrit of 0.19 was used, as measured in mammary adenocarcinomas in rats by Brizel *et al* (1993). The oxygen diffusion coefficient was set to $D_{O_2} = 2 \times 10^{-9} \text{ m}^2 \text{ s}^{-1}$ (Tannock 1972). This effective value incorporates tissue inhomogeneities, including cell membranes, intra- and extracellular components. The maximum oxygen consumption rate M_0 is known only vaguely. A mean value of 15 mmHg s^{-1} was used, as in the work of Daşu *et al* (2003). Generally the rate is proportional to the density of vital cells, which might vary within a tumour as well as for different tumour types. Published data for the Michaelis–Menten constant P_0 of the oxygen consumption vary strongly. One reason is that it is not a fixed parameter for any system, but is linearly related to the maximal rate of respiration M_0 (Schindler 1964). It was set to 2 mmHg,

in agreement with other investigators (Goldman 2008 Daşu *et al* 2003). The resulting median pO_2 of a typical vessel map simulated with the chosen parameters is 3.3 mmHg. This is small compared to the overall median pO_2 of 9 mmHg reported for head-and-neck tumours by Nordmark *et al* (2005), because more islands of low oxygen are resolved by the simulation compared to the low resolution measurements with polarographic electrodes.

Fmiso. The diffusional permeability coefficient L_T was set to $2.4 \times 10^{-6} \text{ m s}^{-1}$, as calculated by Kelly and Brady (2006). This value is prone to error, it may vary by two orders of magnitude for small molecules due to increased vessel fenestration in tumours (Jain 1987a). A diffusion coefficient of $D_T = 5.5 \times 10^{-11} \text{ m}^2 \text{ s}^{-1}$ measured for Misonidazole in multicellular membranes of V79 hamster cells by Cowan *et al* (1996) is considered applicable for Fmiso as well. The relationship between the tracer binding rate and O_2 tension $K(P)$ is determined by P_1 , P_2 and K_{\max} . Rasey *et al* (1989) found that 1000 to 2000 ppm O_2 inhibited binding by 50% compared to anoxia *in vitro* in different cell cultures. Hence, P_1 ranges from 0.8 to 1.5 mmHg. The remaining parameters could not be chosen based on published values. As it is not the purpose of this work to create predictive simulations that would be directly comparable to measurements, it seems to be legitimate to heuristically determine unknown parameters. K_{\max} was chosen such that the late slope of TAC is on the same order of magnitude as in clinical PET TACs, i.e. that tumour to blood ratios (T/B) are comparable. Parameter P_2 , defined as the O_2 tension at which the cell population is diminished by 50%, was determined by the simulated pO_2 at a distance of about $120 \mu\text{m}$ from vessels. This is a typical width of the vital cell layer around vessels (Thomlinson and Gray 1955, Tannock 1972). The parameter k was set to 0.3 to model a narrow transition zone between vital and necrotic tissue.

4. Results

The main characteristics of the simulated oxygen distribution are a sharp decrease with distance proximal to vessels and an asymptotic approach to 0 at large distances. These results corroborate with the findings of earlier investigations (Tannock 1972, Daşu *et al* 2003, Secomb *et al* 2004). Simulated tracer distributions 4 min, 3 min and 4 h after tracer injection are shown in figure 2. Shortly after injection the distribution is highly inhomogeneous; the concentration close to vessels is higher than that in distant regions (figure 2(b)). This results from the combination of slow purely diffusive tracer transport and large intervessel distances. No hypoxia-specific binding can be identified in the image. Hypoxic regions located between normoxic and necrotic tissue start to become discernible after about 30 min (figure 2(c)). Subsequently, the contrast of hypoxic regions against background gradually increases (figure 2(d)). A sufficiently high level of contrast is only reached several hours after tracer injection.

These observations also manifest in TACs from sub-regions with distinctive vascular fractions (VF) as shown in figure 3. Tissue perfusion strongly depends on VF. All simulated curves reproduce the typical phases in clinical PET TACs: a highly variable part in the first minutes, which is dominated by the freely diffusing tracer component, is followed by an almost linear uptake which is related to oxygen-dependent tracer binding. The shape of the early signal is strongly influenced by the VF and might thus be suitable to measure tissue perfusion. A lower VF results in higher tracer diffusion distances and, because the initial signal is dominated by free tracer, a less pronounced initial peak. Further, late signal slopes correspond to the VF in the chosen sub-regions, but it takes more than 1 h until the contrast

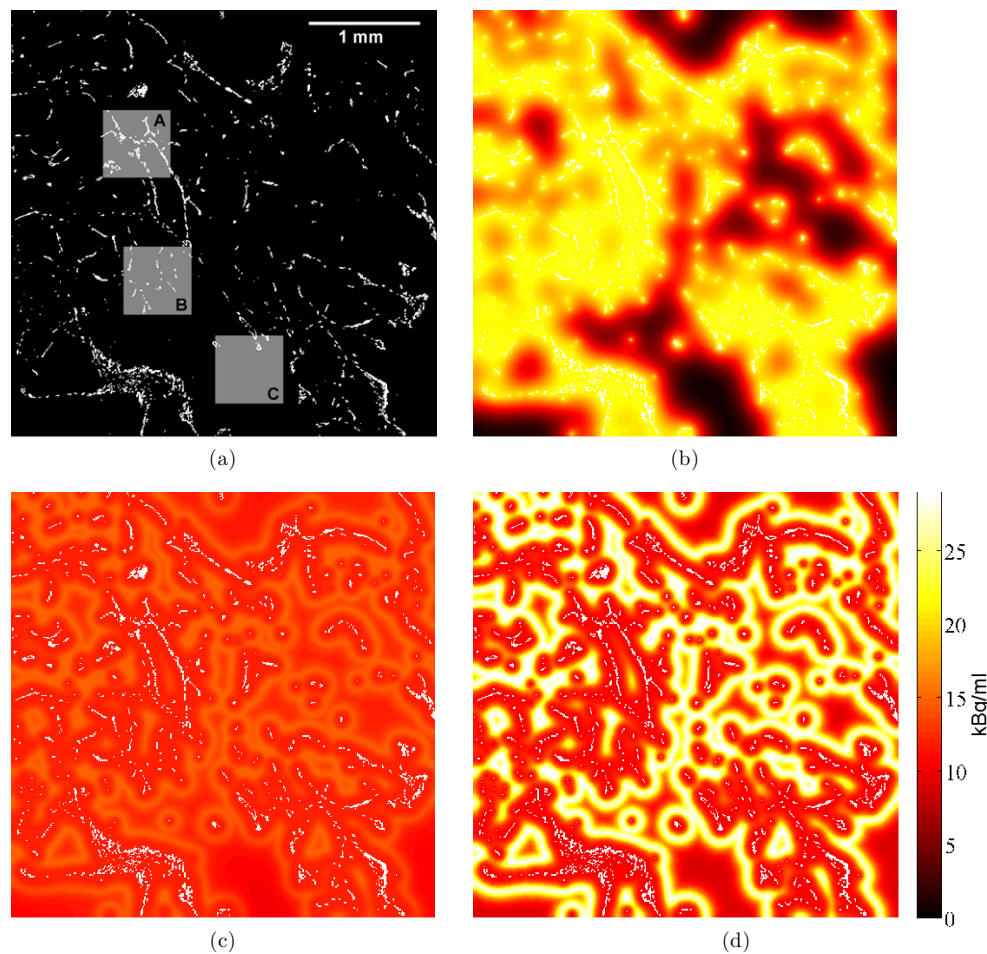


Figure 2. (a) Simulation vessel map with ROIs (vascular fractions A: 7.9%, B: 2.9%, C: 1.2%). Total (free + bound) tracer distributions on this map 4 min (b), 30 min (c) and 240 min (d) after tracer administration. Scale applies to all. Initially, the distribution is highly inhomogeneous as a result of slow tracer diffusion. Subsequently a hypoxia-specific contrast arises and gradually increases in layers between normoxic and necrotic tissue.

between region B (low late slope) and C (high late slope) is consistent with the late slopes, i.e. until the mean tracer density in C is higher than that in B.

To explore the complex formation process of Fmiso distributions, differences between TACs from two distinctively vascularized regions are shown in figure 4. A major advantage of the presented method is the possibility of separately analysing each component of a signal. There are three components: the mean densities of free and bound tracer in the extravascular space and the perfusive component, which is the contribution of tracer in the blood vessels in the respective tissue region. Two reasons for the described discrepancy between late signal slopes and contrast can be derived.

- (i) Initially, there is a large difference between free components. This leads to unbalanced binding that is higher in region B than in region C (Δbound), because the amount of

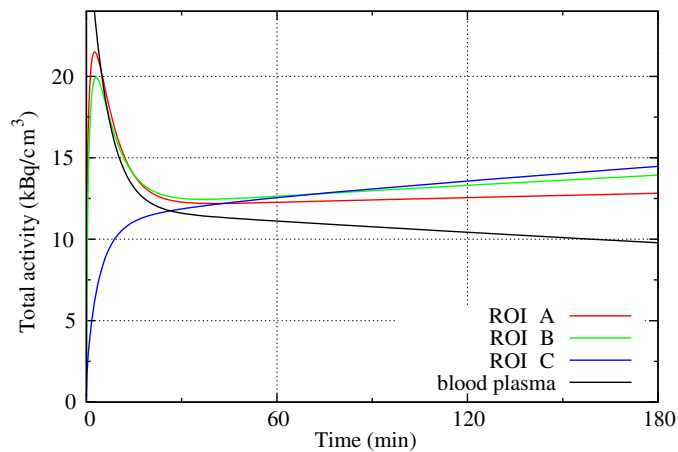


Figure 3. TACs from different ROIs in the simulated vessel map (Figure 2(a)). The initial signal shape depends on the respective VF (A: 7.9%, B: 2.9%, C: 1.2%). It takes more than 1 h until the curves of ROI C (higher late slope) and ROI B (lower slope) intersect.

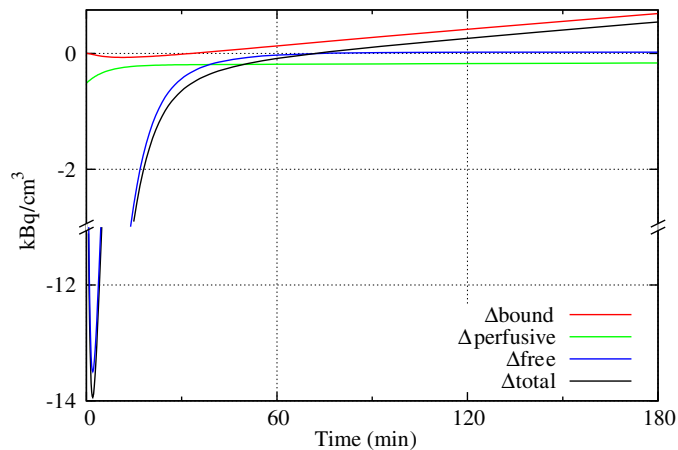


Figure 4. Signal component differences ROI C (low VF)—ROI B (intermediate VF). A large initial difference between free tracer signals (slow diffusion) leads to unspecific binding in the first minutes. In addition, the persistent difference between perfusive components has to be compensated before the total signal of ROI C becomes higher than that of ROI B and thus the contrast becomes representative (though not quantitatively) for the late signal slope. The late slope is strongly influenced by tracer binding and may thus be a measure of hypoxia.

bound tracer is proportional to free tracer concentrations. After about 30 min this effect is compensated.

- (ii) Still, the total signal difference remains negative, because the perfusive signal component is higher in region B exhibiting a higher VF than region C ($\Delta_{\text{perfusive}}$). An additional 30 min later this is compensated by tracer binding.

Eventually, TACs from regions B and C intersect more than 60 min after tracer administration and a contrast that corresponds to the late signal slope starts to evolve (figure 3).

However, a quantitatively stable contrast does not develop. It is noteworthy that in the presented case the free components have no influence on the time point of intersection.

Hypoxia tracers with transport and binding mechanisms similar to those of Fmiso were optimized for beneficial pharmacokinetic properties, such as a faster clearance from blood plasma while a high diffusibility is sustained (Mees *et al* 2009). We studied the theoretical impact of faster clearance by varying the clearance rate in the input plasma tracer concentration function by factors of 3 and 9. The resulting average increase in simulated T/B ratios 4 h after injection was 11% and 96%, respectively. However, absolute signals strongly decreased by 33% and 75%, respectively, which may impact the overall signal-to-noise level in PET imaging. For faster clearance less initial anti-specific binding was observed. Also, late tracer binding decreased because free tracer is almost completely cleared from tissue. These observations point towards an earlier optimum time point for static imaging compared to Fmiso. However, the simulations showed that, for quicker clearance, the free component is elevated in signals from sparsely vascularized regions, which limits the earliest feasible imaging time point.

5. Limitations of the method

The presented method is subject to a number of limitations. By employing two-dimensional vessel maps only radial molecular diffusion is incorporated, though considerable diffusion in the out of plane direction might occur in tissue. It might be feasible to extract three-dimensional maps from consecutive tissue sections, though this seems very challenging. When extracting simulation maps from microsections, erroneous vessel staining and resolution reduction might lead to false estimations of supply. No-flux boundary conditions imposed on the external boundary of simulation maps might result in false representations of the vessel density close to boundaries. As a consequence, sub-regions with different VFs were only taken from central areas of the vessel map. By calculating local tracer binding rates from static oxygenations, acute effects possibly influencing uptake are ignored. Tracer as well as oxygen concentration gradients along vessels are neglected; thus, a permeability limited supply is assumed. Irregular properties of tumour vasculature (e.g., elongated vessels, low vascular density) might lead to a slightly different situation. Parameter values of the model are generally prone to error and additional uncertainties are introduced by their different origins. Assumptions of homogeneous cell density and diffusion coefficients are limited by high tumour heterogeneity. In this study, results are not directly related to clinical PET signals, because PET characteristics such as a machine-specific point spread function, averaging over finite acquisition periods, image noise and reconstruction details, were not simulated. Still, the simulated TACs provide valuable information on the fundamental composition of real curves.

6. Discussion

We presented a method to simulate the dynamics of Fmiso on the microscopic scale incorporating all important processes for tracer distribution and uptake. Despite the limitations discussed in the previous section, the simulated local TACs share many characteristics with clinical PET TACs. Specifically, the high variability in the first hour which strongly depends on the local VF and the linear uptake later on. This suggests that the model is sensible. The results give evidence that it might be possible to measure perfusion from early dynamic Fmiso PET TACs. This potentially yields information on the time point of reoxygenation during RT and might help to identify hypoxic regions exhibiting low uptake.

Intersecting TAC were observed clinically (Eschmann *et al* 2005) and in preclinical tumour models (Busk *et al* 2009). This was confirmed by the simulated curves. The intersection of TACs may have fundamentally different reasons. Curves from regions exhibiting high (A) and intermediate (B) VFs intersect shortly after tracer administration (approximately 15 min). This is caused by faster distribution of free tracer in region (A) that quickly equilibrates with region (B). Curves from intermediately (B) to sparsely (C) vascularized regions intersect much later (1 to 2 h). In contrast to the first scenario, this is not driven by the free tracer component. Here, the late intersection is due to early unspecific binding and different weights of the perfusive components in the total signal. A possible practical implication is that, in order to identify hypoxia-related tracer binding, static Fmiso PET scans should be acquired as late as possible. Unspecific binding may be reduced by employing hypoxia tracers with higher diffusibilities, but the perfusive components are determined by the local vascular structure and cannot be influenced.

Quantification of images is necessary to incorporate Fmiso PET into RT by a DP by numbers approach (Thorwarth *et al* 2010). It is still an open question how to obtain stable parameters and how to translate them into a radiation dose by means of a suitable prescription function (Bentzen 2005, Bowen *et al* 2009). Our results indicate that using a single static image is prone to quantification error, because absolute intensities and more importantly also relative intensities between voxels strongly depend on the acquisition time point. Stability could be achieved by acquiring two subsequent images and thus directly measuring the late slope that is a combination of tracer uptake and clearance rate. Alternatively, kinetic model parameters fitted to dynamic Fmiso PET data could be employed, which was shown earlier to correlate with treatment outcome for head-and-neck cancer patients (Thorwarth *et al* 2005a).

7. Conclusion

Simulation of Fmiso dynamics using realistic microvessel maps based on tumour histology is feasible and may help to improve hypoxia PET acquisition protocols. Simulated spatiotemporal tracer distributions share many features with clinical PET TACs, suggesting that the current conception of the microscopic processes involved in the distribution and oxygen-dependent retention of Fmiso is adequate. Intersecting TACs from distinctively vascularized regions result from slow tracer diffusion and distinctive perfusion. Evidence was found that a measure of tissue perfusion might be derived from dynamic Fmiso PET scans. Furthermore, the simulations show that a single static Fmiso PET scan may not enable quantitative assessment of hypoxia because simulated intervoxel contrast is unstable.

Acknowledgments

This project was financially supported by the German Research Foundation (DFG), grant number AL 877/1-2 and by the European Social Fund and the Ministry of Science, Research and the Arts Baden-Württemberg.

References

- Alber M, Paulsen F, Eschmann S M and Machulla H J 2003 On biologically conformal boost dose optimization *Phys. Med. Biol.* **48** N31–5
- Bentzen S M 2005 Theragnostic imaging for radiation oncology: dose-painting by numbers *Lancet. Oncol.* **6** 112–7
- Boucher Y and Jain R K 1992 Microvascular pressure is the principal driving force for interstitial hypertension in solid tumors: implications for vascular collapse *Cancer Res.* **52** 5110–4

- Bowen S R, Flynn R T, Bentzen S M and Jeraj R 2009 On the sensitivity of IMRT dose optimization to the mathematical form of a biological imaging-based prescription function *Phys. Med. Biol.* **54** 1483–501
- Brizel D M, Klitzman B, Cook J M, Edwards J, Rosner G and Dewhirst M W 1993 A comparison of tumor and normal tissue microvascular hematocrits and red cell fluxes in a rat window chamber model *Int. J. Radiat. Oncol. Biol. Phys.* **25** 269–76
- Busk M, Horsman M R, Jakobsen S, Hansen K V, Bussink J, van der Kogel A and Overgaard J 2009 Can hypoxia-PET map hypoxic cell density heterogeneity accurately in an animal tumor model at a clinically obtainable image contrast? *Radiother. Oncol.* **92** 429–36
- Bussink J, Kaanders J H A M, Rijken P F J W, Raleigh J A and van der Kogel A J 2000 Changes in blood perfusion and hypoxia after irradiation of a human squamous cell carcinoma xenograft tumor line *Radiat. Res.* **153** 398–404
- Casciari J J, Graham M M and Rasey J S 1995 A modeling approach for quantifying tumor hypoxia with [F-18]fluoromisonidazole PET time-activity data *Med. Phys.* **22** 1127–39
- Chao K S *et al* 2001 A novel approach to overcome hypoxic tumor resistance: Cu-ATSM-guided intensity- modulated radiation therapy *Int. J. Radiat. Oncol. Biol. Phys.* **49** 1171–82
- Cowan D S M, Hicks K O and Wilson W R 1996 Multicellular membranes as an *in vitro* model for extravascular diffusion in tumours *Br. J. Cancer* **74** S28–31
- Dalah E, Bradley D and Nisbet A 2010 Simulation of tissue activity curves of ⁶⁴Cu-ATSM for sub-target volume delineation in radiotherapy *Phys. Med. Biol.* **55** 681–94
- Daşu A, Toma-Daşu I and Karlsson M 2003 Theoretical simulation of tumour oxygenation and results from acute and chronic hypoxia *Phys. Med. Biol.* **48** 2829–42
- Dehdashti D, Grigsby P W, Aintun M A, Lewis J S, Siegel B A and Welch M 2003 Assessing tumour hypoxia in cervical cancer by positron emission tomography with ⁶⁰Cu-ATSM: relationship to therapeutic response—a preliminary report *Int. J. Radiat. Oncol. Biol. Phys.* **55** 1233–8
- Dewhirst M W 1998 Concepts of oxygen transport at the microcirculatory level *Semin. Radiat. Oncol.* **8** 143–50
- Eggleton C D, Vadapalli A, Roy T K and Popel A S 2000 Calculations of intracapillary oxygen tension distributions in muscle *Math. Biosci.* **167** 123–43
- Eschmann S-M, Paulsen F, Reimold M, Dittmann H, Welz S, Reischl G, Machulla H-J and Bares R 2005 Prognostic impact of hypoxia imaging with ¹⁸F-Misonidazole PET in non-small cell lung cancer and head and neck cancer before radiotherapy *J. Nucl. Med.* **46** 253–60
- Goldman D 2008 Theoretical models of microvascular oxygen transport to tissue *Microcirculation* **15** 795–811
- Höckel M, Knoop C, Schlenger K, Vorndran B, Knapstein P G and Vaupel P 1993 Intratumoural pO₂ predicts survival in advanced cancer of the uterine cervix *Radiother. Oncol.* **26** 45–50
- Jain R K 1987a Transport of molecules across tumour vasculature *Cancer Metastasis. Rev.* **6** 559–93
- Jain R K 1987b Transport of molecules in the tumor interstitium: a review *Cancer Res.* **47** 3039–51
- Jain R K 1988 Determinants of tumor blood flow: a review *Cancer Res.* **48** 2641–58
- Kelly C J and Brady M 2006 A model to simulate tumour oxygenation and dynamic [18F]-Fmiso PET data *Phys. Med. Biol.* **51** 5859–73
- Koh W-J, Rasey J S, Evans M L, Grierson J R, Lewellen T K, Graham M M, Krohn K A and Griffin T W 1992 Imaging of hypoxia in human tumors with [F-18]fluoromisonidazole *Int. J. Radiat. Oncol. Biol. Phys.* **22** 199–212
- Komar G, Seppanen M, Eskola O, Lindholm P, Gronroos T J, Forsback S, Sipila H, Evans S M, Solin O and Minn H 2008 ¹⁸F-EF5: a new pet tracer for imaging hypoxia in head and neck cancer *J. Nucl. Med.* **49** 1944–51
- Ling C C, Humm J, Larson S, Amols H, Fuks Z, Leibel S and Koutcher J A 2000 Towards multidimensional radiotherapy (MD-CRT): biological imaging and biological conformality *Int. J. Radiat. Oncol. Biol. Phys.* **47** 551–60
- Ljungkvist A S E, Bussink J, Rijken P F J W, Kaanders J H A M, van der Kogel A J and Denekamp J 2002 Vascular architecture, hypoxia, and proliferation in first-generation xenografts of human head-and-neck squamous cell carcinomas *Int. J. Radiat. Oncol. Biol. Phys.* **54** 215–28
- Mahy P, Geets X, Lonneux M, Levque P, Christian N, De Bast M, Gillart J, Labar D, Lee J and Grgoire V 2008 Determination of tumour hypoxia with [18F]EF3 in patients with head and neck tumours: a phase I study to assess the tracer pharmacokinetics, biodistribution and metabolism *Eur. J. Nucl. Med. Mol. Imaging.* **35** 1282–9
- Mees G, Dierckx R, Vangestel C and Van de Wiele C 2009 Molecular imaging of hypoxia with radiolabelled agents *Eur. J. Nucl. Med. Mol. Imaging* **36** 1674–86
- Nordmark M *et al* 2005 Prognostic value of tumor oxygenation in 397 head and neck tumors after primary radiation therapy. an international multi-center study *Radiother. Oncol.* **77** 18–24
- Pierr M *et al* 2005 Hypoxia-specific tumor imaging with ¹⁸F-fluoroazomycin arabinoside *J. Nucl. Med.* **46** 106–13
- Pogue B W, O'Hara J A, Wilmot C M, Paulsen K D and Swartz H M 2001 Estimation of oxygen distribution in RIF-1 tumors by diffusion model-based interpretation of pimonidazole hypoxia and eppendorf measurements *Radiat. Res.* **155** 15–25

- Popel A S 1989 Theory of oxygen transport to tissue *Crit. Rev. Biomed. Eng.* **17** 257–321
- Rasey J S, Koh W J, Evans M L, Peterson L M, Lewellen T K, Graham M M and Krohn K A 1996 Quantifying regional hypoxia in human tumours with positron emission tomography of [¹⁸F]fluoromisonidazole: a pretherapy study of 37 patients *Int. J. Radiat. Oncol. Biol. Phys.* **36** 417–28
- Rasey J S, Koh W-J, Grierson J R, Grunbaum Z and Krohn K A 1989 Radiolabeled fluoromisonidazole as an imaging agent for tumor hypoxia *Int. J. Radiat. Oncol. Biol. Phys.* **17** 985–91
- Rijken P F, Bernsen H J, Peters J P, Hodgkiss R J, Raleigh J A and van der Kogel A J 2000 Spatial relationship between hypoxia and the (perfused) vascular network in a human glioma xenograft: a quantitative multi-parameter analysis *Int. J. Radiat. Oncol. Biol. Phys.* **48** 571–82
- Schindler F J 1964 Oxygen kinetics in the cytochrome oxidase-oxygen reaction *PhD Thesis* University of Pennsylvania
- Secomb T W, Hsu R, Park H. E Y and Dewhirst M W 2004 Green's function methods for analysis of oxygen delivery to tissues by microvascular networks *Ann. Biomed. Eng.* **32** 1519–29
- Souvatoglou M, Grosu A L, Röper B, Krause B J, Beck R, Reischl G, Picchio M, Machulla H-J, Wester H-J and Piert M 2007 Tumour hypoxia imaging with ¹⁸F-FAZA PET in head and neck cancer patients: a pilot study *Eur. J. Nucl. Med. Mol. Imaging* **34** 1566–75
- Søvik Å, Malinen E and Olsen D R 2009 Strategies for biologic image-guided dose escalation: a review *Int. J. Radiat. Oncol. Biol. Phys.* **73** 650–8
- Stohrer M, Boucher Y, Stangassinger M and Jain R K 2000 Oncotic pressure in solid tumors is elevated *Cancer Res.* **60** 4251–5
- Tannock I F 1972 Oxygen diffusion and the distribution of cellular radiosensitivity in tumours *Br. J. Radiol.* **45** 515–24
- Thomlinson R H and Gray L H 1955 The histological structure of some human lung cancers and the possible implications for radiotherapy *Br. J. Cancer.* **9** 539–49
- Thorwarth D, Eschmann S M, Paulsen F and Alber M 2005b A kinetic model for dynamic ¹⁸F-Fmiso PET data to analyse tumour hypoxia *Phys. Med. Biol.* **50** 2209–24
- Thorwarth D, Eschmann S M, Scheiderbauer J, Paulsen F and Alber M 2005a Kinetic analysis of dynamic ¹⁸F-fluoromisonidazole PET correlates with radiation treatment outcome in head-and-neck cancer *Bio. Med. Cent. Cancer* **5** 152–60
- Thorwarth D, Eschmann S M, Paulsen F and Alber M 2007 Hypoxia dose painting by numbers: a planning study *Int. J. Radiat. Oncol. Biol. Phys.* **68** 291–300
- Thorwarth D, Geets X and Paiusco M 2010 Physical radiotherapy treatment planning based on functional PET/CT data *Radiother. Oncol.* **96** 317–24
- Toma-Daşu I, Daşu A and Brahme A 2009 Dose prescription and optimisation based on tumour hypoxia *Acta. Oncol.* **48** 1181–92
- van Loon J *et al* 2010 PET imaging of hypoxia using [¹⁸F]HX4: a phase I trial *Eur. J. Nucl. Med. Mol. Imaging* **37** 1663–8
- Vaupel P 2004 Tumor microenvironmental physiology and its implication for radiation oncology *Semin. Radiat. Oncol.* **14** 198–206
- Wang W, Lee N Y, Georgi J-C, Narayanan M, Guillem J, Schoder H and Humm J L 2010 Pharmacokinetic analysis of hypoxia ¹⁸F-Fluoromisonidazole dynamic PET in head and neck cancer *J. Nucl. Med.* **51** 37–45
- Wang W *et al* 2009 Evaluation of a compartmental model for estimating tumor hypoxia via FMISO dynamic PET imaging *Phys. Med. Biol.* **54** 3083–99

B. Modelling and simulation of the influence of acute and chronic hypoxia on [¹⁸F]fluoromisonidazole PET imaging

published in

Physics in Medicine and Biology 2012, **57**: 1675–1684.

Modelling and simulation of the influence of acute and chronic hypoxia on [¹⁸F]fluoromisonidazole PET imaging

David Mönnich¹, Esther GC Troost², Johannes HAM Kaanders²,
Wim JG Oyen³, Markus Alber¹ and Daniela Thorwarth¹

¹ Section for Biomedical Physics, University Hospital for Radiation Oncology,
Hoppe-Seyler-Straße 3, 72076 Tübingen, Germany

² Institute of Oncology, Radiation Oncology, Radboud University Nijmegen Medical Centre,
PO Box 9101, 6500 HB Nijmegen, The Netherlands

³ Institute of Oncology, Nuclear Medicine, Radboud University Nijmegen Medical Centre,
PO Box 9101, 6500 HB Nijmegen, The Netherlands

E-mail: david.moennich@med.uni-tuebingen.de

Received 11 October 2011, in final form 11 January 2012

Published 7 March 2012

Online at stacks.iop.org/PMB/57/1675

Abstract

Tumour hypoxia can be assessed by positron emission tomography (PET) using radiotracers like [¹⁸F]fluoromisonidazole (Fmiso). The purpose of this work was to independently investigate the influence of chronic and acute hypoxia on the retention of Fmiso on the microscale. This was approached by modelling and simulating tissue oxygenation and Fmiso dynamics on the microscale based on tumour histology. Diffusion of oxygen and Fmiso molecules in tissue- and oxygen-dependent Fmiso binding were included in the model. Moreover, a model of fluctuating vascular oxygen tension was incorporated to theoretically predict the effects of acute hypoxia. Simulated tissue oxygen tensions (PO₂) are strongly influenced by the modelled periodical fluctuations (period 40 min, total amplitude 10 mmHg and mean 35 mmHg). Fluctuations led to variations in mean PO₂ of up to 41% and in the hypoxic fraction (PO₂ < 5 mmHg) from 56% up to 65%. Significant Fmiso retention is caused by chronic (87%) as well as acute hypoxia (13%). By simulating Fmiso injection during different phases of the vascular PO₂ fluctuation cycle, it was found that acute hypoxia of an empirically valid magnitude does not influence the reproducibility of PET imaging. Thus, it may be impossible to separate acute and chronic hypoxia from serial PET images.

(Some figures may appear in colour only in the online journal)

1. Introduction

Hypoxia is a frequent trait of human tumours and negatively affects radiotherapy outcome (Höckel *et al* 1993, Nordmark *et al* 2005, Vaupel 2004). It can be categorized into chronic

and acute (or intermittent) hypoxia. While chronic hypoxia is a static phenomenon which is primarily caused by large intervessel distances, acute hypoxia is highly dynamic and is characterized by fluctuating tissue oxygen tension (PO_2) (Bayer *et al* 2011). As a consequence, acutely hypoxic cells can be located closer to vessels than cells suffering from chronic hypoxia. Hypoxia can be clinically assessed by positron emission tomography (PET) imaging using radiotracers such as [^{18}F]fluoromisonidazole (Fmiso) (Mees *et al* 2009). Integrating hypoxia PET imaging into radiotherapy treatment planning might improve treatment efficacy (Søvik *et al* 2009, Nestle *et al* 2009, Thorwarth *et al* 2010).

Fluctuating tissue PO_2 was directly measured in preclinical tumour models with polarographic electrodes and optical methods (Dewhirst *et al* 1998, Brurberg *et al* 2004). Indirect methods evaluating a mismatch between sequentially administered markers also yielded evidence for acute hypoxia (Chaplin *et al* 1987, Bennewith and Durand 2004). Early studies often attributed acute hypoxia to a total stasis of blood flow in vessels (Brown 1979). This view shifted towards a more gradual understanding of acute hypoxia by demonstrations of the predominance of varying red blood cell flux (RCF) over flow stasis in preclinical tumour models (Durand and Aquino-Parsons 2001, Lanzen *et al* 2006, Cárdenas-Navia *et al* 2008). Fluctuating perfusion was also found in different clinical tumours (Pigott *et al* 1996). Few studies combined direct measurements of (single-point) tissue PO_2 timelines and RCF (Kimura *et al* 1996, Lanzen *et al* 2006), in many cases, revealing a correlation between flux fluctuations and variations in tissue PO_2 . More evidence on the induction of intermittent tissue hypoxia by fluctuating RCF was obtained from theoretical simulations of O_2 transport (Kimura *et al* 1996). In a similar way, a model of vascular PO_2 fluctuations was used by Cárdenas-Navia *et al* (2007) to theoretically predict the efficacy of the hypoxic cytotoxin tirapazamine with respect to acute hypoxia.

In a clinical Fmiso PET imaging study, Nehmeh *et al* (2008) reported a variability in spatial uptake between repeat scans. Assuming that this variability is associated with acute hypoxia, Wang *et al* (2009) developed a model to separate out acute from chronic hypoxia. In a preclinical study, Maftai *et al* (2011a) found no correlation between the proportion of acute hypoxia predicted by this model and that assessed in tumour microsections.

In this work, fluctuating O_2 supply is linked to the resulting tissue O_2 distribution with high spatial resolution. To achieve this, a theoretical model of varying vascular PO_2 has been integrated in a simulation tool to predict the tissue oxygenation for a given 2D vascular configuration. Moreover, with this tool the distribution and oxygen-dependent binding of Fmiso can be simulated with high spatial and temporal resolution. Theoretical predictions are a valuable tool for this application, because time-resolved measurements of microscopic O_2 and tracer distributions are not yet technically feasible. A further objective is to investigate the influence of acute hypoxia on Fmiso retention and the potential to distinguish between retention from chronic and acute hypoxia in serial (or single dynamic) clinical PET scans. This is an important issue for the correct interpretation of hypoxia PET data and its potential use for an individualization of radiotherapy in terms of dose painting.

2. Methods and materials

2.1. Modelling and simulation of tissue oxygenation and Fmiso dynamics

Modelling and simulation of Fmiso diffusion and binding has been implemented in multiple steps, as described in detail before (Mönnich *et al* 2011). Fundamental parameter values used in this study have been adopted from this publication. The major steps of the simulation process and their respective input and output are outlined in figure 1. Briefly, spatial oxygen

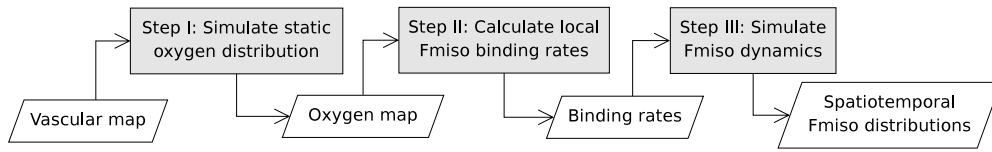


Figure 1. Spatiotemporal Fmiso distributions are simulated in three steps. A steady-state oxygen map is simulated on a histology-derived vessel map (step I). This serves as input for the calculation of local PO_2 -dependent Fmiso binding rates (step II). These first-order reaction rates are the input for the simulation of Fmiso dynamics (step III).

tension distributions are simulated on 2D vessel maps that are derived from images of the vasculature in preclinical tumour tissue microsections. Details on histological procedures have been published elsewhere (Bussink *et al* 2000, Rijken *et al* 2000). Tissue oxygenation is modelled by a reaction–diffusion equation (Daşu *et al* 2003) using a Michaelis–Menten relationship between tissue oxygen tension P_t and consumption rate $M(P_t)$:

$$\frac{\partial P_t}{\partial t} = D_{O_2} \cdot \nabla^2 P_t - M(P_t),$$

with D_{O_2} as the oxygen diffusion coefficient. A reduced cellular oxygen demand, when supply is limited, is reproduced by M . In a consecutive step, local Fmiso binding rates $K(P_t)$ are calculated as a function of local oxygen tensions, also considering the density of vital cells. Finally, diffusion and binding of Fmiso in the extravascular space is simulated with high spatial and temporal resolution. The underlying coupled diffusion–reaction model linking concentrations of freely diffusing C_f and bound C_b tracer (Kelly and Brady 2006):

$$\begin{aligned} \frac{\partial C_f}{\partial t} &= D_T \cdot \nabla^2 C_f - K(P_t) \cdot C_f \\ \frac{\partial C_b}{\partial t} &= K(P_t) \cdot C_f, \end{aligned}$$

where D_T denotes the Fmiso diffusion coefficient.

As a consequence of acute hypoxia in tumour tissue, Fmiso binding rates can vary with time. In contrast, the assumption of a stable Fmiso supply does not induce substantial errors in the simulations, because the supply is limited by the tracer plasma concentration for the first minutes after bolus injection only, i.e. before an equilibrium free tracer concentration has been established in tissue.

2.2. Modelling fluctuating vascular oxygen tension

To simulate the influence of acute hypoxia on Fmiso retention, the calculation of steady-state oxygen distributions (step I, figure 1) has been extended by an explicitly time-dependent blood oxygen tension $P = P(t)$. It was assumed that P fluctuates sinusoidally with an amplitude P_A , a period T and a phase ϕ around a mean value \bar{P} :

$$P(t) = \bar{P} + P_A \sin(2\pi t/T + \phi). \quad (1)$$

This is a simplification of a broad range of fluctuation types observed in preclinical tumour models. Nonetheless, a number of published timelines clearly exhibit harmonic behaviour (Cárdenas-Navia *et al* 2008, Brurberg *et al* 2004). The cellular oxygen consumption rate is a function of supply, it is almost constant at high tissue oxygen levels and decreases if supply is limited. Cells are not able to fully adapt metabolism to oxygen fluctuations above a certain frequency. Thus, the continuous fluctuations described by equation (1) are discretized into constant steps (figure 2(b)). In each consecutively numbered step, i a static tissue oxygen

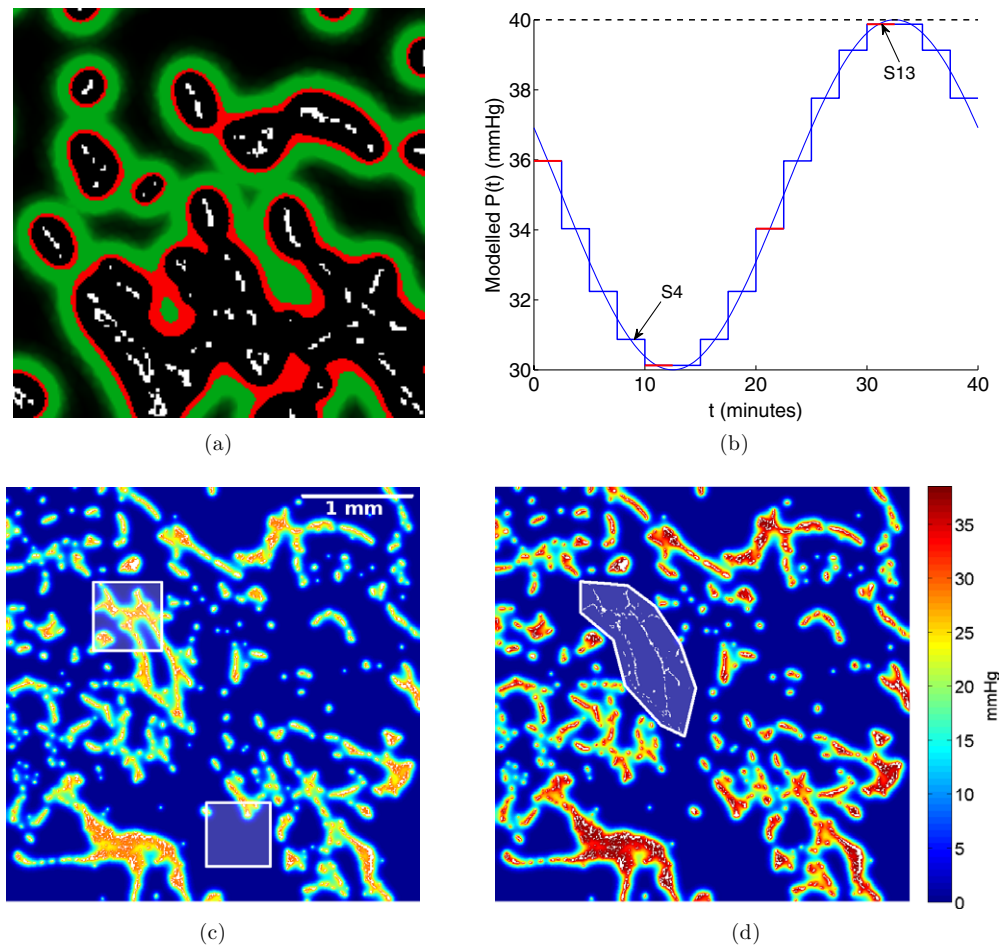


Figure 2. (a) In a subregion of the simulation map, oxygen levels fluctuate around 5 mmHg in acutely hypoxic regions (red) while remaining below this threshold in chronically hypoxic regions (green). Vessels are white. (b) Continuous periodical fluctuations of vascular PO_2 with a period of 40 min ($P(t)$, equation 1) are discretized into 2.5 min wide steps of constant PO_2 (P_i , $i = 1, \dots, 16$). Red: steps including supply collapse. Dashed line: baseline PO_2 level (chronic hypoxia). (c/d): Resulting tissue oxygenations during step 4 (c) and 13 (d). In step 13, oxygen supply from the highlighted group of vessels has stalled. Two subregions with vascular fractions distinct from the total map are highlighted in (c).

distribution is calculated based on the corresponding discretized intravascular P_i . In this study, a step width of 2.5 min and a fluctuation period of 40 min (cf section 2.3) translate to $i = 1, \dots, 16$. It was further assumed that acute hypoxia does not interfere with cell viability. In a separate scenario, total supply collapse within a manually selected group of vessels is added to continuous fluctuations.

2.3. Simulation parameters

The choice of parameter values for the fluctuation model is based on preclinical timelines of intravascular PO_2 reported by Cárdenas-Navia *et al* (2008). Dominating fluctuations showed periods in the order of tens of minutes. Total amplitudes as high as 10 mmHg were commonly observed. In order to assess the potential magnitude of the effects from acute hypoxia, a

total amplitude of 10 mmHg ($P_A = 5$ mmHg) and a period $T = 40$ min was chosen for the simulations. These values may vary among tumour types, sites and volumes. As a consequence, an empirically unvalidated value $T = 4$ h was included in this study to estimate an upper boundary of the effect that crucially depends on the fluctuation period. A mean value of $\bar{P} = 35$ mmHg was used, so that a maximum plasma PO_2 of $P_A + \bar{P} = 40$ mmHg during cycling yields the baseline chronic oxygenation. Reported fluctuations were not strictly synchronous among vessels in a 6 mm^2 region. However, in this study variations were assumed to be temporally coordinated in a $4.2 \times 4.2 \text{ mm}^2$ vessel map, as small vascular networks are probably cycling together (Dewhirst *et al* 2008). Transient flow collapse or plasma flow (absence of RCF) affects 5%–17% of repeatedly the same vessels for short periods (Dewhirst 1998, Maftai *et al* 2011b). No data have been published yet on the frequency of supply collapse. For simulation purposes, a region comprising 13% of the vascular space in the simulation map was manually selected (figure 2(d)) in which supply collapse for 2.5 min with a frequency of 6 h^{-1} was modelled.

2.4. Data evaluation

The mean PO_2 in the tissue region selected for this simulation was calculated for each fluctuation step to determine the corresponding tissue hypoxia. Moreover, PO_2 histograms were generated for all steps to evaluate changes in PO_2 statistics caused by acute hypoxia. The proportion of Fmiso retention caused by acute hypoxia was calculated relative to the reference uptake for a constant plasma PO_2 of 40 mmHg. Furthermore, Fmiso time activity curves (TACs) were generated by integrating tracer concentrations over the whole area of the vessel map. The maximum difference between TACs for different underlying PO_2 fluctuation phases was determined for timepoints later than 2 h after tracer injection (p.i.). This allows us to assess whether Fmiso PET imaging is sensitive to the PO_2 fluctuation phase in which the tracer bolus is injected, i.e. whether acute hypoxia can cause differential uptake in serial PET scans as proposed by Nehmeh *et al* (2008). As hardware-specific properties of PET imaging and 3D characteristics of the vascular bed are not included in the simulation of TACs, these are not directly comparable to clinical voxel-wise PET TACs. Nonetheless, the simulated activity distributions form a plausible microscopic ground truth for a real PET signal.

3. Results

3.1. Influence of fluctuating vascular PO_2 on tissue oxygenation

Resulting oxygen distributions for two different fluctuation steps are shown in figure 2. In figure 2(c), oxygen supply is low (step 4, $P_4 \approx 31$ mmHg). In this step, tissue PO_2 is considerably lower than that in the high supply step 13 depicted in figure 2(d) ($P_{13} \approx 40$ mmHg), even though step 13 includes supply collapse in the depicted region. The mean tissue PO_2 for the two distributions is 5.7 mmHg (S4) and 7.3 mmHg (S13), respectively. A still larger mean tissue PO_2 of 8.2 mmHg results from step 14, which does not include supply collapse. Generally, the modelled fluctuations in plasma PO_2 influence mean tissue PO_2 directly (figure 3(a)). The maximum observed variation between steps 5 and 14 is 3.4 mmHg (w/ collapse, dots, figure 3(a)) and 2.7 mmHg (w/o collapse, boxes). Figure 3(b) shows a histogram of oxygen tensions for all steps during the 40 min fluctuation period. Apparently, the population of states with oxygen tensions between 0 and 5 mmHg strongly depends on the fluctuation step. In contrast, intermediately oxygenated states are influenced to a much lower extent. The acutely hypoxic fraction (aHF) can be defined as the proportion

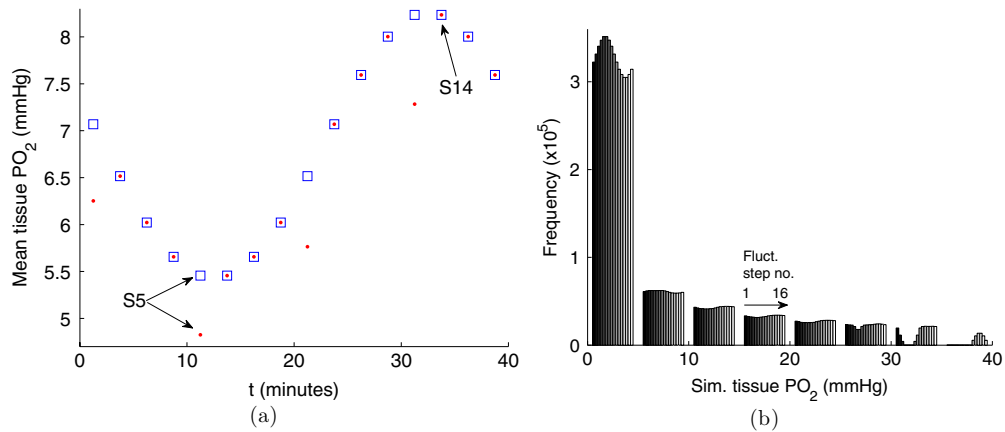


Figure 3. (a) Mean tissue PO_2 of the simulation map for each fluctuation step (cf figure 2(b)). Boxes: w/o supply collapse. Dots: w/ collapse with a frequency of 6 h^{-1} . (b) Histogram of simulated tissue PO_2 for fluctuation steps 1 to 16 (black to grey). Oxygenation states between 0 and 5 mmHg are primarily affected by acute hypoxia.

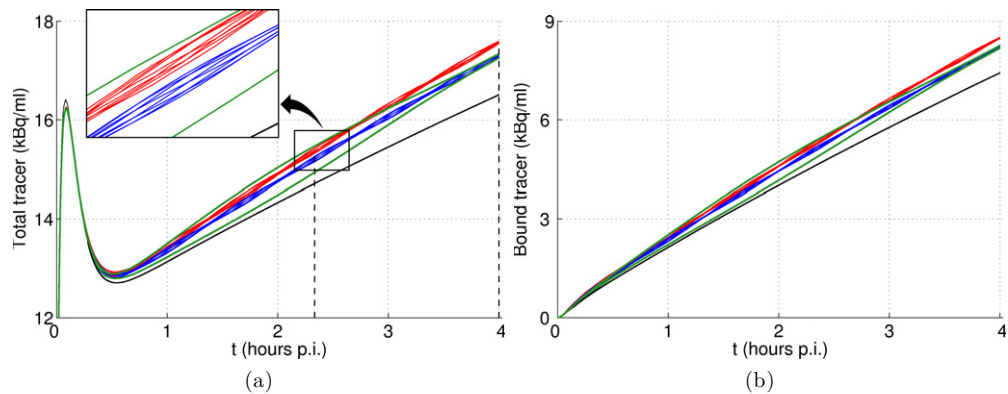


Figure 4. (a) Simulated Fmiso TACs for a constant vascular PO_2 of 40 mmHg (black) and for a PO_2 fluctuating with an amplitude of 5 mmHg around a mean value of 35 mmHg w/o (blue) and w/ supply collapse (red) in selected vessels. Eight different fluctuation phases ϕ from 0 to $7\pi/4$ were used in each set of curves to assess the variability of the curves depending on the timepoint of tracer injection. In addition, a period of 4 h was simulated w/o collapse for $\phi = 0, \pi$ (green). (b) Influence of acute hypoxia on the isolated bound tracer component.

of tissue area in which oxygen levels fluctuate across a 5 mmHg threshold (figure 2(a)). In the presented example, the aHF amounts to 9% (w/ collapse) and 12% (w/o collapse). Chronic hypoxia prevails, with 56% of the simulated tissue area invariably remaining below the threshold.

3.2. Influence of acute hypoxia on Fmiso distributions

The influence of acute hypoxia on simulated Fmiso retention is depicted in figure 4. TACs for the vessel map in figure 2 were simulated for three scenarios: stable supply with the maximum vascular PO_2 of 40 mmHg (baseline) and fluctuating supply with and without collapse. Compared to baseline conditions, fluctuations alone affect tracer retention more strongly than the additional phases of supply collapse. Isolated analysis of the bound Fmiso

component (figure 4(b)) reveals that in the combined case a maximum of 13.0% of Fmiso retention can be attributed to acute hypoxia. As a part of this, a fraction of 3.5% arises from supply collapse. This fraction rises to 33% in an extreme scenario with supply collapse in 69% of the vessels. Relative to the total tracer concentration, which consists of tracer in blood plasma, freely diffusing in tissue and bound in hypoxic regions, the influence is smaller. Depending on the timepoint p.i. 4.1% (2 h), 5.4% (3 h) and 6.2% (4 h) of the total tracer concentration results from acute hypoxia.

In order to investigate the reproducibility of Fmiso PET imaging, simulations with eight different PO_2 fluctuation phases were performed (variation of ϕ in equation 1 between 0 and $7\pi/4$). Each single curve in figure 4 corresponds to the injection of Fmiso in a different phase of the modelled harmonic PO_2 fluctuations, comparable to a test/retest experiment in a clinical setting. The maximum variability of the total Fmiso signal including supply collapse was 0.7% (140 min p.i.), while at 4 h p.i. it was 0.3%. These values are specified relative to the mean at each timepoint. The same analysis was carried out for subregions in the simulation map that exhibit distinct vascular densities from the total map (figure 2(c)). The maximum variability between TACs in a poorly and a well-vascularized subregion was 0.3% and 2.2%, respectively. For hypothetical fluctuations with $T = 4$ h (w/o collapse), a maximum difference of 3.8% for the total map was found, which may be still larger in subregions. Averaging over a 15 min interval, which is representative for a typical late PET acquisition time, does not reduce the given variabilities.

4. Discussion

Acute hypoxia is characterized by oxygen supply fluctuations that directly induce variations in mean tissue PO_2 and lead to considerable redistribution towards worse oxygenated states. All cells experience cycling oxygenation, though in chronically hypoxic regions the absolute effect is lower. This may increase the magnitude of hypoxia-related adverse effects on treatment of human cancers and add temporal variability. The results of this simulation framework show that chronic hypoxia prevails over acute hypoxia for the specific vessel map used, which agrees with results from categorizing microvascular supply units in immunohistochemically stained squamous cell carcinoma xenograft sections (Maftei *et al* 2011b). This particular vessel map was chosen, because it comprises a well-balanced combination of subregions with distinct vascular patterns, in contrast to most other available tissue sections of the same family.

In the presented example, additional Fmiso retention predominantly originates from periodical fluctuations rather than supply collapse. Significant Fmiso retention arises from both acute and chronic hypoxia. In the presented simulations, an acutely hypoxic fraction of 12% accounts for 13% of the total tracer retention, indicating that in special cases there may be a direct match between the abundance of hypoxia types and the retention associated with each type. This result strongly depends on the choice of the model, parameter values and vessel map. Generally, acute hypoxia may result in an amount of Fmiso retention that is detectable by PET. However, it is not evident that this component can be separated from the total signal due to the inherent combination of both acutely and chronically hypoxic tissue areas in a PET voxel. There are fundamental limitations to the potential to detect acute hypoxia by a single dynamic PET examination. Rapid fluctuations will be obliterated by the inertia of cells to adapt to alternating O_2 supply and also cannot be sampled by slow PET imaging. Slow fluctuations with periods much larger than the duration of the examination will induce equally slow uptake changes that may also not be detectable by PET.

As Fmiso binding is approximately irreversible (Casciari *et al* 1995), the amount of retained Fmiso is a surrogate of the integral hypoxia during the tracer uptake time. Thus, it

is intelligible that acute hypoxia with periods smaller than the uptake time may not strongly affect Fmiso PET reproducibility. Our results support this notion, as different timepoints of tracer administration were simulated by varying the phase of the PO₂ fluctuation. Resulting variations in tissue Fmiso concentrations were smaller than 2.2% for fluctuation parameters based on published values. A wide range of potential microvascular distributions in a PET voxel was incorporated in the analysis by also considering subregions in the simulation map with vascular patterns distinct from the total map. A variation of the observed magnitude may not influence the interpretation of Fmiso PET, which is subject to much larger uncertainties, such as statistical noise. Asynchronous (out of phase) plasma PO₂ fluctuations among vessels potentially further reduce this variability in (pre-)clinical tumours.

Only extremely slow fluctuations with periods in the order of the tracer uptake time (~4 h p.i.) might compromise reproducibility and thus render acute hypoxia observable by PET imaging. For hypothetical fluctuations with $T = 4$ h a maximum signal difference of 3.8% was found, indicating a rising influence on Fmiso PET imaging compared to simulations based on empirical parameter values. This ambiguity remains, as it is unknown if such slow changes in tumour oxygenation occur periodically in (pre-)clinical tumours or if they are dominated by irreversible structural remodelling that should be attributed to evolving chronic hypoxia. This has to be clarified by future research to determine the precursor of differential Fmiso uptake in serial clinical Fmiso PET scans observed by Nehmeh *et al* (2008).

Our results have a number of implications for the integration of Fmiso PET data into radiotherapy treatment planning (RTP). First, the reproducibility of Fmiso retention in a voxel seems largely unaffected by acute hypoxia originating from supply collapse and PO₂ fluctuations with periods below 4 h and a total magnitude of 10 mmHg. This is a prerequisite for consistent PET-based RTP, as this work suggests that there is no method to separate chronic and acute hypoxia in Fmiso PET images for a broad range of microvascular beds and supply fluctuation patterns. Moreover, it is a promising result that the composite PET signal shows substantial uptake from both hypoxia types and therefore no type is generally neglected in RTP using this data. Although, it might be necessary to find ways to assess both types separately, if it holds true that they have different biological consequences. It has been suggested that acute hypoxia may induce increased radioresistance and stimulate transfer of cells to a more malignant phenotype, while chronically hypoxic cells have a limited survival time (Janssen *et al* 2005, Bristow and Hill 2008).

5. Conclusion

A mathematical model of transport and oxygen-dependent binding of the hypoxia PET tracer [¹⁸F]fluoromisonidazole (Fmiso) was extended in order to theoretically investigate the interplay of acute and chronic hypoxia and its influence on Fmiso retention in histology-derived microscopic tumour vessel maps. Simulations show that modelled fluctuations in vascular oxygen content considerably reduce tissue oxygenation, still underlying chronic hypoxia prevails. Acute effects cause an amount of Fmiso retention detectable by PET. However, simulations with empirical fluctuation properties do not suggest a potential to distinguish between uptake from chronic and acute effects in serial clinical PET scans.

Acknowledgments

DT is supported by the European Social Fund and the Ministry of Science, Research and the Arts Baden–Württemberg.

References

- Bayer C, Shi K, Astner S, Maftai C-A and Vaupel P 2011 Acute versus chronic hypoxia: why a simplified classification is simply not enough *Int. J. Radiat. Oncol. Biol. Phys.* **80** 965–8
- Bennewith K L and Durand R E 2004 Quantifying transient hypoxia in human tumor xenografts by flow cytometry *Cancer Res.* **64** 6183–9
- Bristow R G and Hill R P 2008 Hypoxia and metabolism: Hypoxia, DNA repair and genetic instability *Nature Rev. Cancer* **8** 180–92
- Brown J M 1979 Evidence for acutely hypoxic cells in mouse tumours, and a possible mechanism of reoxygenation *Br. J. Radiol.* **52** 650–6
- Brurberg K G, Graff B A, Olsen D R and Rofstad E K 2004 Tumor-line specific PO₂ fluctuations in human melanoma xenografts *Int. J. Radiat. Oncol. Biol. Phys.* **58** 403–9
- Bussink J, Kaanders J H A M, Rijken P F J W, Raleigh J A and van der Kogel A J 2000 Changes in blood perfusion and hypoxia after irradiation of a human squamous cell carcinoma xenograft tumor line *Radiat. Res.* **153** 398–404
- Cárdenas-Navia L I, Mace D, Richardson R A, Wilson D F, Shan S and Dewhirst M W 2008 The pervasive presence of fluctuating oxygenation in tumors *Cancer Res.* **68** 5812–9
- Cárdenas-Navia L I, Secomb T W and Dewhirst M W 2007 Effects of fluctuating oxygenation on tirapazamine efficacy: theoretical predictions *Int. J. Radiat. Oncol. Biol. Phys.* **67** 581–6
- Casciari J J, Graham M M and Rasey J S 1995 A modeling approach for quantifying tumor hypoxia with [F-18]fluoromisonidazole PET time-activity data *Med. Phys.* **22** 1127–39
- Chaplin D J, Olive P L and Durand R E 1987 Intermittent blood flow in a murine tumor: radiobiological effects *Cancer Res.* **47** 597–601
- Daşu A, Toma-Daşu I and Karlsson M 2003 Theoretical simulation of tumour oxygenation and results from acute and chronic hypoxia *Phys. Med. Biol.* **48** 2829–42
- Dewhirst M W 1998 Concepts of oxygen transport at the microcirculatory level *Semin. Radiat. Oncol.* **8** 143–50
- Dewhirst M W, Braun R D and Lanzen J L 1998 Temporal changes in PO₂ of R3230Ac tumors in fischer-344 rats *Int. J. Radiat. Oncol. Biol. Phys.* **42** 723–6
- Dewhirst M W, Cao Y and Moeller B 2008 Cycling hypoxia and free radicals regulate angiogenesis and radiotherapy response *Nature Rev. Cancer* **8** 425–37
- Durand R E and Aquino-Parsons C 2001 Clinical relevance of intermittent tumour blood flow *Acta Oncol.* **40** 929–36
- Höckel M, Knoop C, Schlenger K, Vorndran B, Knapstein P G and Vaupel P 1993 Intratumoural PO₂ predicts survival in advanced cancer of the uterine cervix *Radiother. Oncol.* **26** 45–50
- Janssen H L, Haustermans K M, Balm A J and Begg A C 2005 Hypoxia in head and neck cancer: how much, how important? *Head Neck* **27** 622–38
- Kelly C J and Brady M 2006 A model to simulate tumour oxygenation and dynamic [18F]-Fmiso PET data *Phys. Med. Biol.* **51** 5859–73
- Kimura H, Braun R D, Ong E T, Hsu R, Secomb T W, Papahadjopoulos D, Hong K and Dewhirst M W 1996 Fluctuations in red cell flux in tumor microvessels can lead to transient hypoxia and reoxygenation in tumor parenchyma *Cancer Res.* **56** 5522–8
- Lanzen J, Braun R D, Klitzman B, Brizel D, Secomb T W and Dewhirst M W 2006 Direct demonstration of instabilities in oxygen concentrations within the extravascular compartment of an experimental tumor *Cancer Res.* **66** 2219–23
- Maftai C-A, Bayer C, Shi K, Astner S and Vaupel P 2011b Quantitative assessment of hypoxia subtypes in microcirculatory supply units of malignant tumors using (immuno-)fluorescence techniques *Strahlenther. Onkol.* **187** 260–6
- Maftai C-A, Shi K, Bayer C, Astner S and Vaupel P 2011a Comparison of (immuno-)fluorescence data with serial [18F]Fmiso PET/CT imaging for assessment of chronic and acute hypoxia in head and neck cancers *Radiother. Oncol.* **99** 412–7
- Mees G, Dierckx R, Vangestel C and Van de Wiele C 2009 Molecular imaging of hypoxia with radiolabelled agents *Eur. J. Nucl. Med. Mol. Imaging* **36** 1674–86
- Mönnich D, Troost E G C, Kaanders J H A M, Oyen W J G, Alber M and Thorwarth D 2011 Modelling and simulation of [18F]fluoromisonidazole dynamics based on histology-derived microvessel maps *Phys. Med. Biol.* **56** 2045–57
- Nehmeh S A *et al* 2008 Reproducibility of intratumor distribution of 18F-Fluoromisonidazole in head and neck cancer *Int. J. Radiat. Oncol. Biol. Phys.* **70** 235–42
- Nestle U, Weber W, Hentschel M and Grosu A L 2009 Biological imaging in radiation therapy: role of positron emission tomography *Phys. Med. Biol.* **54** R1–25

- Nordsmark M *et al* 2005 Prognostic value of tumor oxygenation in 397 head and neck tumors after primary radiation therapy. An international multi-center study *Radiother. Oncol.* **77** 18–24
- Pigott K, Hill S, Chaplin D and Saunders M 1996 Microregional fluctuations in perfusion within human tumours detected using laser Doppler flowmetry *Radiother. Oncol.* **40** 45–50
- Rijken P F, Bernsen H J, Peters J P, Hodgkiss R J, Raleigh J A and van der Kogel A J 2000 Spatial relationship between hypoxia and the (perfused) vascular network in a human glioma xenograft: a quantitative multi-parameter analysis *Int. J. Radiat. Oncol. Biol. Phys.* **48** 571–82
- Søvik Å, Malinen E and Olsen D R 2009 Strategies for biologic image-guided dose escalation: a review *Int. J. Radiat. Oncol. Biol. Phys.* **73** 650–8
- Thorwarth D, Geets X and Pausco M 2010 Physical radiotherapy treatment planning based on functional PET/CT data *Radiother. Oncol.* **96** 317–24
- Vaupel P 2004 Tumor microenvironmental physiology and its implication for radiation oncology *Semin. Radiat. Oncol.* **14** 198–206
- Wang K, Yorke E, Nehmeh S A, Humm J L and Ling C C 2009 Modeling acute and chronic hypoxia using serial images of [18F]-FMISO PET *Med. Phys.* **36** 4400–8

C. Correlation between tumor oxygenation and ^{18}F -Fluoromisonidazole PET data simulated based on microvasculature images

publication pending

Correlation between tumor oxygenation and 18F-Fluoromisonidazole PET data simulated based on microvasculature images

David Mönnich^{1*}, Dipl. Phys., Esther G C Troost², M.D., Ph.D., Johannes H A M Kaanders³, M.D., Ph.D., Wim J G Oyen⁴, M.D., Ph.D., Markus Alber⁵, Ph.D., Daniel Zips⁶, M.D., Ph.D., Daniela Thorwarth¹, Ph.D.

¹ Section for Biomedical Physics, Department of Radiation Oncology, University Hospital Tübingen, Tübingen, Germany

² Department of Radiation Oncology (MAASTRO), GROW School for Oncology and Developmental Biology, Maastricht University Medical Center, Maastricht, The Netherlands

³ Institute of Oncology, Radiation Oncology, Radboud University Nijmegen Medical Centre, Nijmegen, The Netherlands

⁴ Institute of Oncology, Nuclear Medicine, Radboud University Nijmegen Medical Centre, Nijmegen, The Netherlands

⁵ Department of Oncology, Aarhus University Hospital, Aarhus, Denmark

⁶ Department of Radiation Oncology, University Hospital Tübingen, Tübingen, Germany

* Corresponding author

Address: David Mönnich, Section for Biomedical Physics, Department of Radiation Oncology, Hoppe-Seyler-Str. 3, 72076 Tübingen, Germany

E-mail address: david.moennich@med.uni-tuebingen.de (D. Mönnich)

Phone: +49 (0)70712986064

Fax: +40 (0)7071295920

Short running title: Correlation between tumor oxygenation and FMISO PET data

Acknowledgments: This project was financially supported by the German Research Foundation (DFG), grant no. TH 1528/1-1 and by the European Social Fund and the Ministry of Science, Research and the Arts Baden-Württemberg.

Conflict of Interest: None.

Abstract

Purpose

Tumor hypoxia is associated with poor outcome after radiotherapy. It can be assessed by positron emission tomography (PET) using the hypoxia tracer ^{18}F -Fluoromisonidazole (FMISO). It was investigated, which aspects of the local tumor oxygenation are actually assessed using different FMISO-PET protocols. We hypothesize that two PET scans at different timepoints after tracer injection (p.i.) yield a measure for the mean oxygen partial pressure (PO_2) in a voxel.

Methods and Materials

Microscopic tissue oxygenations and FMISO diffusion-retention dynamics were computationally simulated. Tumor vessel maps, derived from head-and-neck tumor xenograft histology, model the transport of molecules into and out of tissue. Different O_2 and FMISO parameters were evaluated for 300 distinct $2 \times 2 \text{ mm}^2$ vessel configurations: O_2 parameters were the vital hypoxic fraction (vHF) and the mean PO_2 . FMISO-PET parameters were the voxel signal four hours p.i. ($F_{4\text{h}}$) and the ratio between $F_{4\text{h}}$ and signal 0–15 min p.i. ($F_{\text{H/P}}$). Interpreting each vessel configuration as a PET voxel, correlations between O_2 and FMISO parameters were evaluated. A receiver operating characteristic (ROC) analysis was performed, regarding the identification of voxels with mean $\text{PO}_2 < 2.5 \text{ mmHg}$ using $F_{4\text{h}}$ or $F_{\text{H/P}}$. It was also performed for critical microscopic PO_2 values without averaging.

Results

In hypoxic tissue $F_{4\text{h}}$ is well correlated with vHF ($R^2=0.90$), while its correlation with mean PO_2 is low ($R^2=0.22$). A high correlation was found between $F_{\text{H/P}}$ and mean PO_2 ($R^2=0.99$). The ROC analysis showed that hypoxic regions can be identified based on $F_{\text{H/P}}$ with a higher diagnostic accuracy ($\text{YI}=\text{sensitivity}+\text{specificity}-1=0.94$), than based on $F_{4\text{h}}$ alone ($\text{YI}=0.68$). Both FMISO parameters identify critical microscopic PO_2 values with moderate effectiveness ($\text{YI}=0.63$ and 0.60 , respectively).

Conclusions

Compared to a single late FMISO-PET scan alone, incorporating a second scan, acquired during the tracer wash-in phase, yields a more accurate measure for the mean voxel PO_2 . The single-scan alone appears suitable to estimate the vHF.

1 Introduction

Tumor hypoxia reduces the effectiveness of radiotherapy (RT). Clinical studies have shown that therapy response correlates with local tumor oxygen concentrations (PO_2) measured with polarographic oxygen probes (1). A prognosis of RT outcome is also possible by non-invasive positron emission tomography (PET) imaging using hypoxia tracers such as ^{18}F -Fluoromisonidazole (FMISO) and $^{60/64}\text{Cu}$ -diacetyl-bis(N4-methylthiosemicarbazone) (Cu-ATSM) (2–4). These results prompted concepts to improve RT efficacy by adapting dose prescriptions to the local degree of hypoxia that was assessed using PET imaging (5). Reliable local prescriptions for a specific tumor might require more elaborate imaging protocols, compared to a simple overall prognosis of RT outcome (6).

Hypoxia in tumor tissue is very heterogeneously distributed on the microscopic length-scale and often interspersed with necrotic regions. Moreover, FMISO is retained in vital cells only. Thus, the limited PET resolution restricts the detection of small hypoxic regions embedded in necrotic or normoxic tissue (7, 8). Consequently, any information about microscopic tissue properties inferred from hypoxia PET data, e.g. the oxygenation, is associated with uncertainties. This might explain reports of low to moderate correlations between direct PO_2 measurements using invasive oxygen probes and hypoxia PET data in clinical (9, 10) as well as preclinical settings (11–13).

The aim of this study was to investigate, which FMISO PET imaging protocol might deliver a reliable surrogate for the local loss of cell kill that is caused by hypoxia. This loss, frequently characterized by the oxygen enhancement ratio (OER), is closely linked to the PO_2 in cells. Cell kill strongly decreases below PO_2 values of 10 mmHg (14). Therefore, an FMISO PET imaging parameter that correlates with the local PO_2 might also effectively identify radioresistance.

Here, two different voxel-based FMISO parameters were considered, which can be obtained by one

or two PET scans at different timepoints after injection (p.i.). The correlation between these parameters and the underlying PO_2 was analyzed for different histology-derived microvessel architectures. The analysis was based on computational simulations of (a) the static tissue oxygenation and subsequently (b) the full FMISO diffusion-retention dynamics (15).

2 Methods and Materials

2.1 Tissue microsections and tumor microvessel maps

Vessel maps were derived from tumor tissue histology. As described earlier (16), frozen tissue sections from human SCCHN xenograft tumor lines were immunohistochemically (IHC) stained for endothelial structures with 9F1 (rat monoclonal to mouse endothelium). Subsequently, the sections were scanned using a digital image analysis system, resulting in gray-scale images of the fluorescent signal. In this study, five images of different tumors with a total area of 133 mm^2 converted into binary vessel maps. Tissue images were chosen from a large amount of data, so that vessel patterns varied strongly among the maps, ranging from very dense to sparse and inhomogeneous distributions. The maps were used to model the flow of O_2 and FMISO molecules into and out of tissue. Within the maps, 300 sub-regions with dimensions of $2 \times 2 \text{ mm}^2$ were placed at random locations. In these sub-regions, the O_2 and FMISO parameters were calculated from the simulated data.

2.2 Modeling and simulation of O_2 and FMISO

A tool to perform computer simulations of the FMISO diffusion-retention dynamics in multiple steps was used in this study. Its basic working principle is schematically shown in fig. 1. The applied diffusion-reaction equations, simulation method and parameter values were described in detail earlier (15). Briefly, equilibrium oxygen partial pressure (PO_2) distributions are calculated for a given vessel map. The applied model accounts for the supply of oxygen across capillary membranes, its distribution in tissue and its consumption by tumor cells. A Michaelis-Menten relationship describes the decreasing oxygen consumption with a decreasing amount of offered oxygen (17). Subsequently, the PO_2 distributions are used to calculate local FMISO binding rates. Binding rates are modeled to increase with decreasing PO_2 , up to a sharp drop at very low PO_2 . This drop accounts for cell death under extreme oxygen and glucose deprivation. It also considers that FMISO is reduced in vital cells only. These assumptions agree qualitatively with pimonidazole IHC in xenografts of human squamous cell carcinomas of the head-and-neck (SCCHN) (18). Finally, applying the PO_2 -dependent local binding rates, FMISO supply, diffusion and retention are simulated in the same vessel map as the PO_2 . By integrating the simulated FMISO concentrations in a specific sub-region, pseudo-PET voxel signals can be derived at different timepoints (p.i.). Relating these signals to the blood tracer concentration yields tumor-to-blood (T:B) ratios.

2.3 Simulated macroscopic O_2 and FMISO parameters

In each sub-region (a) the mean oxygen partial pressure (mean PO_2) and (b) the vital hypoxic fraction (vHF) were calculated. The vHF was defined as the fraction of microscopic PO_2 values (micro PO_2) that are smaller than 2.5 mmHg. The fraction of necrotic cells was mathematically excluded. Consequently, the vHF is low in largely necrotic regions, which typically show a very low mean PO_2 . In contrast, the HF, which is frequently assessed using oxygen probes, includes vital and necrotic tissue areas alike.

The two simulated FMISO parameters calculated in each sub-region were: (a) the mean FMISO concentration four hours p.i., $F_{4h}=c(t=4h \text{ p.i.})$ and (b) the ratio between F_{4h} and the mean concentration 0—15 min p.i., $F_{H/P}=c(t=4h \text{ p.i.}) / \overline{c(t)_{0-15\text{min}}}$. The second parameter can be interpreted as a measure of hypoxia-related tracer retention that is normalized to a simple measure of perfusion (6). In this way, a largely necrotic region, which retains small amounts of FMISO, can nonetheless be correctly identified as hypoxic, as it is typically poorly perfused as well.

2.4 Correlations between oxygenation and FMISO PET

Scatter plots of meanPO₂ and vHF against F_{4h} as well as F_{H/P} were created. Further, a correlation analysis was performed. Coefficients of determination R² were calculated in a linear sense (Pearson coefficient) and from nonlinear fits.

Binary hypoxia maps (meanPO₂<2.5 mmHg) were created by applying different thresholds to both simulated FMISO parameters. In ROC curves, true positive rates (sensitivities) were plotted *versus* false positives rates (1-specificities). Along the curves the applied thresholds decrease. The area under the curves (AUC) and the Youden index (YI=sensitivity+specificity-1) were calculated as quality measures. Their values may range from 0.5 to 1 and 0 to 1 (futile to ideal), respectively. In a further step, the ROC analysis was also used to evaluate how well the hypoxia maps characterize the microPO₂. In this case, each component of an FMISO hypoxia map represents a 60×60 matrix of underlying PO₂ values.

3 Results

3.1 Simulated oxygenations

Full simulations were performed for all vessel maps. An example for a simulated equilibrium PO₂ distribution and the corresponding static FMISO pattern four hours p.i. is shown in fig. 2. The median microPO₂ value of all maps was 10.0 mmHg (0.0 mmHg–40.0 mmHg), calculated with a resolution comparable to that of polarographic probes (~50 μm/pixel). Histograms of the microPO₂ within four selected sub-regions show distinct oxygenation patterns (fig. 3).

The simulated sub-regional meanPO₂ values ranged from 1.3 mmHg to 32.5 mmHg with a median of 11.0 mmHg. The median simulated vHF was 26% (0%–48%), while the median HF was 34% (0%–87%). In fig. 4 the simulated vHF and HF are plotted against meanPO₂. For meanPO₂ values above 17 mmHg vHF and HF overlap, which indicates that necrosis plays a minor role in this value range. However, for lower values vHF and HF differ greatly. In hypoxic regions with meanPO₂<10 mmHg the relationship between vHF and meanPO₂ appears ambiguous, while apparently there is a linear relation between HF and meanPO₂. Due to this relation, the HF was abandoned in favor of the meanPO₂ in the further analysis, as the latter is not based on an arbitrary threshold value.

3.2 Correlations between oxygenation and FMISO PET

In fig. 5a scatter plots of vHF and meanPO₂ *versus* F_{4h} are shown. Each point represents a data pair from a specific sub-region. A high overall linear correlation coefficient R² of 0.99 and 0.95 for vHF and meanPO₂, respectively, was observed. These values reduce to 0.90 and 0.22, respectively, when the analysis is restricted to data pairs in the hypoxic range (i.e. meanPO₂<10 mmHg and vHF>0.24). A high diagnostic accuracy is especially important in this range. Consequently, F_{4h} is a reliable surrogate measure for the vHF, but it does not enable an accurate prediction of the meanPO₂.

Plots of vHF and meanPO₂ against the second FMISO parameter, F_{H/P}, are shown in fig. 5b. Both plots display a nonlinear relationship. By visual inspection the meanPO₂ appears better defined than the vHF, markedly in the hypoxic range. This was corroborated by fitting a function of the form $f(x)=p_1/(p_2+x)^{p_3}+p_4$ to the meanPO₂ and vHF curves (fit coefficients p_i). The resulting coefficients of determination R² for vHF and meanPO₂ were 0.97 and 0.99 for the overall data, respectively and 0.54 and 0.99 when the fit was restricted to the hypoxic range, respectively. This suggests that F_{H/P} is a more accurate surrogate for the meanPO₂ than F_{4h}.

3.3 ROC analysis

The ROC analysis of the simulated diagnostic accuracies of the two FMISO parameters to identify hypoxia is shown in fig. 6. Clearly, regions with critical meanPO₂ values are discriminated extremely well by F_{H/P} (AUC=0.95, optimum YI=0.94), while F_{4h} alone is much less reliable (AUC=0.88, YI=0.68). Note, that for very high thresholds applied to F_{4h} the false positive rate is

higher than the true positive rate. The optimum threshold values were $F_{H/P}=1.61$ and $F_{4h}=16.3$ kBq/ml (T:B=1.8).

The ROC analysis of the feasibility to identify microscopic hypoxia (microPO₂) resulted in AUC (optimum YI) coefficients of 0.88 (0.63) and 0.86 (0.60) for $F_{H/P}$ and F_{4h} , respectively. These values are almost identical to those for identifying the macroscopic meanPO₂ by F_{4h} , though much lower than for evaluating meanPO₂ by $F_{H/P}$. Here, the optimum threshold values were $F_{H/P}=1.0$ and $F_{4h}=15.5$ kBq/ml (T:B=1.7).

4 Discussion

The results of this study outline the fundamental problems associated with imaging microscopic tumor hypoxia using PET, which is a macroscopic imaging modality. In addition to the partial volume effect, the ambiguous binding behavior of the FMISO molecule is problematic. That is, its low accumulation in well oxygenated as well as predominantly necrotic tissue. Necrosis is closely related to the progress of hypoxia (18). These intrinsic limitations might render static FMISO PET signals poor surrogates for meanPO₂ and, as a consequence, also for the local radiosensitivity. The advantages of the employed simulation method, compared to experimental approaches using oxygen electrodes, are the very high spatial as well as temporal resolutions. Moreover, it is possible to quantitatively compare PO₂ and FMISO distributions for identical vessel microstructures.

The combined statistics of the PO₂ distributions simulated here showed a median PO₂ value of 10.0 mmHg. In clinical SCCHN the median PO₂, assessed in different institutions, ranged from 5 mmHg to 18 mmHg (1). This makes it plausible that the manifold oxygenations in SCCHN were adequately represented by the simulations. Note, that this study is specific to SCCHN, as the employed histological material was limited to this entity.

The high correlation between F_{4h} and vHF indicates that the vHF in a voxel can be assessed by an FMISO PET scan 4 h p.i. A similar result was reported for the relationship between FAZA autoradiography and the vital hypoxic fraction evaluated using pimonidazole IHC (7). In contrast, the meanPO₂ is not as easily accessible. A reliable evaluation of the meanPO₂ requires adding information from a second PET scan during the tracer wash-in phase. This argument is supported by a small study reporting a correlation between kinetic analysis of dynamic FMISO PET data and local control in RT of head-and-neck cancer (6). The results of the ROC analysis correspond with the different degrees of correlation, i.e. the two-scan parameter being more accurate.

Quantitative aspects of the presented results must be interpreted carefully. In a clinical setting, the diagnostic accuracies presumably are substantially lower than estimated here. There is a number of reasons for this. For instance, resolutions achievable in clinical PET are lower than the edge-length of 2 mm of the simulated sub-regions. Moreover, the full temporal and spatial heterogeneity of tumor tissue oxygenations might not be covered entirely by the histological data and the model used in the simulations. Also, simple averaging over sub-regions is not fully realistic, as real PET signals are convolved with a more complex point spread function. Furthermore, image noise was neglected in this study and simulations were performed in 2D.

This study does not cover the development of hypoxia and FMISO PET signals after RT initiation. It was proposed that optimum timepoints for static imaging might lie weeks into the course of therapy (3, 19). A possible explanation is that reoxygenation occurs during RT. It is possible that the independent tracer wash-in signals make information about the reoxygenation potential of a tissue region available ahead of the start of therapy (20).

Despite all limitations, the general tendency probably persists that two-scan FMISO PET imaging yields a more reliable surrogate for the mean PO₂ than a single scan. The results of this study will be validated based on clinical data, comprising dynamic FMISO PET scans or the two static scans proposed here. In combination with the assessment of RT outcome data, an analysis of the locations of potential tumor recurrences would be ideal to evaluate the different parameters proposed here. An advantage of the two-scan method is its simple clinical implementation, compared to the more intricate kinetic analysis of dynamic data. Standard static scan routines can be used, followed by co-

registration of the image volumes and a simple parameter evaluation.

Another future line of research is to further investigate the hypothesis supported by this work, that low perfusion/necrosis and high perfusion/mild hypoxia can only be distinguished with multiple or dynamic FMISO PET scans. This can be performed by taking targeted biopsies from patients following FMISO PET scanning and evaluate necrosis and hypoxia.

5 Conclusion

In this study, tissue oxygenations and FMISO diffusion-retention dynamics were computationally simulated based on histology-derived tumor microvessel networks. The results indicate a potential advantage of using the independent information of two FMISO PET scans to accurately assess the local mean partial oxygen pressure (PO_2) in head-and-neck tumors, compared to a single scan. The first scan covers the tracer wash-in phase, while the second scan is acquired following a tracer uptake phase of a few hours. This might be important to effectively adapt radiotherapy dose prescriptions according to the local degree of tumor hypoxia.

References

1. Nordmark M, Bentzen SM, Rudat V, *et al.* Prognostic value of tumor oxygenation in 397 head and neck tumors after primary radiation therapy. An international multi-center study. *Radiother Oncol.* 2005;77:18–24.
2. Dehdashti F, Grigsby PW, Lewis JS, *et al.* Assessing tumor hypoxia in cervical cancer by PET with ^{60}Cu -labeled diacetyl-bis(N4-methylthiosemicarbazone). *J Nucl Med.* 2008;49:201–205.
3. Zips D, Zöphel K, Abolmaali N, *et al.* Exploratory prospective trial of hypoxia-specific PET imaging during radiochemotherapy in patients with locally advanced head-and-neck cancer. *Radiother Oncol.* 2012.
4. Mortensen LS, Johansen J, Kallehauge J, *et al.* FAZA PET/CT hypoxia imaging in patients with squamous cell carcinoma of the head and neck treated with radiotherapy: Results from the DAHANCA 24 trial. *Radiother Oncol.* 2012.
5. Ling CC, Humm J, Larson S, *et al.* Towards multidimensional radiotherapy (MD-CRT): biological imaging and biological conformality. *Int J Radiat Oncol Biol Phys.* 2000;47:551–560.
6. Thorwarth D, Eschmann S-M, Scheiderbauer J, *et al.* Kinetic analysis of dynamic ^{18}F -fluoromisonidazole PET correlates with radiation treatment outcome in head-and-neck cancer. *BMC Cancer.* 2005;5:152.
7. Busk M, Horsman MR, Jakobsen S, *et al.* Can hypoxia-PET map hypoxic cell density heterogeneity accurately in an animal tumor model at a clinically obtainable image contrast? *Radiother Oncol.* 2009;92:429–436.
8. Christian N, Lee JA, Bol A, *et al.* The limitation of PET imaging for biological adaptive-IMRT assessed in animal models. *Radiother Oncol.* 2009;91:101–106.
9. Bentzen L, Keiding S, Nordmark M, *et al.* Tumour oxygenation assessed by ^{18}F -fluoromisonidazole PET and polarographic needle electrodes in human soft tissue tumours. *Radiother Oncol.* 2003;67:339–344.
10. Mortensen LS, Buus S, Nordmark M, *et al.* Identifying hypoxia in human tumors: A correlation study between ^{18}F -FMISO PET and the Eppendorf oxygen-sensitive electrode. *Acta Oncol.* 2010;49:934–940.

11. O'Donoghue JA, Zanzonico P, Pugachev A, *et al.* Assessment of regional tumor hypoxia using 18F-fluoromisonidazole and 64Cu(II)-diacetyl-bis(N4-methylthiosemicarbazone) positron emission tomography: Comparative study featuring microPET imaging, Po2 probe measurement, autoradiography, and fluorescent microscopy in the R3327-AT and FaDu rat tumor models. *Int J Radiat Oncol Biol Phys.* 2005;61:1493–1502.
12. Sørensen M, Horsman MR, Cumming P, *et al.* Effect of intratumoral heterogeneity in oxygenation status on FMISO PET, autoradiography, and electrode Po2 measurements in murine tumors. *Int J Radiat Oncol Biol Phys.* 2005;62:854–861.
13. Bartlett RM, Beattie BJ, Naryanan M, *et al.* Image-Guided Po2 Probe Measurements Correlated with Parametric Images Derived from 18F-Fluoromisonidazole Small-Animal PET Data in Rats. *J Nucl Med.* 2012.
14. Bristow RG, Hill RP. Hypoxia and metabolism: Hypoxia, DNA repair and genetic instability. *Nat Rev Cancer.* 2008;8:180–192.
15. Mönnich D, Troost EGC, Kaanders JHAM, *et al.* Modelling and simulation of [18F]fluoromisonidazole dynamics based on histology-derived microvessel maps. *Phys Med Biol.* 2011;56:2045–2057.
16. Bussink J, Kaanders JHAM, Rijken PFJW, *et al.* Changes in Blood Perfusion and Hypoxia after Irradiation of a Human Squamous Cell Carcinoma Xenograft Tumor Line. *Radiat Res.* 2000;153:398–404.
17. Casciari JJ, Sotirchos SV, Sutherland RM. Variations in tumor cell growth rates and metabolism with oxygen concentration, glucose concentration, and extracellular pH. *J Cell Physiol.* 1992;151:386–394.
18. Ljungkvist ASE, Bussink J, Kaanders JHAM, *et al.* Hypoxic cell turnover in different solid tumor lines. *Int J Radiat Oncol Biol Phys.* 2005;62:1157–1168.
19. Eschmann SM, Paulsen F, Bedeshem C, *et al.* Hypoxia-imaging with 18F-Misonidazole and PET: Changes of kinetics during radiotherapy of head-and-neck cancer. *Radiother Oncol.* 2007;83:406–410.
20. Thorwarth D, Eschmann S-M, Paulsen F, *et al.* A Model of Reoxygenation Dynamics of Head-And-Neck Tumors Based on Serial 18F-Fluoromisonidazole Positron Emission Tomography Investigations. *Int J Radiat Oncol Biol Phys.* 2007;68:515–521.

Figures

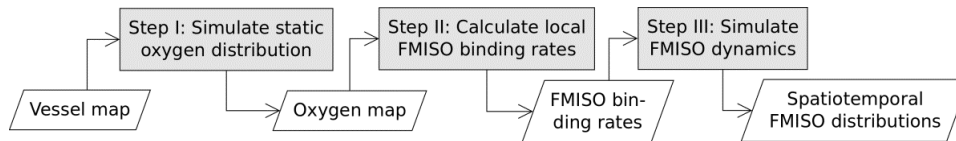


Figure 1: Multi-step simulation of tissue oxygenation and FMISO dynamics. I. A steady-state oxygen map is simulated in a histology-derived vessel map. II. This serves as input for the calculation of local PO_2 -dependent FMISO binding rates. III. These rates are the input for the simulation of FMISO diffusion and retention.

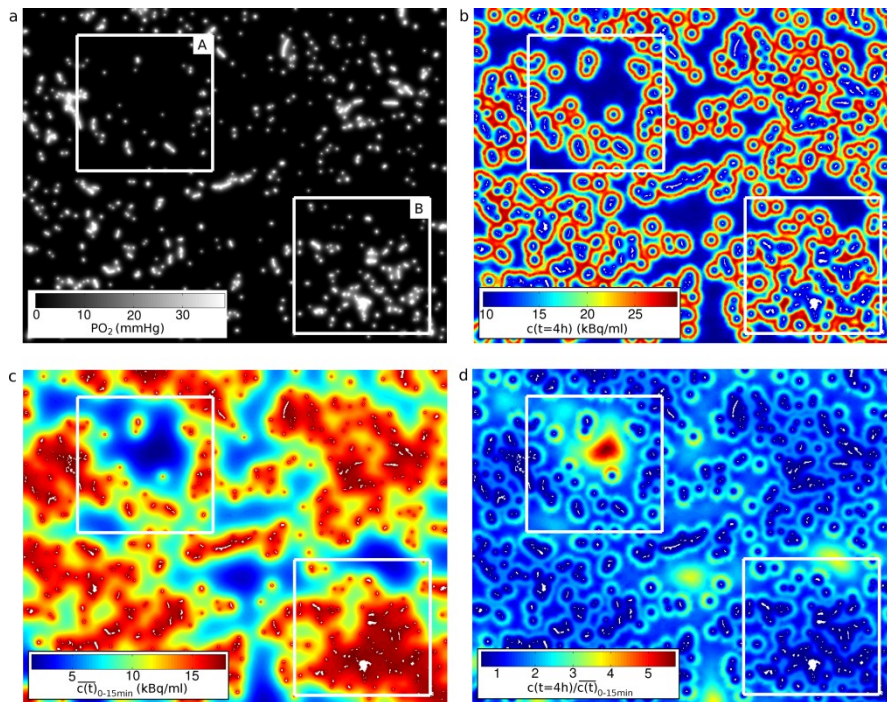


Figure 2: (a) Equilibrium PO_2 distribution for a $6.3 \times 4.9 \text{ mm}^2$ vessel map including two randomly placed $2 \times 2 \text{ mm}^2$ sub-regions (A, B). (b) Corresponding distribution of FMISO four hours p.i. Sub-regional averaging yields F_{4h} . Note the increasing retention with decreasing PO_2 until it is diminished by necrosis. Vessels are white. (c) Averaged early FMISO signal. (d) Ratio between the distributions shown in (b) and (c), yielding $F_{H/P}$. The mean PO_2 in sub-regions A and B is 1.7 mmHg and 4.3 mmHg, respectively. The single-scan FMISO signal F_{4h} is lower in A (16.2 kBq/ml) than in B (17.7 kBq/ml), giving contradicting results. A consistent metric is given by the two-scan value $F_{H/P}$, which is higher in A (1.82) than in B (1.35).

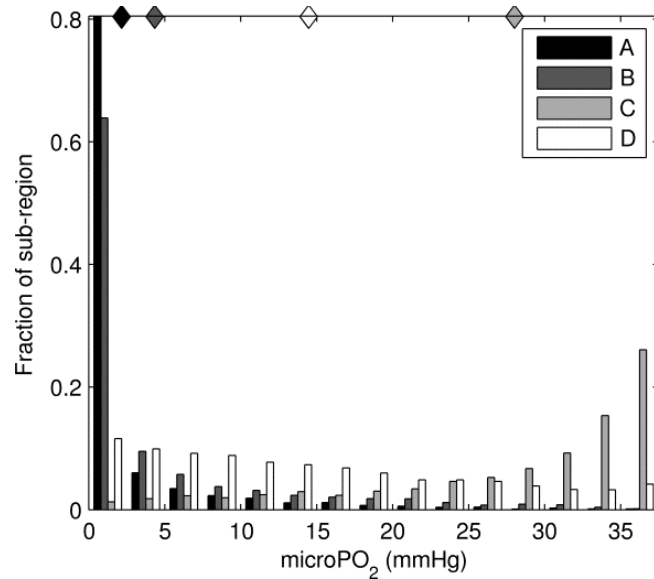


Figure 3: Histogram of the simulated microPO₂ values in 2×2 mm² sub-regions. Regions A and B are depicted in fig. 2, C and D are not shown. Respective meanPO₂ values are marked on the top axis.

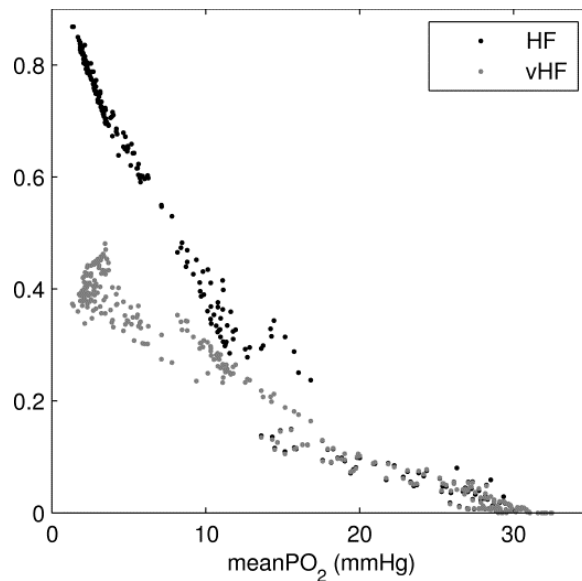


Figure 4: Scatter plots of vHF and HF against meanPO₂. Each point represents mean simulated data in a 2×2 mm² sub-region. Necrosis does not induce a difference between vHF and HF for meanPO₂>17 mmHg. For lower values excluding the necrotic sub-population from the vHF causes large differences. In hypoxic areas (meanPO₂<10 mmHg) the HF correlates well with the meanPO₂, while there are large discrepancies between meanPO₂ and vHF.

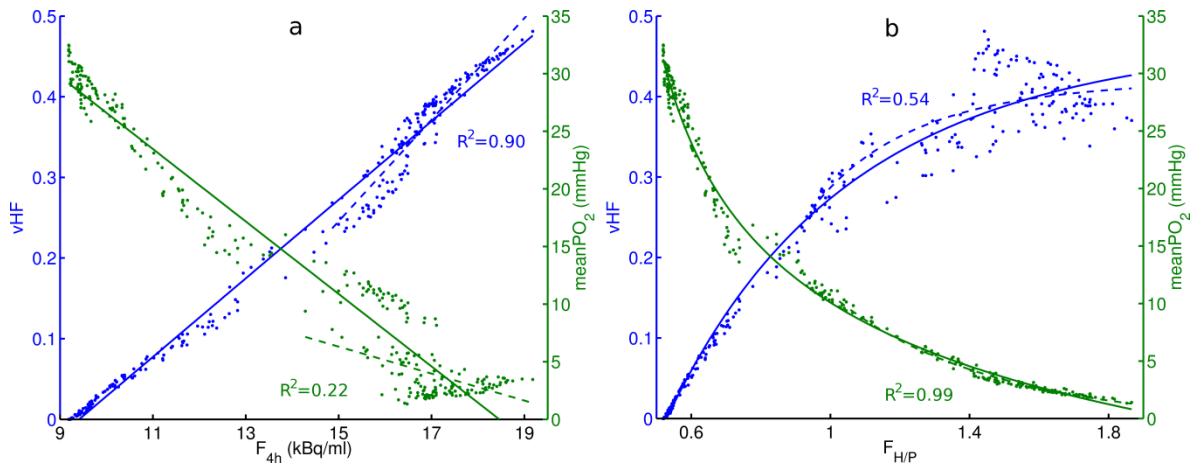


Figure 5: Scatter plots of vHF and meanPO₂ against (a) F_{4h} and (b) the two-scan parameter F_{H/P}. Continuous lines are fits to the overall data, while dashed lines are fits restricted to hypoxic regions. Coefficients of determination R² for the restricted fits show that F_{4h} is correlated to vHF. In contrast, meanPO₂ is well correlated to F_{H/P} only.

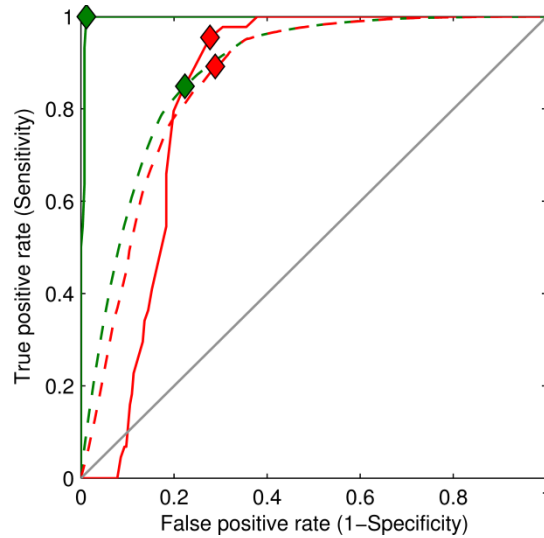


Figure 6: Receiver operating characteristic of F_{H/P} (green curves) and F_{4h} (red curves) for the identification of hypoxia (PO₂<2.5 mmHg). Solid and dashed lines refer to the identification of meanPO₂ and microPO₂, respectively. Cut off values applied to the FMISO parameters decrease along the curves from left to right. Optimum points, in terms of maximum Youden indices, are marked. Identification of critical meanPO₂ is very sensitive and specific using F_{H/P} (YI=0.94). Using F_{4h} is less effective (YI=0.68). Both parameters are moderately accurate in identifying critical microPO₂ values (YI=0.63 and 0.60).

D. Combined PET/CT for IMRT treatment planning of NSCLC: Contrast-enhanced CT images for Monte Carlo dose calculation

published in

Physica Medica: European Journal of Medical Physics 2012, article in press.

Available online at www.sciencedirect.com

SciVerse ScienceDirect

journal homepage: <http://intl.elsevierhealth.com/journals/ejmp>

ORIGINAL PAPER

Combined PET/CT for IMRT treatment planning of NSCLC: Contrast-enhanced CT images for Monte Carlo dose calculation

David Mönnich^{a,*}, Stephan Lächelt^b, Thomas Beyer^{c,d},
Matthias K. Werner^e, Daniela Thorwarth^a

^a Section for Biomedical Physics, University Hospital for Radiation Oncology, Eberhard-Karls-University Tübingen, Hoppe-Seyler-Str. 3, 72076 Tübingen, Germany

^b University Hospital for Radiation Oncology, Eberhard-Karls-University Tübingen, Germany

^c Imaging Science Institute, Tübingen, Germany

^d cmi-experts GmbH, Zurich, Switzerland

^e Department of Diagnostic and Interventional Radiology, Eberhard-Karls-University Tübingen, Germany

Received 24 May 2012; received in revised form 24 July 2012; accepted 8 August 2012

KEYWORDS

Intravenous contrast;
IMRT;
Lung cancer;
Monte Carlo dose
calculation

Abstract *Purpose:* Combined PET/CT imaging has been proposed as an integral part of radiotherapy treatment planning (TP). Contrast-enhanced CT (ceCT) images are frequently acquired as part of the PET/CT examination to support target delineation. The aim of this dosimetric planning study was to investigate the error introduced by using a ceCT for intensity modulated radiotherapy (IMRT) TP with Monte Carlo dose calculation for non-small cell lung cancer (NSCLC).

Material and methods: Nine patients with NSCLC prior to chemo-RT were included in this retrospective study. For each patient non-enhanced, low-dose CT (neCT), ceCT and [¹⁸F]-FDG-PET emission data were acquired within a single examination. Manual contouring and TP were performed on the ceCT. An additional set of independent target volumes was auto-segmented in PET images. Dose distributions were recalculated on the neCT. Differences in dosimetric parameters were evaluated.

Results: Dose differences in PTV and lungs were small for all patients. The maximum difference in all PTVs when using ceCT images for dose calculation was –2.1%, whereas the mean difference was less than –1.7%. Maximum differences in the lungs ranged from –1.8% to 2.1% (mean: –0.1%). In four patients an underestimation of the maximum spinal cord dose between 2% and 3.2% was observed, but treatment plans remained clinically acceptable.

* Corresponding author.

E-mail address: david.moennich@med.uni-tuebingen.de (D. Mönnich).

Conclusions: Monte Carlo based IMRT planning for NSCLC patients using ceCT allows for correct dose calculation. A direct comparison to neCT-based treatment plans revealed only small dose differences. Therefore, ceCT-based TP is clinically safe as long as the maximum acceptable dose to organs at risk is not approached.

© 2012 Associazione Italiana di Fisica Medica. Published by Elsevier Ltd. All rights reserved.

Introduction

Combined PET/CT imaging enables the quasi-simultaneous acquisition of PET and CT data within a single examination without moving the patient off the bed in between scans [1]. Over the past decade, whole-body PET/CT has become a diagnostic modality-of-choice for the work-up of cancer patients [2]. PET/CT is increasingly employed in radio-chemotherapy treatment planning (TP) [3,4]. The use of PET/CT in radiotherapy (RT) treatment planning is further supported by adaptations to the hardware, the possible use of a radiotherapy pallet for patient positioning and DICOM connectivity to RT planning systems [5]. PET/CT examinations performed in treatment position, including positioning devices, can be directly used for tumor delineation based on the available anatomical and metabolic information [3,6,7]. Frequently, the separate acquisition of a planning CT can be waived in favor of a single PET/CT acquisition [8].

Modern radiation dose calculation algorithms rely on CT-derived tissue density information. It is generally accepted that dose calculation for radiotherapy should be performed on non-enhanced CT (neCT) images acquired without intravenous (IV) contrast administration. However, combined PET/CT imaging including contrast-enhanced CT (ceCT) protocols has been shown to yield more accurate information in several tumor entities than non-enhanced PET/CT alone [9,10]. Further, contrast-enhanced PET/CT facilitates clinical whole-body staging, therapy response assessment as well as delineation of target volumes and organs at risk (OARs) [11,12].

Modern CT contrast agents consist of iodine in a non-ionic, complexed form, for instance iopromide in different concentrations equivalent to 150–370 mg/mL ionic iodine for IV application. Ramm et al. investigated the influence of comparatively high atomic number contrast agents, such as barium-sulfate [13]. Using phantom studies, the authors found that accumulations of high-density CT contrast agents with attenuation values of 500 HU, or less in volumes of 5 cm diameter, or less lead to errors in the dose calculations of 1%–3%. Clinical patient studies reported a similarly low bias in dose calculations from the presence of IV CT contrast (300–370 mg/mL iodine) for NSCLC [14–16]. Also, some head-and-neck planning studies concluded that there is no clinically relevant influence on calculated dose [16–20]. Some of these studies relied on a single CT volume only and densities within blood-vessels were virtually altered to simulate the effect of IV contrast. Even in TP of radiosurgery of cerebral arteriovenous malformations, where CT attenuation differences within the target volume were large, a significant effect was observed in selected cases only [21].

The purpose of this study was to evaluate the effect of IV CT contrast enhancement on TP with Monte Carlo (MC) dose calculation in intensity modulated radiotherapy (IMRT) of patients with non-small cell lung cancer (NSCLC). In contrast to earlier studies where artificial CT densities were assigned to single volumes, this investigation includes original neCT and ceCT images with proven co-registration, as they were acquired as part of the same PET/CT examination. In addition, the effect of IV contrast agents on dose calculation was evaluated using state-of-the art MC dose calculation, which was shown to yield accurate results for TP of NSCLC [22].

Material and methods

Patient data

Nine patients diagnosed with NSCLC prior to combined radio-chemotherapy (RCT) were included in this retrospective planning study. Additional patient characteristics are summarized in Table 1. All patients were examined between 2003 and 2009 in the context of the randomized multicenter ESPATUE (Essen-Paris-Tübingen) study. Each patient recruited at the University Hospital Tübingen received a pre-treatment [¹⁸F]-FDG-PET/CT examination for staging purposes followed by a second PET/CT exam between day 16 and day 21 of RCT. From the originally available data ($n = 34$), a subgroup of nine patients meeting the following criteria was selected:

- Location of the main tumor mass confirmed in the upper lobe of the lung, in order to reduce respiratory motion artifacts.
- Availability of complete image volumes for neCT, ceCT and PET emission acquisition.
- Visually verified spatial alignment of neCT and ceCT image volumes using retrospective image co-

Table 1 Characteristics of patients selected for this study ($n = 9$).

| Pat | Age (y) | Gender | TNM stage | PTV _{CT} (mL) | PTV _{PET} (mL) |
|-----|---------|--------|-----------|------------------------|-------------------------|
| 1 | 54 | M | T4N0M0 | 357 | 250 |
| 2 | 65 | M | T4N0M0 | 881 | 213 |
| 3 | 53 | M | T4N3M0 | 967 | – |
| 4 | 66 | M | T1bN0M0 | 268 | 130 |
| 5 | 56 | M | T2bN0M0 | 1002 | 267 |
| 6 | 63 | M | T4N2M0 | 978 | 329 |
| 7 | 52 | M | T4N0M0 | 994 | 581 |
| 8 | 57 | M | T3N0M0 | 584 | 173 |
| 9 | 54 | F | T2aN2M0 | 480 | 92 |

registration. Here, neCT and ceCT image volumes were aligned using automated linear and non-linear co-registration based on mutual information algorithms (Mirada XD3, Mirada Medical Ltd., UK). Following the spatial co-registration, the image registration quality was visually assessed and then the image volume alignment of neCT and ceCT data was confirmed. If the residual maximum average misregistration vector provided by the software was less than the PET voxel size (600 mm, 128 matrix size: 4.7 mm) then the CT image volumes were considered accurately aligned for the purpose of CT-based attenuation correction and dose planning. Note, the spatial resolution of the CT and PET emission data must be the same.

Patient protocol

Patients fasted for 6 h prior to the injection of [^{18}F]-FDG. Patients were then injected with a median [^{18}F]-FDG dose of 441 MBq. During the median uptake phase of 62 min patients rested in a reclined position in a dimly lit room. A negative oral CT contrast was administered during the uptake phase [23]. Patients were positioned head first supine on a vacuum cushion and an RT table top with their arms raised and supported above the head. PET/CT imaging was performed on a Biograph HiRez 16 PET/CT (Siemens Healthcare, Germany).

The imaging sequence was as follows: topogram scan, low-dose non-enhanced CT (neCT), arterial-phase contrast-enhanced CT (ceCT) following 100 mL of 370 mg/mL iodine-equivalent non-ionic intravenous iodinated contrast agent (Ultravist 370, Bayer-Schering, Germany) and a multi-bed emission scan of 3 min/bed. More details are given in [24]. Emission and CT imaging with and without IV contrast was performed during tidal breathing and in mid-expiration, respectively [25]. PET image reconstruction was performed using a 2D OSEM algorithm with 2 iterations, 8 subsets and a matrix size of 128×128 . PET attenuation correction was performed based on the neCT images with a well-established algorithm described elsewhere [26].

Treatment planning and target volumes

For this retrospective study PET/CT image data from the pre-treatment examination were used. Target volumes (TV) and OARs were delineated manually on the ceCT using the treatment planning system Oncentra MasterPlan (Nucletron, The Netherlands). A clinical target volume (CTV_{CT}) including the primary tumor and involved lymph nodes was created by an experienced RT specialist in accordance with

the guidelines of the International Commission on Radiation Units & Measurements (ICRU) Report 62 [27]. A second clinical target volume (CTV_{PET}) was automatically segmented in the PET images using a fixed threshold at 42% of the maximum standardized uptake value [28] (Siemens TrueD, Siemens Healthcare). Both volumes were uniformly expanded by a 1.5 cm safety margin to obtain planning target volumes (PTV_{CT} and PTV_{PET} , Fig. 1) that were subject to a dose prescription of 60 Gy in 30 fractions. OARs considered for NSCLC IMRT planning were heart, total lung, and spinal cord.

IMRT TP was performed on the ceCT with the Hyperion planning system using a dedicated MC dose engine [22,29]. The voxel size for the dose calculation and estimated MC accuracy was set to 3 mm and 2%, respectively. Six to ten coplanar 6 MV beams were applied. The primary objective was to enclose the PTV within the 95% isodose line as long as normal tissue constraints were met and to achieve high target dose uniformity. Doses higher than 105% of the prescribed dose were not allowed.

In a second step, the created treatment plans were recalculated based on tissue densities in the neCT (Fig. 1). Here, accurate alignment of neCT and ceCT image volumes was assumed, since the patients eligible for this study were shown not to have moved in between the CT examinations. Previously, it was reported that dose errors induced by differences in attenuation values between low- and full-dose CTs are below 2% [30]. Thus, it is legitimate to use doses calculated on non-enhanced low-dose CTs as references.

Data analysis

Relative dose differences in the PTV, the spinal cord and healthy lung tissue (total lung – PTV) were calculated as

$$\Delta D = (D_{\text{ceCT}} - D_{\text{neCT}}) / D_{\text{ceCT}} \times 100 \quad (1)$$

where ΔD is the relative dose difference in % and D is the respective dosimetric parameter. This definition differs in sign compared to results in [15]. Relative differences were calculated for mean and maximum dose. Maximum dose differences of more than 3% were considered to be clinically relevant. Additionally, differences in the fractional volume of healthy lung tissue receiving more than 20 Gy (V_{20}) and the minimum dose within 95% of the PTV (D_{95}) were evaluated. PTV_{PET} plans were assessed independently using the same method.

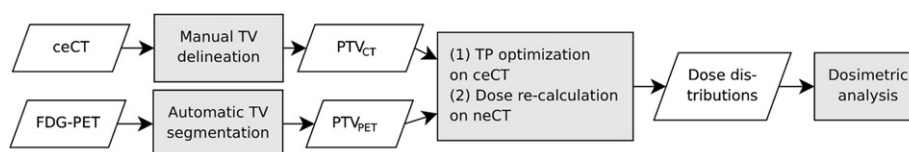


Figure 1 Flow chart for the presented study. First, two target volumes were segmented independently on the contrast-enhanced CT (ceCT) and [^{18}F]-FDG-PET. Then, two independent planning target volumes were generated based on these volumes: PTV_{CT} and PTV_{PET} , respectively. This was followed by ceCT-based treatment plan (TP) optimization and dose recalculation on the corresponding non-enhanced low-dose CT (neCT). Finally, the resulting differences in dosimetric parameters were evaluated.

Results

A direct comparison of the CT attenuation values in ne- and ceCT images demonstrated that IV contrast leads to an increased fraction of higher attenuating tissue voxels in relevant sub-volumes (Fig. 2). Contrast administration leads to an increased number of voxel values between 150 HU and 300 HU in the ceCT.

Manually delineated PTVs had a mean size of 723 mL (range: 268 mL–1002 mL), and were generally larger than those segmented from PET images with a mean volume of 254 mL (range: 92 mL–581 mL) (Table 1).

An acceptable dose coverage complying with normal tissue constraints was achieved in all treatment plans with one exception where the full dose was applicable to the manually delineated CTV only (patient 10). The resulting median mean dose was 59.3 Gy (range: 55.2 Gy–60.9 Gy) for PTV_{CT} plans and 59.8 Gy (59.2 Gy–60.7 Gy) for PTV_{PET} plans. Dose parameters for all plans created on the neCT images are shown in Table 2.

Table 3 shows the relative dose differences ΔD between neCT and ceCT for PTVs as well as OARs. Relative dose differences in the target volumes were below 2% in almost all cases. For patient 9, differences in the maximum dose and D_{95} for the PTV were -2.1% and -2.2% , respectively, which reflects a noncritical overdosage in the original plan. In contrast, a positive difference of 2.6% in D_{95} in the PET-PTV plan for the same patient reveals a moderate underdosage.

For the mean PTV dose mainly negative differences were found with a median value for PTV_{CT} and PTV_{PET} of -0.9% , and -0.3% , respectively. This indicates a small systematic underestimation of the applied dose caused by the usage of the ceCT as a basis for dose calculation. Dose differences in the lung were below 2% with the exception in patient 9, where V_{20} and mean dose were underestimated by -3.6%

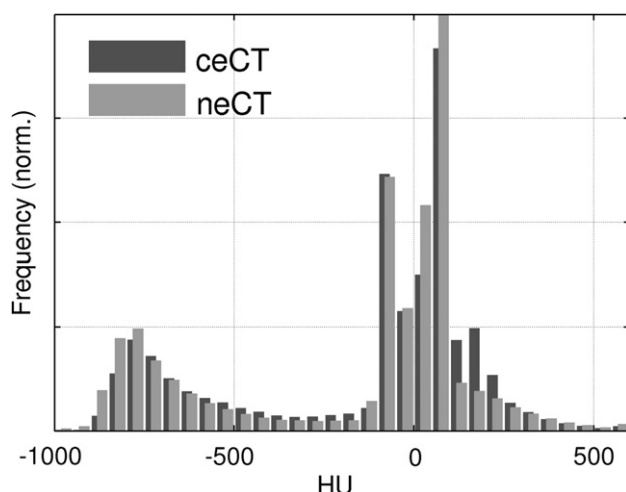


Figure 2 Histogram of Hounsfield units in the non-enhanced (neCT) and contrast-enhanced (ceCT) CT volume covering the co-axial range of the target volume (patient 5). Note the increased number of voxels with higher attenuation values in the range of 150–300 HU after intravenous contrast administration (ceCT).

Table 2 Characteristics of treatment plans created on non-enhanced CT volumes for the patient group of this study.

| | Dosimetric parameter median (range) | |
|----------------------------|-------------------------------------|--------------------|
| | PTV _{CT} | PTV _{PET} |
| Mean dose PTV (Gy) | 59.3 (55.2–60.9) | 59.8 (59.2–60.7) |
| Max dose PTV (Gy) | 65.4 (64.3–67.0) | 64.7 (62.7–65.9) |
| D_{95} (Gy) | 56.3 (47.5–58.2) | 56.6 (55.9–57.8) |
| Mean dose lungs (Gy) | 19.8 (9.5–23.7) | 10.8 (7.1–16.9) |
| Max dose lungs (Gy) | 64.2 (63.3–66.8) | 63.7 (62.7–65.9) |
| V_{20} (%) | 25.9 (13.7–34.3) | 16.3 (6.3–25.4) |
| Mean dose spinal cord (Gy) | 12.3 (7.3–18.2) | 6.9 (5.5–11.9) |
| Max dose spinal cord (Gy) | 36.2 (21.7–40.6) | 25.6 (17.1–46.5) |

and -2.4% , respectively. Differences in mean spinal cord doses were below 2% for all plans with median values of -1.2% (PTV_{CT}) and -1.5% (PTV_{PET}). Maximum spinal cord doses were underestimated in all but one case. In some plans the underestimation was larger than 2% with a maximum of -3.2% in the PTV_{PET} plan of patient 5. Nevertheless, no critical overdosages were observed in this particular case, considering that absolute maximum doses remained below 45 Gy.

Figure 3 shows IMRT treatment plans on neCT and ceCT images for patients 9 and 5. Examples of the resulting dose distributions are depicted for selected axial image planes. In patient 9, differences between the original and the recalculated dose distribution (Fig. 3a, b) can be identified in a region where the PTV_{CT} overlaps with large arteries containing contrast agent. The shape of the 95% isodose line is different and a small overdosed region (>63 Gy) appears in the recalculated plan. In another patient (patient 5, Fig. 3d, e) the isodose lines of both dose distributions are virtually identical. Voxel-based relative dose differences reveal some mismatch artifacts close to the body surface and also local differences smaller than -6% and larger than 6% in low-dose regions (Fig. 3c, f). Figure 4 shows the corresponding dose volume histograms (DVH) for patients 9 and 5. Here, the effect of ceCT-based TP, which is a slight underestimation in terms of dose in the contrast-enhanced target regions, is clearly visible.

Discussion

The uniqueness of the presented study is given by (a) the availability of pairs of original NSCLC CT image data acquired with and without IV contrast in one single examination and (b) by the use of an MC dose calculation to investigate the effect of ceCT on RT TP. As neCT and ceCT were acquired during the same examination and in the same breathing phase, accurate co-registration of the corresponding image data sets could be validated retrospectively. As a result, identical regions of interest could be used for ne- and ceCT-based TP. Furthermore, the type of dose calculation used to study this effect is of major

Table 3 Relative differences for various dosimetric parameters (Equation (1)). Values larger than 2% are marked in gray. PET data were unavailable for patient 3.

| Pat # | PTV _{CT} | | | | | | PTV _{PET} | | | | | |
|--------|-------------------|-------|-----------------|-------------|-------|-----------------|--------------------|-------|-----------------|-------------|-------|-----------------|
| | Total lung | | | Spinal cord | | | Total lung | | | Spinal cord | | |
| | Mean | Max | D ₉₅ | Mean | Max | V ₂₀ | Mean | Max | D ₉₅ | Mean | Max | V ₂₀ |
| 1 | -0.1% | 0.0% | 0.2% | -0.8% | -0.8% | -0.6% | 0.7% | 0.0% | 0.3% | 0.2% | 0.5% | 1.8% |
| 2 | -0.7% | -0.6% | -0.7% | -0.9% | -1.2% | -1.1% | -1.4% | -1.9% | 0.0% | -0.4% | 0.7% | -0.1% |
| 3 | -0.9% | -0.1% | -0.7% | -0.9% | -0.3% | -0.8% | -1.0% | -0.2% | 0.0% | 0.0% | 0.0% | -0.6% |
| 4 | -1.4% | -0.9% | -0.4% | -1.2% | 2.1% | -1.2% | -1.2% | -1.7% | 1.1% | 0.1% | 0.4% | 0.1% |
| 5 | -1.3% | -1.8% | -1.4% | -1.2% | -0.3% | -1.5% | -1.3% | -0.9% | -0.8% | -1.2% | -1.6% | 0.0% |
| 6 | -1.0% | -0.2% | -1.3% | -1.2% | -0.2% | -1.2% | -1.3% | -2.2% | -1.2% | -0.8% | -1.0% | -1.3% |
| 7 | -0.4% | -0.2% | -0.2% | -1.3% | 1.0% | -1.4% | -1.3% | -2.1% | -0.6% | -0.6% | -0.1% | -1.8% |
| 8 | -0.6% | 0.2% | -0.5% | -1.1% | -0.1% | -1.6% | -1.0% | 0.4% | 0.2% | -0.3% | -1.4% | 0.9% |
| 9 | -1.7% | 2.1% | 2.2% | 2.4% | 0.7% | 3.6% | -0.6% | -1.5% | 2.6% | 0.0% | 0.7% | -2.6% |
| Median | -0.9% | -0.2% | -0.7% | -1.2% | -0.2% | -1.2% | -1.2% | -1.5% | 0.1% | -0.3% | 0.1% | 0.0% |

importance. It is known, that current analytical dose calculation algorithms introduce errors of up to 5%, especially in the case of high density materials and high density gradients, i.e. tissue-bone and tissue-air interfaces [31,32]. It is not safe to assume that results obtained with such algorithms are as well applicable to more accurate MC dose calculation.

We were able to demonstrate that dose calculation based on ceCT images is possible and results in acceptable treatment plans. Errors introduced by using CT images following IV contrast enhancement were clinically negligible in all patients. In most cases the applied dose in targets as well as OARs was underestimated. Underdosage effects were regional and resulted either from the attenuation of beams by enhanced structures shadowing a volume-of-interest, or from the direct effect of less dose being deposited in enhanced structures compared to non-enhanced CT TP.

The magnitude of dose differences in PTVs and healthy lung tissue were much smaller than errors anticipated from tumor motion during irradiation (Table 3). Specifically, the dose simulation underestimates target doses, which may translate into excess radiation doses. This increase may, however, be acceptable in NSCLC if it is below 110%. This result agrees with other studies investigating the influence of intravenous contrast on IMRT planning of NSCLC [14,15].

Dose differences in the lung, though much larger than reported by Xiao et al. [15], were clinically irrelevant (Table 3). Deviations from the results reported by Xiao et al. [15] may be due to the fact that in their study a convolution/superposition algorithm was used for dose calculation. Good agreement with the results of Shi et al. [14] was found in the patient group averages of differences in V₂₀ and mean lung dose. Generally, it is difficult to compare the presented patient specific values with other studies, because most of them reported group averages only, thus obliterating extreme differences from the results.

Relevant differences were found in the maximum spinal cord dose, which varied by up to 3.2% on a single patient basis. These patient based differences are considerably larger than the cohort averages of 0.4% as reported by Shi et al. using single CTs and density override [14]. In the spinal cord, errors of the observed magnitude might be relevant in cases with high local dose burdens approaching 45 Gy. In these cases it may be feasible to adjust tissue densities following the delineation of contrast-enhanced regions.

A careful clinical interpretation of the dosimetric differences in patients of this pilot study is required. First, the minor differences can be explained by the use of an MC dose engine and two independent CT image volumes (neCT and ceCT). The observed dose differences may be caused also by effects of respiratory motion, which may lead to sub-cm, or even sub-mm alignment accuracies of the lesions on neCT and ceCT. Here, the neCT and ceCT image volumes were acquired sequentially in mid-expiration breath-hold [24,25], which improves spatial co-registration of complementary image volumes [33].

In addition to the small group size of this study, it should be mentioned that a potential influence of dose calculation errors on the convergence of the TP software to the optimum treatment plan was not investigated in this study.

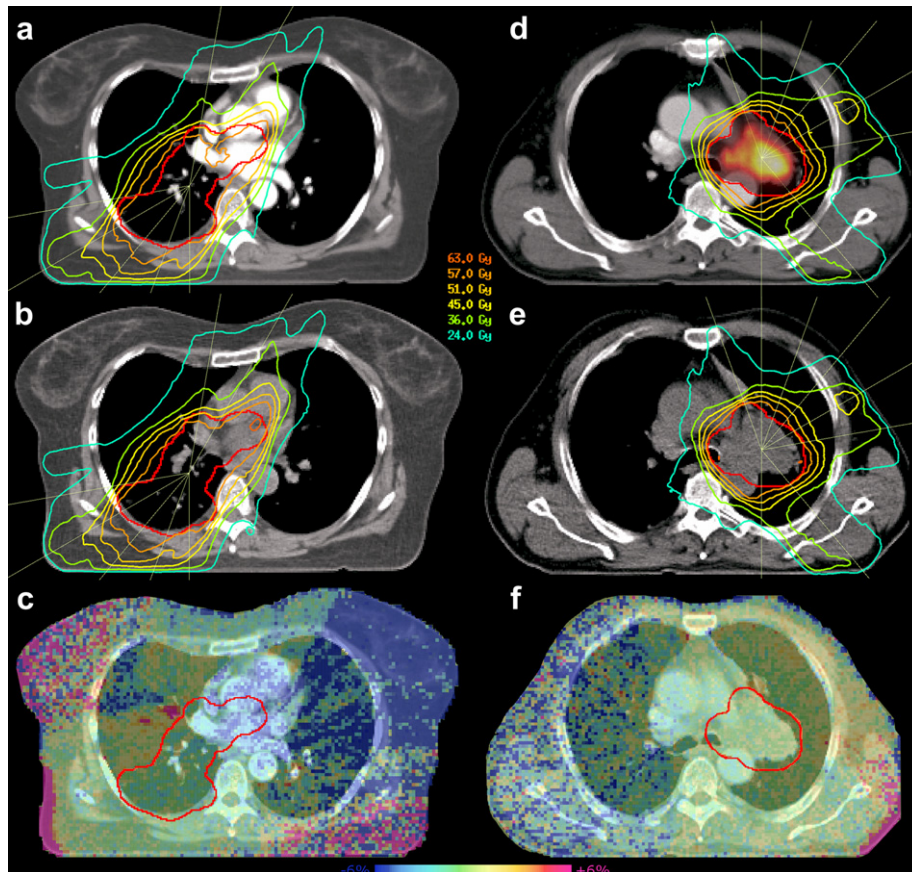


Figure 3 Selected axial image planes from the PTV_{CT} plan of patient 9 (a–c) and the PTV_{PET} plan of patient 5 (d–f). Isolines of the dose distributions as planned on ceCT are depicted in a and d, respectively. Isolines of dose distributions recalculated using the neCT are illustrated in b and e. Corresponding voxel-based relative dose differences are shown in c and f.

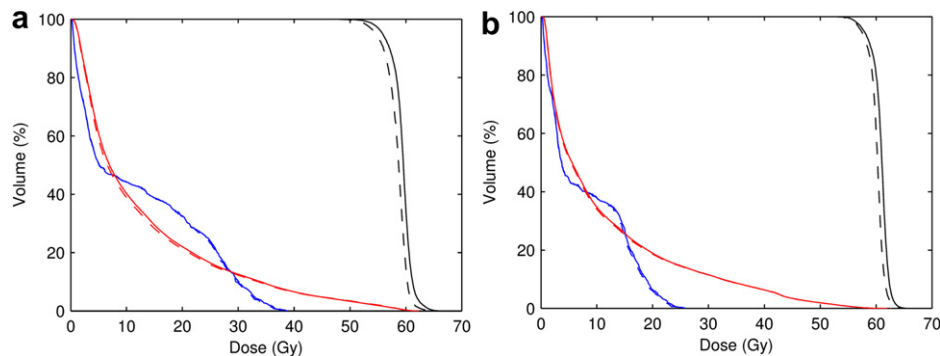


Figure 4 Dose volume histograms of patient 9 (a) and 5 (b) in the PTV (black), the lungs (red) and the spinal cord (blue). Continuous lines represent treatment plans created on the ceCT and dashed lines those recalculated on the neCT. Dose differences are most obvious within the PTV_{CT} of patient 9. (For interpretation of the references to color in this figure legend, the reader is referred to the web version of this article.)

Conclusions

Our data support the notion of using contrast-enhanced CT as part of combined PET/CT imaging for radiotherapy treatment planning in NSCLC without the need to acquire a separate, low-dose CT. MC dose calculation based on ceCT images was shown to yield correct treatment plans in terms of relative errors in dose compared to neCT-based

planning. Care must be taken in cases with perceived high doses to OARs, where critical overdoses might result when TP is performed on a contrast-enhanced CT.

Conflict of interest

Thomas Beyer is founder and president of cmi-experts GmbH, Zurich and reports no conflict of interest.

Acknowledgments

DT is supported by the European Social Fund and the Ministry of Science, Research and the Arts Baden-Württemberg. We thank Markus Alber (University Hospital for Radiation Oncology, Tübingen) for providing us with a research version of the TPS Hyperion and Mirada Medical, UK for XD3 image fusion software.

List of abbreviations

| | |
|--------|--|
| ceCT | contrast-enhanced computed tomography |
| CTV | clinical target volume |
| DVH | dose volume histogram |
| FDG | fluorodesoxyglucose |
| HU | Hounsfield Unit |
| ICRU | International Commission for Radiation Units & Measurement |
| IMRT | intensity modulated radiation therapy |
| IV | intravenous |
| MC | Monte Carlo |
| neCT | non-enhanced computed tomography |
| NSCLC | non-small cell lung cancer |
| OAR | organ at risk |
| OSEM | ordered subsets expectation maximization |
| PET/CT | positron emission tomography/computed tomography |
| PTV | planning target volume |
| RCT | radio-chemotherapy |
| RT | radiation therapy |
| TP | treatment planning |
| TV | target volume |

References

- [1] Beyer T, Townsend DW, Brun T, Kinahan PE, Charron M, Roddy R, et al. A combined PET/CT scanner for clinical oncology. *J Nucl Med* 2000;41:1369–79.
- [2] Czernin J, Allen-Auerbach M, Schelbert HR. Improvements in cancer staging with PET/CT: literature-based evidence as of September 2006. *J Nucl Med* 2007;48(Suppl. 1):785–885.
- [3] Nestle U, Weber W, Hentschel M, Grosu AL. Biological imaging in radiation therapy: role of positron emission tomography. *Phys Med Biol* 2009;54:R1–25.
- [4] Lammering G, De Ruyscher D, van Baardwijk A, Baumert BG, Borger J, Lutgens L, et al. The use of FDG-PET to target tumors by radiotherapy. *Strahlenther Onkol* 2010;186:471–81.
- [5] Sattler B, Lee JA, Lonsdale M, Coche E. PET/CT (and CT) instrumentation, image reconstruction and data transfer for radiotherapy planning. *Radiother Oncol* 2010;96:288–97.
- [6] Evans PM. Anatomical imaging for radiotherapy. *Phys Med Biol* 2008;53:R151–91.
- [7] Thorwarth D, Schaefer A. Functional target volume delineation for radiation therapy on the basis of positron emission tomography and the correlation with histopathology. *Q J Nucl Med Mol Imaging* 2010;54:490–9.
- [8] Thorwarth D, Geets X, Paiusco M. Physical radiotherapy treatment planning based on functional PET/CT data. *Radiother Oncol* 2010;96:317–24.
- [9] Pfannenbergs AC, Aschoff P, Brechtel K, Müller M, Bares R, Paulsen F, et al. Low dose non-enhanced CT versus standard dose contrast-enhanced CT in combined PET/CT protocols for staging and therapy planning in non-small cell lung cancer. *Eur J Nucl Med Mol Imaging* 2007;34:36–44.
- [10] Antoch G, Freudenberg LS, Beyer T, Bockisch A, Debatin JF. To enhance or not to enhance? 18F-FDG and CT contrast agents in dual-modality 18F-FDG PET/CT. *J Nucl Med* 2004;45(Suppl. 1):56S–65S.
- [11] De Ruyscher D, Kirsch C-M. PET scans in radiotherapy planning of lung cancer. *Radiother Oncol* 2010;96:335–8.
- [12] Roy AEF, Wells P. Volume definition in radiotherapy planning for lung cancer: how the radiologist can help. *Cancer Imaging* 2006;6:116–23.
- [13] Ramm U, Damrau M, Mose S, Manegold K-H, Rahl CG, Böttcher H-D. Influence of CT contrast agents on dose calculations in a 3D treatment planning system. *Phys Med Biol* 2001;46:2631–5.
- [14] Shi W, Liu C, Lu B, Yeung A, Newlin HE, Amdur RJ, et al. The effect of intravenous contrast on photon radiation therapy dose calculations for lung cancer. *Am J Clin Oncol* 2010;33:153–6.
- [15] Xiao J, Zhang H, Gong Y, Fu Y, Tang B, Wang S, et al. Feasibility of using intravenous contrast-enhanced computed tomography (CT) scans in lung cancer treatment planning. *Radiother Oncol* 2010;96:73–7.
- [16] Shibamoto Y, Naruse A, Fukuma H, Ayakawa S, Sugie C, Tomita N. Influence of contrast materials on dose calculation in radiotherapy planning using computed tomography for tumours at various anatomical regions: a prospective study. *Radiother Oncol* 2007;84:52–5.
- [17] Liauw SL, Amdur RJ, Mendenhall WM, Palta J, Kim S. The effect of intravenous contrast on intensity-modulated radiation therapy dose calculations for head and neck cancer. *Am J Clin Oncol* 2005;28:456–9.
- [18] Létourneau D, Finlay M, O'Sullivan B, Waldron JN, Cummings BJ, Ringash J, et al. Lack of influence of intravenous contrast on head and neck IMRT dose distributions. *Acta Oncol* 2008;47:90–4.
- [19] Choi Y, Kim J-K, Lee H-S, Hur W-J, Hong Y-S, Park S, et al. Influence of intravenous contrast agent on dose calculations of intensity modulated radiation therapy plans for head and neck cancer. *Radiother Oncol* 2006;81:158–62.
- [20] Lee FK-H, Chan CC-L, Law C-K. Influence of CT contrast agent on dose calculation of intensity modulated radiation therapy plan for nasopharyngeal carcinoma. *J Med Imaging Radiat Oncol*, 53: 114–118.
- [21] Zabel-du Bois A, Ackermann B, Hauswald H, Schramm O, Sroka-Perez G, Huber P, et al. Influence of intravenous contrast agent on dose calculation in 3-D treatment planning for radiosurgery of cerebral arteriovenous malformations. *Strahlenther Onkol* 2009;185:318–24.
- [22] Sikora M, Muzik J, Söhn M, Weinmann M, Alber M. Monte Carlo vs. pencil beam based optimization of stereotactic lung IMRT. *Radiat Oncol* 2009;4:64.
- [23] Antoch G, Kuehl H, Kanja J, Lauenstein TC, Schneemann H, Hauth E, et al. Dual-modality PET/CT scanning with negative oral contrast agent to avoid artifacts: introduction and evaluation. *Radiology* 2004;230:879–85.
- [24] Brechtel K, Klein M, Vogel M, Mueller M, Aschoff P, Beyer T, et al. Optimized contrast-enhanced CT protocols for diagnostic whole-body 18F-FDG PET/CT: technical aspects of single-phase versus multiphase CT imaging. *J Nucl Med* 2006;47:470–6.
- [25] Beyer T, Rosenbaum S, Veit P, Stattaus J, Müller SP, Difilippo FP, et al. Respiration artifacts in whole-body (18)F-FDG PET/CT studies with combined PET/CT tomographs employing spiral CT technology with 1 to 16 detector rows. *Eur J Nucl Med Mol Imaging* 2005;32:1429–39.

- [26] Kinahan PE, Hasegawa BH, Beyer T. X-ray-based attenuation correction for positron emission tomography/computed tomography scanners. *Semin Nucl Med* 2003;33:166–79.
- [27] International Commission on Radiation Units and Measurements. ICRU report 62. Prescribing, recording, and reporting photon beam therapy (supplement to ICRU report 50). Bethesda, MD: ICRU; 1999.
- [28] Erdi YE, Mawlawi O, Larson SM, Imbriaco M, Yeung H, Finn R, et al. Segmentation of lung lesion volume by adaptive positron emission tomography image thresholding. *Cancer* 1997; 80(Suppl.):2505–9.
- [29] Alber M, Birkner M, Laub M, Nüsslin F. Hyperion: an integrated IMRT planning tool. In: Schlegel W, Bortfeld T, editors. Proceedings of the XIII conference on the use of computers in radiation therapy. , Heidelberg: Springer; 2000. p. 46–8.
- [30] Kurth J, Vogel H, Dunkelmann S, Hildebrandt G, Schümichen C. Nutzung des low-dose-CT der PET/CT für die Strahlentherapieplanung – Einfluss des CT-Protokolls auf die CT-Elektronendichte-Konvertierung. *Nuklearmedizin* 2011;50:A51.
- [31] Vanderstraeten B, Reynaert N, Paelinck L, Madani I, De Wagter C, De Gersem W, et al. Accuracy of patient dose calculation for lung IMRT: a comparison of Monte Carlo, convolution/superposition, and pencil beam. *Med Phys* 2006;33: 3149–58.
- [32] Hasenbalg F, Neuenschwander H, Mini R, Born EJ. Collapsed cone convolution and analytic anisotropic algorithm dose calculation compared to VMC++ Monte Carlo simulations in clinical cases. *Phys Med Biol* 2007;52:3679–91.
- [33] Beyer T, Antoch G, Müller S, Egelhof T, Freudenberg LS, Debatin J, et al. Acquisition protocol considerations for combined PET/CT imaging. *J Nucl Med* 2004;45(Suppl. 1):255–355.